AN EVALUATION OF IMAGE BASED TECHNIQUES FOR WILDFIRE DETECTION AND FUEL MAPPING

By

DUSTIN W. GABBERT

Bachelor of Science in Mechanical Engineering

Bachelor of Science in Aerospace Engineering

Oklahoma State University

Stillwater, OK

2011

Submitted to the Faculty of the
Graduate College of the
Oklahoma State University
in partial fulfillment of
the requirements for
the Degree of
MASTER OF SCIENCE
May, 2015

AN EVALUATION OF IMAGE BASED

TECHNIQUES FOR WILDFIRE DETECTION AND

FUEL MAPPING

Thesis Approved:

Dr. Jamey Jacob

Thesis Adviser

Dr. James Kidd

Dr. Adam Mathews

ACKNOWLEDGEMENTS

I would like to thank Dr. Jamey Jacob and the other members of my thesis committee for sharing their guidance and experience. I would also like to thank Dr. Mehran Andalibi for sharing his helpful insights in computer vision techniques, Dr. JD Carlson for sharing his experience from implementing the fire risk model OKFIRE, Chris Banfield for designing and 3D printing most of the custom parts used in this project, and John Weir for allowing me to film at his controlled burns. Finally, I want to thank my wife, Mary, for her help with proofreading and editing this paper. This research was funded in part by Sandia National Laboratories' Critical Skills Masters Program.

Acknowledgements reflect the views of the author and are not endorsed by committee members or Oklahoma State University

Name: DUSTIN W. GABBERT

Date of Degree: MAY, 2015

Title of Study: AN EVALUATION OF IMAGE BASED TECHNIQUES FOR WILDFIRE DETECTION AND FUEL MAPPING

Major Field: MECHANICAL AND AEROSPACE ENGINEERING

ABSTRACT:

Few events can cause the catastrophic impact to ecology, infrastructure, and human safety of a wildland fire along the wildland urban interface. The suppression of natural wildland fires over the past decade has caused a buildup of dry, dead surface fuels: a condition that, coupled with the right weather conditions, can cause large destructive wildfires that are capable of threatening both ancient tree stands and manmade infrastructure. Firefighters use fire danger models to determine staffing needs on high fire risk days; however models are only as effective as the spatial and temporal density of their observations. OKFIRE, an Oklahoma initiative created by a partnership between Oklahoma State University and the University of Oklahoma, has proven that fire danger assessments close to the fire – both geographically and temporally – can give firefighters a significant increase in their situational awareness while fighting a wildland fire.

This paper investigates several possible solutions for a small Unmanned Aerial System (UAS) which could gather information useful for detecting ground fires and constructing fire danger maps. Multiple fire detection and fuel mapping programs utilize satellites, manned aircraft, and large UAS equipped with hyperspectral sensors to gather useful information. Their success provides convincing proof of the utility that could be gained from low-altitude UAS gathering information at the exact time and place firefighters and land managers are interested in. Close proximity, both geographically and operationally, to the end can reduce latency times below what could ever be possible with satellite observation.

This paper expands on recent advances in computer vision, photogrammetry, and infrared and color imagery to develop a framework for a next-generation UAS which can assess fire danger and aid firefighters in real time as they observe, contain, or extinguish wildland fires. It also investigates the impact information gained by this system could have on pre-fire risk assessments through the development of very high resolution fuel maps.

TABLE OF CONTENTS

Chapter Page

LIST OF TABLES

Table Page

LIST OF FIGURES

Figure Page

Figure Page

CHAPTER I

INTRODUCTION

1. MOTIVATION

On June 30, 2013, 19 firefighters lost their lives fighting a wildfire near Yarnell, AZ. The elite team of firefighters, called the "Hot Shots," was protecting the evacuated town from a 2,000-acre wildfire when the fire encircled them. They were in the wrong location, and they were unaware of an unforecasted wind shift. Because of a lack of situational awareness, these veteran firefighters died trying to simply limit property damage.

Large wildfires can cause massive ecological damage and threaten structures and human lives, and wildfire suppression has increased these risks. Over 9,000,000 acres were burned from wildfires in 2012, and that number has been increasing since 1986. In 2012, the federal government and some states exhausted their wildfire suppression funds trying to contain these fires. [Gabbert, 2012]

Current technology has limited the effectiveness of small UAS for tactical firefighting. Some of the problems identified are the limitations of autonomous capabilities, ease of control, effectiveness of the user interface, and communication of useful information in a timely manner. [Murphy] This paper will address a part of the last problem: efficiently processing raw data into

useful products that firefighters can use while keeping size, weight, and cost low enough to be an effective tool for rural, volunteer fire departments fighting remote wildland fires.

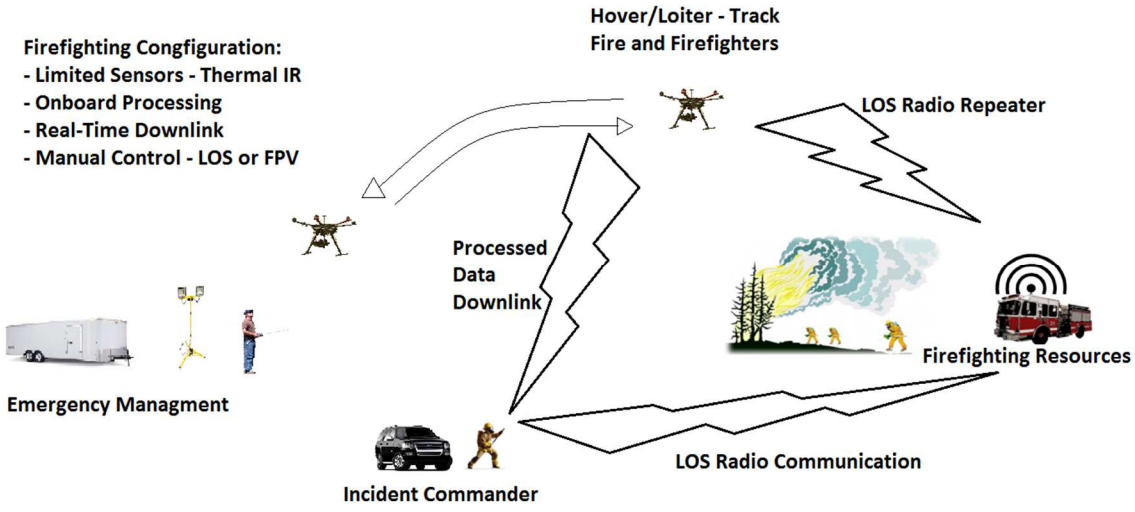

Figure 1 - Concept of operations for a firefighting UAS

Land managers use natural and prescribed burning to eliminate excessive fuel buildups in areas where fire suppression has allowed dead fuel to accumulate on the forest floor. For instance, when draught and high winds created multiple catastrophic fires across Yellowstone National Park in the summer of 1988, 16 years of natural fire management (i.e. allowing fires ignited naturally to burn up to a certain size without suppression) had reduced the available fuels that had accumulated over the previous century of a total fire suppression policy. [Christensen, et al., 1989] Today, prescribed burning is a cornerstone of natural fire management across the US, replacing the regular natural fires of previous centuries with regular manmade fires, which can be analyzed for risk and monitored for safety. Additionally, national policy makers have recognized the need for community preparedness and efficient fire response, specifically a "more realistic and accurate depiction of where wildland fire hazard or risk actually occurs," and to "assist communities with evaluating their risk from wildfire." [National Cohesive Wildland Fire Management Strategy, 2014] Achieving these goals would require an accurate, efficient, and

persuasive means of gathering wildfire risk information and communicating it to the people who need it.

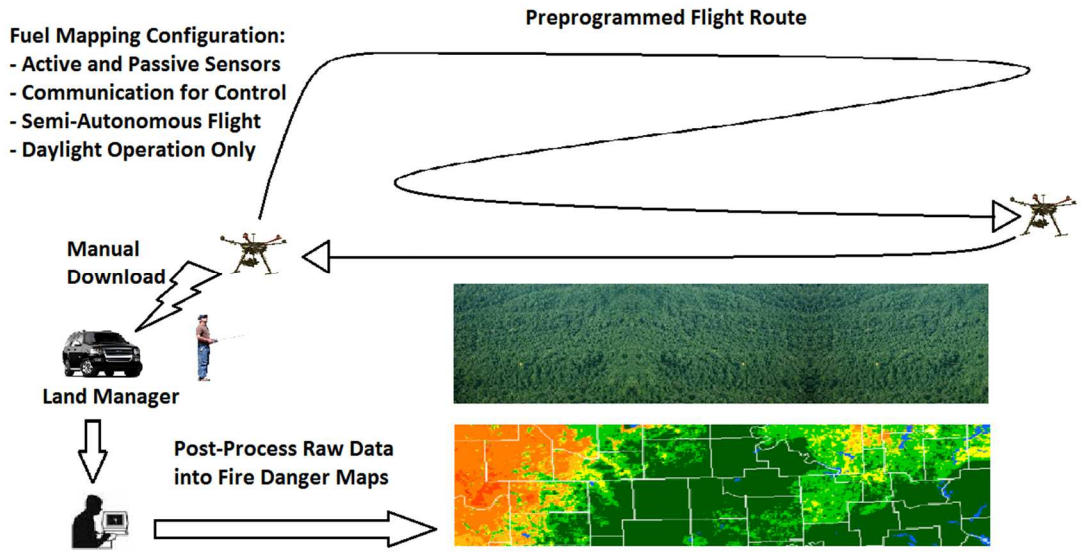

Figure 2 - Concept of Operations for a fuel mapping UAS

Fire spread models are required for safe, large scale prescribed burning. Current wildfire spread models are empirical in nature, and do not integrate the effects of fuels, topography, and weather into the fundamental physical processes that produce fire (heat transfer, combustion, ignition, entrainment, etc.). A robust physics-based fire model requires further experimentation on the impact of atmospheric effects on fire behavior and of fire behavior on the local atmosphere. No one has developed a common experimental basis for determining the organization, order, and required amounts fire spread phenomena. [Carlson, et al. 2003, Wildland Fire Management RD&A, 2013]

2. GOALS AND OBJECTIVES

The goal of this paper is to develop and evaluate imaging sensors and algorithms for wildland fire surveillance and fuel mapping with small UAS. The specific objectives of this paper are:

1. Determine the specific situational awareness needs of an incident commander responding to a wildfire that can be solved using image processing techniques.
2. Evaluate the capabilities of image processing to increase an incident commander's situational awareness
    a. Autonomous flame detection using video captured by a UAS
    b. Autonomous smoke detection using video captured by a UAS.
    c. Fuel load mapping using Color Near Infrared (NIR) imagery captured by a UAS and Structure from Motion (SfM) techniques.
    d. Identification of vegetation type and fuel state using low-cost multispectral sensors from a UAS.
3. Evaluate multiple UAS platforms for application to specific firefighting tasks.
4. Evaluate multiple sensor packages, both passive and active, for application to specific firefighting tasks.
5. Analyze the abilities and costs of commercial-off-the-shelf platforms and sensors to recommend a UAS that would benefit a small, volunteer fire department.
6. Evaluate the minimum crew requirements of a useful wildfire UAS by developing an effective single-operator system.

CHAPTER II

REVIEW OF LITERATURE

1. SURVEY OF WILDLAND TACTICAL FIREFIGHTING

Municipal fire departments, often volunteer fire departments, are usually the first to respond to a wildland fire report. The Incident Commander has the responsibility to contain the fire with the resources available. Typically if they have not contained the fire after one or two hours, the Incident Commander will request help from the Emergency Manager, who can request mutual aid (other municipal fire departments), state aid, or federal aid, as needed. The Emergency Manager may also own useful firefighting resources unavailable to the Incident Commander. [Reed, Metcalf, and Louthan, conversation with author]

In order to make good decisions, Incident Commanders at a wildland fire must have certain information. First, he must have an accurate picture of where the forward burning line, or the fireline, is located. A wildland fire typically spreads to an area of three to four acres by the time firefighters arrive. If the fire is located quickly enough the initial attack may contain the fire with negligible loss of property. Second, the location of the fire in relation to natural fire breaks such as roads is critical to the allocation of resources around the fire. Third, the Incident Commander

must have an accurate picture of how the fire will spread. Currently, the Incident Commander must determine this picture through intuition and experience. A variety of unknown conditions, such as winds at various altitudes, accurate fuel estimates in the vicinity of the fire, or exact topography of the area, will limit the accuracy of the Incident Commander's assessment of the fire spread characteristics. Fourth, the evacuation of any wildland-urban interface, such as a nearby house or trailer, will be an Incident Commander's first priority when arriving at the scene. Therefore, any new knowledge of nearby structures or people would drastically change an incident commander's firefighting plan. [Bradley, conversation with author]

A volunteer fire department will have little or no money for the purchase of equipment for gathering any of the unknown variables of fire spread, namely weather, fuels, and topography. However, many of these variables could be determined long before the fire occurs. This gap in situational awareness has driven several state and federal programs that regularly gather information and determine the general wildland fire risk over a large area. One such program in Oklahoma is OK-FIRE. This system gathers meteorological information from the 155 reporting stations across Oklahoma that make up the Mesonet. It also utilizes the National Weather Service's 84-hour North American Mesoscale (NAM) weather prediction model. OK-FIRE then combines this current and predicted meteorological information with the latest estimates of fuel conditions in various locations across Oklahoma to determine the fire risk in the vicinity of each Mesonet weather reporting station. [Carlson, et al. 2003]

Systems such as OK-FIRE are limited by the scarcity of the reporting stations, the infrequency of fuel load and fuel type surveys, and the inaccuracy of indirect fuel state measurements. Nonetheless, OK-FIRE has proven to be a valuable tool that is currently used by municipal fire departments across the state to determine fire risk, make short-term staffing decisions to match the risk, and communicate that risk to the general public. [Carlson, et al, 2003]

A good assessment of fire danger must integrate information about the three major environmental drivers of fire spread: topography, fuels, and weather. [Carlson, et al. 2003] Current models take advantage of online surveys of ground topography, such as the USGS 30 meter digital elevation models, or even satellite-based canopy-penetrating radar, such as the Spaceborne Imaging Radar-Band C (SIR-C), or airborne LiDAR sensors. [Blair, et al. 1999, Iriarte, 2015] Topography is the most constant of the environmental drivers, but the same remote sensing techniques used to map ground topography can also map the changing conditions of canopy fuels. [Saatchi, et al. 2007]

The next variable, fuels, can be estimated through sample destructive harvesting, ground survey, or multispectral remote sensing. Harvesting is the most accurate, and it involves gathering all vegetation within a specified plot into bundles, weighing the bundles, drying the bundles in an over until all the moisture is removed, and then weighing the dry bundles again. This process gives the best indications of fuel weight and moisture content, however it is incredibly time intensive and is destructive to the plot measured. [Schmidt, 2014]

Ground survey is the oldest technique of producing fuel maps. The fuel types and relative quantities are estimated by experts who visually inspect each area. It is less time intensive than destructive harvesting, but the results are subjective since they depend on the observer's opinion. [Hornby, 1935]

Satellite remote sensing has been used to create fuel maps of many parts of the world, including the entire United States, that are readily input into national-scale fire spread and fire danger models. Airborne color imagery has likewise been used to identify individual plant species or classes over a smaller scale with less uncertainty, but at the cost of a higher workload by the observer. [Schmidt, 2014]

Accurate fuel loading maps are important for more than just fire danger maps or predictive wildfire models. Communities on the Wildland-Urban Interface (WUI) are using fuel

information for strategic fire mitigation practices. Reliable knowledge of the special distribution of fuel can highlight at-risk areas, allowing for informed placement of reduction measures. [Krasnow et al, 2009]

Prescribed burns are one means of managing the wildfire risk in areas that have built up significant amounts of dry, burnable fuel since their most recent fire. Prescribed burning is defined as the controlled application of fire to a specific land area to accomplish planned resource managements objectives, such a reducing surface fuels. Wildfire risk assessment is based on, among other variables, the fuel type, fuel load, and fuel state. Fuel type is determined visually by a trained observer as the fuel that will be the main carrier of the fire. The most accurate way to determine fuel load and state is destructive harvesting. Through this method, all plants in an area are clipped at some short distance from the ground, and the total clipped vegetation is weighed, oven dried for days or weeks, and reweighed. The dry weight is the burnable fuel load, and the amount of water removed by over drying determines the fuel state. This method is only useful for limited research environments and would not be used for local wildfire risk assessment. A typical risk assessment for a prescribed burn may involve an estimation of fuel load as low, medium, or high and an estimation of fuel state as the percentage of fuel available to burn. The first would be based on the assessment of a trained observer, and the second would be based on fuel moisture, fuel size, fuel arrangement, depth of the fuel bed, days since last precipitation, and long-term drought conditions. [SCFC, 2014] Because all three of these variables are determined by human observation, their accuracy is severely limited. As a result, risk management and planning must be significantly more conservative than it would if accurate, reliable measurements could be taken. Fast, accurate surveys of fuel type, state, and load could make planned burns more efficient and less dependent on weather conditions than they currently need to be.

Predictive fire spread models are sometimes used for emergency management planning or for managing risk at large prescribed burns. Unlike fire risk assessment tools like OKFIRE, these

models are largely empirical-based rather than physics-based, and are therefore limited in accuracy when extrapolated to previously unobserved conditions. Current models are country- or region-specific. For instance, a model developed in Canada would perform poorly in New Zealand. They are calibrated using predefined fuel categories, and will not capture the differences associated with uncalibrated fuels or even variations between plants of the same species. They are designed to predict rate of spread and intensity only, and they cannot accurately predict other fire behaviors like "catching the crowns," a term for fire ascending from the ground to the forest canopy. [Arroyo et al, 2008] A physics-based model would be much more complex, requiring accurate assumptions about the wind currents in the vicinity of the fire. However such a model would only be limited by the accuracy of the input conditions. One required input for any wildfire predictive model is the horizontal distribution of Above Ground Biomass (AGB), or fuel loading. In order to more accurately predict a fire's behavior, a model would also need information about the vertical distribution of fuel loading, such as canopy height, canopy base height, and canopy bulk density. These variables are difficult to measure, and they are often provided as generalities of a plant species or functional group and age. Even a uniform vertical distribution of biomass is sometimes considered reasonable. [Saatchi, et al., 2007]

This survey achieves objective 1.

2. WILDFIRE AIRCRAFT

The National Interagency Fire Center (NIFC) operates two fixed-wing aircraft to provide situational awareness for asset management around major wildfire events in the United States. These aircraft supplement satellite hyperspectral imagery with night-time thermal infrared (TIR) imagery collected from a mission altitude of 10,000 feet Above Ground Level (AGL). These

sensors, though they provide higher spacial resolution than satellite imagery, are still too coarse to spot individual small hot spots, which may saturate a larger pixel, giving an indication of a larger fire threat than what actually exists. Because of this issue, mop-up operations are often supported instead by handheld TIR sensors carried onboard low-altitude rotorcraft. Both of these techniques (broad area observation from fixed-wing aircraft or small area observation from rotorcraft) are manpower intensive, with a dedicated crewmember required for sensor operation and communication with the ground. A UAS by necessity would automate some of these processes, reducing the required manpower while increasing endurance and reducing fuel costs. [Ambrosia, et al., 2011]

From 2006 to 2009, NASA flew two modified General Atomics Predator over 55 major wildfire events in both day- and night-time as part of the Western States UAS Fire Imaging Mission. [Ambrosia, et al., 2011] The first of these aircraft, a modified Predator B called "Altair," was designed to demonstrate the capabilities of an UAS performing high-altitude Earth science missions, but it was also flown over the . The aircraft could carry a sensor payload of up to 750 pounds. In October, 2006, the Altair was equipped with a pod-mounted infrared imaging sensor under the fuselage and flew several missions Esperanza fire to support firefighting efforts there. [NASA Armstrong, 2014]

The second Predator B deployed by NASA as part of this mission, the "Ikhana," was first flown in 2007. It was able to provide incident commanders with near-real-time GIS products for visualizing the fire front through an internet distribution (10 minute latency to process imagery and distribute GIS information over the internet). The aircraft was able to reduce the latency greatly by utilizing an Applanix, Inc. 'Position and Orientation System for Airborne Vehicles (POS-AV)' model 310 system to tag all images with the precise GPS position and inertial orientation of the sensor. This information eliminated a tedious post-processing step and gave a "forward" solution that had a RMS error of only 2.5 pixels when compared to post-processed

information. Onboard processing allowed the aircraft to communicate only processed information to the ground through the limited communication bandwidth. The entire payload of the instrumented Ikhana weighed 2400 pounds. [Ambrosia, et al., 2011]

NASA was able to attain an FAA Certificate of Authorization (COA) for each aircraft by filing flight plans with as little as 48-72 hours' notice for scheduled flights over controlled burns. On the other hand, after the Ikhana was delivered in January 2007, the first COA for the new aircraft tail number was not issued until August of that year. The Ikhana operators had to fly the flight plan similarly to pilots flying on an Instrument Flight Rules (IFR) flight plan [Federal Aviation Regulations, 91.117], with all deviations requiring a clearance from the FAA Air Route Traffic Control Center (ARTCC) via verbal radio communications. [Ambrosia, et al., 2011]

In the summer of 2014, in a partnership between the Alaska Fire Management office and the US Army, an RQ-7 Shadow battalion flew three flights to determine the best practices for employing these combat aircraft in fighting wildfires. The aircraft and operators were evaluated based on their (1) ability to create an IR map of a large scale fire progression, (2) ability to integrate into a fire management team, (3) ease of use, (4) response time, and (5) potential to operate independently over unstaffed burning on military lands and send status reports and hotspot locations to fire managers. The UAS was only allowed to fly at night to avoid any firefighting aircraft flying during the day, and had to develop a course of action for leaving the airspace if a night medivac helicopter launched. [Hill, 2015]

The systems on the Shadow were sufficient to gather the information important for tracking a fire line and finding hotspots. The biggest challenges came from training the crew in the new mission. The crew and the liaison worked together, especially during the second and third flights, to fit the abilities of the aircraft with the needs of the incident commander. Some capabilities, such as geotagging images with latitude and longitude or plotting a search pattern using the

ground station's computer after takeoff, required some improvisation from the pilots, who were trained for but unfamiliar with the capabilities not typically used on a combat mission. This split attention could be dangerous in a busy airspace, especially given the already limited situational awareness of most UAS. The author concluded that embedding an experienced firefighter with the operators would eliminate many of the problems inexperienced flight crews would experience as various agencies develop procedures and training plans for this new mission. [Hill, 2015]

Large UAS like these are beyond the scope of this paper; however some of the problems experienced apply to small firefighting UAS as well. Concerns over the danger of mixing manned and unmanned aircraft in the same crowded, uncontrolled airspace around an active fire has grounded fire-aviation assets in the United States, and a fire service deputy commissioner in Australia has threatened to do the same in New South Wales. [Bruce, 2015] In the United States, these areas are often protected from sightseeing aircraft by the FAA's Temporary Flight Restriction (TFR) program. [Federal Aviation Regulations, 91.137(a)] Conflicts like this could be avoided in the U.S. if non-participating UAS operators will monitor and respect these restrictions to flight, and participating operators are able to stay situationally aware of other aircraft in the airspace.

Large, military UAS like the Predator are inappropriate for commercial use because of a number of practical barriers. These systems lack the sophistication, reliability, safety, and flexibility expected in civilian aircraft operating in the National Airspace System. They therefore require a large investment in capital and training to operate. [Grossman] Conversely, components marketed to UAS hobbyists are not designed or tested as rigorously as would be required for widespread commercial applications.

3. PASSIVE SENSORS

One solution to the wildfire detection problem is the use of satellite imagery in the color and infrared spectrums to locate hot spots on the ground. Satellites can monitor large areas at regular intervals to detect sufficiently large fires in remote areas. Because of the limited spatial resolution of satellite imagery, small fires will likely go undetected. Atmospheric phenomena such as high humidity or cloud cover could absorb most or all of the color and infrared light emitted by a fire before that light could reach an orbital satellite. Satellites fly fixed orbital paths, often created for purposes other than firefighting, and therefore may not be available for a particular area at a particular time. The cost of launching and maintaining an orbital satellite has prohibited their use for dedicated firefighting applications, and therefore the communication time with the end user often makes them makes the data unusable for all but large federal fires.

Satellites have also been used to gather information for large-scale predictive models of fire behavior. The LANDFIRE database was a federal program in the United States to create a nationwide map of fuels and vegetation using satellite-based remote sensing. This program was limited by a moderate spatial resolution (30 m) and is not suitable for modeling fires on the local level. It also has no way of determining canopy characteristics, and so the data was supplemented with Landsat imagery. However this method also tends to underestimate canopy bulk density and canopy base height. [Erdody and Moskal, 2010]

The Normalized Difference Vegetation Index (NDVI) has also been used to determine plant health and moisture content on the ground using hyperspectral imagery from satellites such as NASA's MODIS [Rouse, et al, 1973]. By measuring the reflectance of a Near Infrared (NIR) and

red bands captured by MODIS, one can calculate NDVI, which is an estimate of photosynthetically active biomass, as:

$$NDVI = \frac{\rho_{857} - \rho_{645}}{\rho_{857} + \rho_{645}}$$

Where ρ_{857} is the reflectance at 857 nm (NIR), and ρ_{645} is the reflectance at 645 nm (red). NDVI has a strong correlation with moisture content in grasses, but the extremely low spatial resolution of MODIS imagery (500 m) makes it difficult to use for determining local fire risk. [Dennison et al, 2005]

Krasnow et al, [2009] makes the case for more precise fuel maps to predict fire spread and plan for fire mitigation practices. The paper used two historic Colorado wildfires (Overland in 2000 and Walker Ranch in 2003) to evaluate the performance of FARSITE simulations using LANDFIRE national fuel maps and maps developed through the method described in the paper. This method used sampling and predictive modeling to create detailed, local fire maps for the areas burned in these fires. Simulation showed that the LANDFIRE map greatly underestimated the extent of the fire, predicting only 40.3% and 77.7% of the area that was burned in the actual fires. The local fuel maps improved that performance to 88.2% and 91.4%, respectively. In the wind driven Overland Fire, the LANDFIRE map predicted an average spread rate of 3.58 m/s whereas the local map predicted a more dangerous 5.75 m/s average spread rate. The author points out that some of this improvement is likely due to the iterative calibration process used to correct the map to match historic fire behavior. This step was necessary to create an accurate metric with which LANDFIRE maps could be compared. However, the paper points out that the predictive model was only able to account for 56-62% of the variability of predicting four fuel parameters used by FARSITE. The simulation may have performed even better if fuel parameters could have been directly measured immediately before the fire.

Fire spotting towers are a low-cost solution to the wildfire detection problem. These fixed towers are deployed in remote areas to monitor atmospheric conditions in the immediate vicinity of the tower and provide warnings of nearby fires. Some towers are equipped with CCD cameras to monitor large tracts of land with or without a human observer. Image and video processing techniques can provide autonomous smoke detection from up to several miles away, reducing an observer's workload. However, commercial software available today is still less effective than a trained observer and produces many more false alarms. [Matthews et al, 2012] Though less expensive than a satellite at about $30,000 per tower, a fire tower can only observe the area around it, and its view can be obscured by natural or manmade features. As the price of processing and communication systems goes down these towers will become more effective, but they will still be limited to line-of-sight observations from the tower.

Davenport [2012] tested the effectiveness of multispectral video for smoke detection. By correlating visible, cooled midwave IR, and cooled longwave IR videos, he was able to perform a Principle Component Analysis (PCA) to find the most significant color channels for smoke identification. According to his findings, smoke was most easily detectible in the seventh principal component of a two frame, five channel PCA (10 principal components in all). The seventh principal component is made up almost exclusively of red, green, and blue channels, with very little contribution from midwave or longwave IR. A duplication of the technique with only red, green, and blue channels obtained the same results. According to these results, midwave IR and longwave IR do not provide significant information for smoke plume detection.

Mallinis et al [2014] evaluated three hyperspectral satellite systems for their ability to gather information that could determine fuel types in the University Forests of Taxiarchis in central Macedonia. Using machine learning techniques, they compared the ability of the Quickbird, Landsat TM, and EO-1 Hyperion imagery to accurately identify the fuels in the test set after being trained on the known set of fuels. They found that the high spatial resolution of the

Quickbird imagery may be more decisive than the high spectral resolution data of Landsat TM and OE-1 Hyperion for Mediterranean fuel type mapping, even without including the contextual information and texture and shape clues that have been shown to improve Quickbird's classification results. Of course, such a simple test is not a replacement for a human classifier. However it does highlight the limitations of the extremely low spatial resolution satellite imagery when attempting to construct a fuel type map.

4. ACTIVE SENSORS

Saatchi, et al, [2007] tested the idea of using radar remote sensing from an airborne or spaceborne platform to determine fuel characteristics. They were able to survey large swathes of Yellowstone National Park using an AIR-SAR (Synthetic Aperture Radar) system mounted to a NASA DC-8. Spatial resolution varied from 5 to 10 meters for different bands and different tests. The paper found a strong relationship between the measured radar backscatter and specific categories of above ground biomass useful for computational computer models (crown and stem biomass, canopy fuel weight, and foliage biomass) by fitting the applicable backscatter signals in dB to the Log of the fuel component desired, and second order Log fits were also provided when they improved the accuracy of the plot significantly. Some sources of error were the uncertainty of the canopy height or the ground relief of the terrain below the canopy, both of which are difficult to attain without ground measurements. Accurate measurements of topographical variations would be required to correct backscatter measurements. These measurements can either come from recent, detailed surveys or from a second sensor to measure surface elevation.

Erdody and Moskal [2010] tested a method of combining passive optical and active Light Detection And Ranging (LiDAR) measurements to form a more accurate estimate of forest

canopy composition of Ponderosa Pine in Ahtanum State Forest in Washington State. The apparatus used employed high-definition digital color near-infrared (NIR) camera coupled with discrete-return LiDAR sensor to determine the strengths of individual measurements compared to a model that combines information from both sensors. The camera was mounted to a fixed-wing manned aircraft, and provided a spatial resolution of 61 cm, which was a large improvement over the 30 meter Landsat or 2 meter Quickbird satellite imagery, however it is still too low to determine features for species identification or structure from motion. The paper concluded that the color NIR imagery added only about 3 to 4% accuracy to the LiDAR estimates of canopy characteristics. However, color NIR information can also be used to identify species, evaluate plant health, estimate moisture content, or other characteristics that LiDAR information cannot estimate. Also, the large, heavy LiDAR system employed in the study would not be feasible on a small UAS, whereas small UAS routinely carry lightweight high-resolution cameras with a spatial resolution much smaller than 61 cm, mainly due to the lower altitudes at which UAS generally fly. Smaller, less sophisticated LiDAR systems would not provide as much accuracy, however penetrating LiDAR information could supplement imagery to identify features below the top of the canopy.

Iriarte [2015] used a LiDAR device mounted to a UAS with a 3 meter wingspan to determine the ground characteristics below Amazon rainforests in Brazil. This project plotted LiDAR reflections, filtered out the reflections that came from the canopy, and mapped out the ground reflections to find the relatively small remains of 1000 year-old structures. Small, cheap LiDAR could also be carried by a wildfire UAS in order to map small changes in the topography in order to get a more accurate picture of the canopy height and the local ground slope.

5. FIRE AND SMOKE DETECTION ALGORITHMS

A smoke plume can be detected a number of ways. Chemical detectors, such as household smoke detectors, are often used to detect carbon monoxide or carbon dioxide in the vicinity of the detector quickly and with great accuracy. A transportation delay exists with these point sensors because they cannot detect a smoke source far away from the detector until a sufficient amount of smoke reaches the detector.

Another solution takes advantage of how smoke absorbs, reflects, and transmits light. If a laser is fired at a smoke plume, certain wavelengths will be either absorbed or reflected back at the source. These optical smoke detectors collect a sample of the ambient atmosphere and fire a laser through it and into a detector or receiver on the other side. If the gas sample reflects or absorbs enough of certain wavelengths, then an alarm is triggered. [US Patent 08/120,947, 1995]

Optical smoke detectors are often attached to towers to test for various chemicals, but these systems are expensive and have a short range, requiring a dense arrangement for effective coverage. Handheld sensors are available, but their low sensitivity limits them to simple point sensing. Long range sensors are available, but they are the size of a semi-trailer and are not practical for surveying large areas of wildland. At Oklahoma State University, the *Sensorcraft* carries an optical chemical detector on a small UAS to survey an area for high levels of a particular gas, which could indicate anything from a smoke plume to an invisible gas leak from a natural gas pipeline. [Mitchel, 2015] Point smoke detection techniques like these are outside the scope of this paper and will not be evaluated.

Figure 3 - OSU Sensorcraft, equipped with a small optical point chemical sensor.

Vision-based smoke detection has considerable advantages over other fire and smoke detection methods. A vision sensor is a volume sensor rather than a point sensor, and therefore the hazard is detected without a transportation delay and from a safe distance. Despite considerable research in this area, vision-based smoke detection is still an open problem. Variability in the sequence lighting, video fogginess, outdoor background, and moving objects with characteristics similar to the smoke make background estimation difficult. No primitive features such as motion, color, edge, shape, or reduction in background energy uniquely describe the smoke. It is also difficult to model the appearance of smoke.

The topic of autonomous fire and smoke detection through image processing techniques has been a subject of study for over a decade, but almost all of the techniques described in literature assume a fixed camera and little if any camera flicker. [Ojo, et al. 2014] These conditions rarely occur even with a CCD camera mounted to a fire tower, and therefore the individual techniques are less effective in this scenario. A camera mounted to a constantly moving UAS makes these

assumptions invalid under all but perfect conditions, and many of the techniques simply have to be discarded.

The first smoke detection algorithms used background subtraction or color discrimination to detect smoke plumes. [Ojo, et al. 2014] Though these techniques can be implemented in real time, they have proven too basic for an accurate smoke detection without excessive false alarms. Background subtraction, or frame differencing, involves subtracting some saved background image from the current frame and noting the differences. This background image can be the previous image, the first image in a sequence, an image updated by each successive frame, or some average image across a training set of frames. Background subtraction techniques are effective in urban settings where the background does not change significantly with each frame, however they must increase in complexity in the presence of a constantly changing background, such as waving grass or blowing leaves common in wildland backgrounds. [Dawson-Howe, 2014] To be effective for smoke detection in wildland environments, the camera must store a pre-smoke background image from the same orientation, position, and time of day as the current frame. Tower cameras will update their background slowly throughout the day in order to ignore subtle changes in illumination, but the limited flight time of a UAS would make this hours-long process impractical.

Color discrimination involves using RGB, [Chen, et al., 2004] HSV, [Chen, et al., 2006] or some other color space values to determine the presence of smoke in a pixel. The cutoff for classifying a pixel as smoke can involve a fixed threshold of values, an updating threshold of values, or a probability distribution based on a training set of images. Though some improvement can come from choice of color space, [Damir, et al. 2009] it is negligible when compared to the number of false alarms and missed detections that occur when evaluating the algorithm with an image outside of the training set. When evaluating each image as a whole, especially under conditions

not included in the training set, these algorithms perform worse than a human observer. When evaluating individual pixels their results are completely unreliable.

Chen, et al. [2004], created a chrominance test with only one static threshold, so that the thresholds were relative to the other chrominance values, not absolute thresholds. In this test, a pixel was fire colored if all of the following were true:

$$R > R_t$$

$$R \geq G > B$$

$$S \geq (255 - R) * \frac{S_t}{R_t}$$

where R, G, and B are the Red, Green, and Blue pixel values, respectively, R_t is some fixed threshold for Red, S is the Saturation value, given as:

$$S = 1 - \frac{1}{R + G + B}[min(R, G, B)], \qquad 0 \leq S \leq 1$$

and S_t is the value of S when $R=R_t$.

Chen, et al. [2004] also includes a chrominance-only smoke test involved testing for the greyness, or the closeness of the R, G, and B values. The paper gives the following formula:

$$R \mp r = G \mp g = B \mp b$$

$$0 \leq r, g, b \leq a$$

where a is a fixed threshold for the minimum greyness of smoke.

Celik, et al. [2007] provided a five step level flame test using chromatic values. The first two steps used only relative thresholds, and the last three are designed to be illumination independent.

$$R(u,v) > G(u,v) > B(u,v)$$

$$R(u,v) > R_{mean} = \frac{1}{k}\sum_{i=1}^{k} R(u_i, v_i)$$

$$0.25 \leq \frac{G(u,v)}{R(u,v)+1} \leq 0.65$$

$$0.05 \leq \frac{B(u,v)}{R(u,v)+1} \leq 0.45$$

$$0.20 \leq \frac{B(u,v)}{G(u,v)+1} \leq 0.60$$

where k is the total number of pixels in the image.

More recent research in flame detection involve the temporal characteristics of fire (i.e. slow spread rate, high frequency flicker on the boundary) that break down when the camera is far away from the fire or the camera is moving. There has been very little success in spotting wildfires from the color characteristics of the flame, and so an evaluation of these techniques for implementation into a wildfire UAS is beyond the scope of this paper. By far, the most successful method of spotting a wildfire from aerial imagery has been viewing infrared bands to detect relative hot spots. This method has the potential to find fires that are obscured by smoke or obstacles or even roots burning under the soil. [Hill, 2015]

A more complex version of color discrimination is testing for greyness. In general, the color of a smoke plume is some level of grey, ranging from white to black depending on the stage of the fire. In RGB color space, this means that the values for red, green, and blue, denoted by R, G, and B are close to each other. Chen, et al. [2004] includes the following chrominance-only smoke test involved testing for the greyness:

$$R \mp r = G \mp g = B \mp b$$

$$0 \leq r, g, b \leq a$$

where "a" is a fixed threshold for the minimum greyness of smoke. Yuan [2008] gives a similar test, which is easier to implement on MATLAB:

$$max(R, G, B) - min(R, G, B) < TR$$

where TR is a predefined threshold. However, certain conditions (i.e. sunrise, sunset, colored smoke, greyish moving objects, heavy mist) can cause the assumptions associated with fixed thresholds to break down. For instance, thick fog may trigger false alarms or obscure actual smoke. Reflections of fire or the sun may also color the smoke, making it fail the greyness test.

As recently as 2013, Yoon, et al. developed a smoke detection test using fixed thresholds that was supposed to eliminate fog and clouds from the pool of false positives. The paper evaluated 5 smoke video sequences, determining smoke pixels by subtracting from a background that was updated through a Gaussian Mixture Model once every minute for 30 minutes. They found that in the HSL color space, 90% of the smoke pixels had a Saturation (S) value from 0-60, and 95% had a Lightness (L) value from 40-140, both on a scale from 0-255. According to this paper, detection times were under 2 minutes, including a thin smoke plume representative of an early fire, with minimal false alarms from fog and clouds.

Töreyin, Dedeoglu, and Çetin [2005] developed an effective five step method for detecting smoke within about 100 meters of the camera. After segmenting potential smoke regions through motion detection, this method uses a background subtraction of the spatial wavelet transform to detect a decrease in high frequency energy, which is indicative of the "blurring" experienced when observing a background through light smoke or haze. The high frequency energy of a pixel, E(i,j), is given by:

$$E(i, j) = LH(i, j)^2 + HL(i, j)^2 + HH(i, j)^2$$

where LH, HL, and HH are the high frequency subbands of an image, and (i,j) represents the pixel located at the i^{th} row and j^{th} column. Candidate regions that lose high frequency energy between subsequent frames are checked for a loss of U and V chrominance values in the LUV color space, an indicator of the "graying" effect that the addition of smoke cover often creates. Finally, the boundaries of the remaining candidate regions are checked for a one to three Hertz flicker observed in smoke boundaries.

This algorithm performs well in the majority of scenarios; however there are several conditions under which it will fail to identify smoke. If the background has very little texture then the smoke will not blur it, and in some cases the smoke will actually increase the high frequency energy of the region. [Chen, et al. 2013] Moving shadows tend to reduce the U and V like smoke does, and if the sun or the fire is reflecting off the smoke and giving it a red hue then the smoke will likely not decrease the red value of the pixel and the region may be discarded during this step. If the smoke is too far away from the camera then any small flicker of the boundary will not be observable, and so the range of the algorithm is limited by the resolution of the video and the inherent flicker and jitter associated with all cameras and camera mounts. Photo compression methods, like .jpg, often use discrete transforms to reduce the memory requirements by filtering out the high frequencies [Gubbi, et al. 2007], so a system that uses this approach would require a camera that outputs uncompressed images and videos. Regardless of these shortcomings, the Töreyin, et al, technique can perform well across a wide range of conditions and is still considered the standard upon which other new techniques are often compared. The high computational complexity of the algorithm has driven researcher to develop algorithms that achieve similar of better results with algorithms that can be processed in real time.

Yuan [2008] proposed a method that utilized optical flow to identify the unique movement of smoke in an image. Optical flow is built on the assumption that light intensity (I) is conserved, and therefore:

$$I(u+\Delta u, v+\Delta v, t+\Delta t) - I(u,v,t) = \frac{\delta I}{\delta u}\Delta u + \frac{\delta I}{\delta v}\Delta v + \frac{\delta I}{\delta t}\Delta t + HOT = 0$$

for each pixel in the image. It uses frame differencing to determine the change in intensity between two subsequent frames $\left(\frac{\partial I}{\partial t}\right)$ and then determines the x and y derivatives within the image using a least squares or some other fit with the surrounding pixels. Because the equation is applied to a digital image with discrete pixels, the movement in the image must not exceed the size of a pixel in order to arrive at a useful solution. Though the theory is based on a false assumption (intensity is rarely conserved in a moving image due to changes in the image brightness and movement toward or away from the light source), the illumination change between two subsequent frames is usually very small, and the calculations converge to a useful solution in the vast majority of problems. [Dawson-Howe, 2014]

In Yuan's technique, optical flow was collected over several frames as an oriented histogram, and regions that showed a general upward motion were classified as potential smoke, taking advantage of the buoyancy of smoke. This one step in particular was able to eliminate many moving objects that would have created a false alarm for other algorithms. Optical flow is a powerful tool for smoke detection, and it provides a means to detect smoke in the presence of camera ego-motion. However it is computationally expensive and therefore currently unsuitable for real time implementation.

Yuan's was not the first paper to attempt to use optical flow to detect smoke in a video. Kopilović, et al. [2000] studied the use of low resolution 180^o panoramic lenses for surveillance and smoke detection. The study separated the optical flow orientations into discrete bins and calculated three characteristics: Entropy, Variation, and Maximum-norm. By testing smoke and non-smoke motion blocks between two consecutive frames of a video, the paper found that Entropy, defined below, showed the best discrimination of smoke motion versus rigid body motion:

$$e_n(f) = \frac{-1}{ln(n)} \sum_{i=1}^{n} f(i) ln\big(f(i)\big)$$

where e is the Entropy, n is the number of discrete orientations considered on the interval (0,π], and f(i) is the distribution of the i^{th} orientation, on the interval [0,1]. This result allows for a quick algorithm that can be implemented in real time for low resolution video; however it still assumes a fixed camera since the random motion of a UAS in turbulence could easily increase the entropy of the background beyond some fixed threshold for smoke. Also, while indoor backgrounds rarely move, outdoor backgrounds are full of non-rigid motion that may have higher Entropy than a smoke plume.

NASA Armstrong [Ambrosia, et al. 2011] deployed the Ikhana UAS over several fires from 2007-2009 in part as an attempt to autonomously detect, identify, and locate flare ups following fires, an operation often referred to as "mopping up." The Ikhana was equipped with an AMS-Wildfire, a high spatial resolution multispectral sensor that was capable of determining radiance in some Thermal Infrared (TIR) bands for temperature measurement, as confirmed by laboratory calibration. The aircraft used the following thresholds to create a fire alarm:

$$Band\ 11(3.60 - 3.79\mu m) > 360° K$$

$$Band\ 12(10.26 - 11.26\mu m) > 290° K$$

$$Band\ 4(0.76 - 0.90\mu m) < 0.4$$

The third threshold was used only during the day, when reflectance from the Sun was likely to create false alarms. This step eliminates any highly reflective objects as false alarms. This technique was able to quickly identify still-burning objects on the ground at night and notify firefighters on the ground to extinguish them. [Ambrosia, et al. 2011] The algorithm is a natural extension of traditional mopping up operations, where thermal video is often taken by firefighters

either on the ground in helicopters above the burn in order to identify hot spots not visible to the naked eye. These experiments proved the usefulness of TIR information for hot spot identification from the air, however without additional color information or highly precise orientation information TIR alone is difficult to analyze.

Chen, et al [2013] used the Gray Level Co-occurrence Matrix (GLCM) to identify pixels within a smoke region by quantifying the discontinuities in the vicinity of each pixel. Similar to the blurring noticed by Töreyin et al [2005], this paper assumes that as smoke occludes a region the number of discontinuities within that region will decrease. Like the high frequency energy observation, this technique will often fail in the presence of a uniform-color moving object, a textureless background, or smoke very near the camera, where rich edges of the smoke can increase the background texture.

Ko, et al [2013] identified two spatiotemporal features for determining smoke regions in a video. The paper states that the smoke boundary has a distinguishable pattern in a spatial Histogram of Oriented Gradients (HOG) within a single frame because of the upward diffusion characteristics of smoke; however it does not describe the pattern so the effectiveness of this feature is difficult to confirm. Additionally, the paper generated a Histogram of Oriented Optical Flow (HOOF) for each pixel in a candidate block over 100 frames. The assumption is that over time, the net optical flow of a smoke pixel is up and left, up, or up and right, as indicated by the discretized range of motion that optical flow can resolve. Another assumption of this technique is that either the camera is motionless or its motion is cyclical so that by the end of the process it will be located and oriented as it was at the start. As in Yuan [2008], it may be possible to use the HOOF to estimate the motion of the camera, but optical flow calculations are very computationally expensive at high image resolutions.

Wang, et al [2014] introduced the idea of using swaying (smoke moves more at the top than at the bottom) and diffusion (the smoke diffuses as it rises, so the top has fewer characteristics of smoke than the bottom) features to identify smoke blobs in an image. The swaying tracks the centroids of the top and bottom halves of a large smoke colored blob through several frames. A rigid moving object such as a car would give similar results between the top and bottom halves, whereas the bottom half of an example smoke plume moved only 70% as much as the top over 5 frames. Two specific examples, a man exercising and a plastic bag tied to a vent on the ground, showed similar results. To eliminate potential false alarms, the paper also calculated the diffusion of the blobs using the GLCM. By summing the elements along the main diagonal (exact matches) and dividing by the total number of elements, these normalized matching ratios could be compared. The paper concluded that if 65% of the bottom pixels match (main diagonal on the GLCM) and if the top half has less than 96% of the matches that the bottom has, then the region is a good candidate for smoke. The swaying characteristic may have some benefit to a camera that is allowed to translate but not rotate. As long as the motion between frames is small enough that a candidate smoke region can be identified in consecutive frames, the difference in motion between the top and bottom could be found, though the ratio may break down when the camera motion is much greater than the smoke motion.

Dark channel priori is a technique that has been used for automatically normalizing the ambient light in an image. Ligang, et al [2014] proposed using this technique to identify smoke regions by noting the increase in the minimum RGB value within a smoke region. This technique assumes that inside any background region $\Omega(\mathbf{x})$ centered at the pixel identified by vector $\mathbf{x}$, which is not occluded by smoke, there are always pixels for which the dark channel $J^{dark}(\mathbf{x})$, defined below, is very small, potentially even zero. This means there are some pixels inside each region for which one either the Red, Green, or Blue values are considerably small. When the

smoke covers that background region, the dark channel will increase, and this phenomenon could be used to find smoke regions in the current frame. The dark channel is calculated as:

$$J^{dark}(\boldsymbol{x}) = \min_{c\in\{R,G,B\}}\left(\min_{y\in\Omega(\boldsymbol{x})}\left(J^{c}(y)\right)\right)$$

6. FUEL MAPPING ALGORITHMS

McCree [1972] determined the Photosynthetically Active Region (PAR) of the electromagnetic spectrum by measuring the response of 22 plant types to electromagnetic radiation between 350 and 750 nm. He determined that all plants absorbed ultraviolet, visible blue and visible red light, with a noticeable dip in the range of visible green light and a sharp drop at the boundary between visible red and near infrared, as illustrated by the following figure.

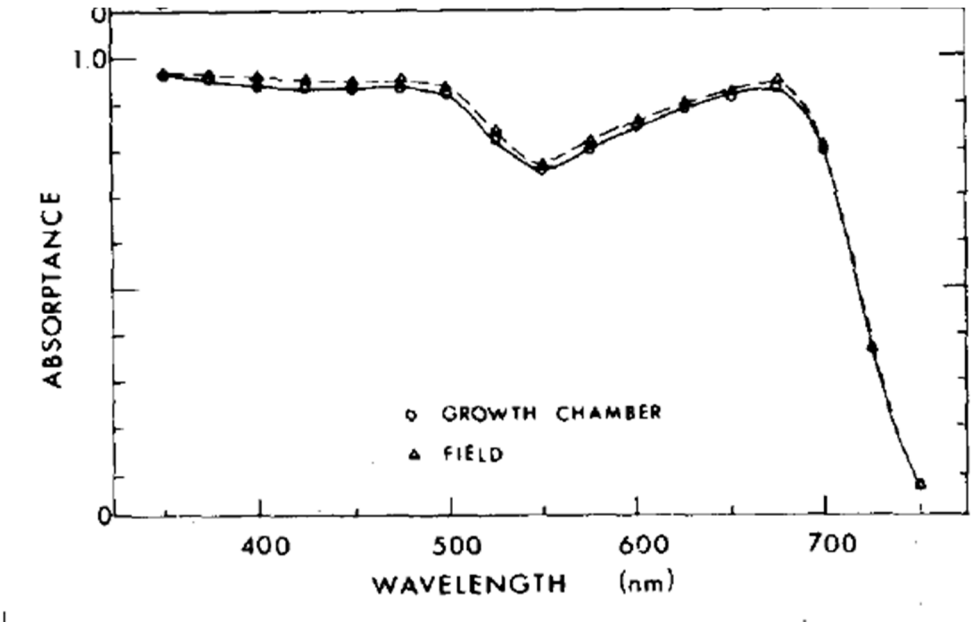

Figure 4 – Average absorptance characteristics of 22 plant types [McCree, 1972]

Rouse, et al. [1973] used LANDSAT spectral information to develop this PAR into a useful index to determine plant health or density. The paper determined that healthy, dense vegetation exhibited high NIR reflectance and low red reflectance, whereas unhealthy or sparse vegetation exhibited low NIR reflectance and high red reflectance. This study also created a so-called "greenness" measures called the Vegetative Index (VI) (later called the Normalized Difference Vegetative Index, or NDVI), which could be used to monitor range lands and wheat crops, for seasonal changes. VI combines the LANDSAT channels MSS7 (NIR) and MSS5 (RED) using the following equation:

$$VI = \frac{MSS7 - MSS5}{MSS7 + MSS5}$$

Tucker [1979] evaluated several spectral indices and ratios like Rouse's VI. He used regression techniques to compare 18 spectral variables using IR-RED or GREEN-RED combinations against six canopy characteristics. The study found that IR-RED reflectance characteristics were a much better indicator of vegetative qualities that GREEN-RED. Also, although VI was a good indicator of photosynthetic vegetation, it reached an asymptote in high green biomass situations. The significance of different IR bands, namely 0.75-0.80µm, 0.80-0.90µm, and 0.75-0.90µm were also evaluated and found to be extremely similar.

Running, et al. [1995] proposed that vegetation could be classified into one of six categories by using remote sensing measurements to determine whether the plants within the plot were perennials or annuals, whether the perennials were evergreen or deciduous, and whether the leaves were broad or needle-like. Plants could be categorized into annual or perennial by tracking a 12-month history of above-ground biomass, and likewise the evergreen versus deciduous characteristics could also be identified using a 12-month history of "greenness," such as NDVI. The third classification, leaf shape, would be the hardest to measure directly. However, evergreen forests in the Pacific Northwest and Southeast can be clearly discriminated by

"duration of greenness" and "onset of greenness." [Loveland, et al. 1991] Additionally, known spectral characteristics of stems and leaves have been proposed for weed detection. [Wang, et al. 2001, Okamoto, et al. 2007] Similar characteristics could be used for autonomous fuel classification or even species identification for more detailed fuel mapping using very high special resolution hyperspectral aerial photography.

Scott et al. [2002] was one of the first studies into the feasibility of creating a fuel map from aerial imagery. This paper compared U.S. Forestry Service aerial photos of the Santa Fe Watershed area in the Sangre de Cristo Mountains of northern New Mexico. Sixty 105' x 105' plots were harvested, dried, and weighed to determine the fuel loads in the area. The purpose of the study was to determine if there was a correlation with the crown density of Mixed Conifer, Ponderosa Pine, and Pinyon-Juniper trees and the amount of fuel available to burn. The study used color photos and a visual density guide to estimate the percentage of ground covered by the tree crowns and compared that to the measured dry fuel load within the plot. Linear relationship showed that Mixed Conifer and Ponderosa Pine had a strong linear relationship (P-values of 0.0135 and 0.0185, respectively), and Pinyon-Juniper did not (P-value of 0.5614). Extrapolating the empirical equations to another region, near Los Alamos National Lab in the Jemez Mountains also in northern New Mexico, yielded poor results. Therefore, these correlations are obviously site specific, and likely time-of-year specific.

Dennison et al [2005] compared the use of NDIV, which quantifies the reflectance characteristics of vegetation, with the Normalized Difference Water Index (NDWI), which was designed around the absorption characteristics of water, to determine the live fuel moisture (LMF) of a California shrubland. They found that replacing the visible light used in NDVI (red, in their example) with shortwave infrared (SWIR) gave a significantly better correlation with moisture content recently measured through destructive harvesting and oven drying. The paper used imagery from the MODIS multispectral satellite, so large resolution (500 meters per pixel) adds some uncertainty to

the measurements. The paper only evaluated five species of California chaparral, so a broader evaluation is still necessary. The authors believed that grasses, which have much lower moisture content, would not respond as well to NDWI as they do to NDVI. However, the asymptotic quality of NDVI at high values is not as prominent when using NDWI to measure moisture content.

Roberts, et al. [2006] also evaluated the usefulness of multispectral satellite imagery in determining LFM. LFM is a critical factor for determining fire danger in shrubland and catastrophic forest fires, where live crown fuels contribute to fire spread. It is defined as:

$$LFM = \frac{W_{wet} - W_{dry}}{W_{dry}} * 100\%$$

where W_{wet} is the harvested fuel weight before oven drying and W_{dry} is its weight after oven dying. In this study, imagery from MODIS and AVIRIS satellites collected from 1994 to 2001 were compared against each other and against samples taken by the Los Angeles County Fire Department (LACFD) during that time. They found strong linear relationships for predicting LFM with four greenness indices (NDVI, EVI, VIg, and VARI) and three moisture indices (WI, NDWI, and NDII) for LMC above 60%, with stronger correlations when plants were categorized by functional group. As the reflectance index fell below the level for 60% LMC the LMC remained constant. This phenomenon is likely a result of the LACFD's harvesting procedures, which excluded dead material which would build up under low moisture conditions and would affect the spectral reflectance of a plot.

INDEX	FORMULA	REFERENCE
NDVI	$\frac{\rho 857 - \rho 645}{\rho 857 + \rho 645}$	*Rouse et al. [1973]*
EVI	$2.5 * \frac{\rho 857 - \rho 645}{\rho 857 + (6 * \rho 645) - (7.5 * \rho 469) + 1}$	*Huete et al. [2002]*
VIg	$\frac{\rho 555 - \rho 645}{\rho 555 + \rho 645}$	*Gitelson et al. [2002]*
VARI	$\frac{\rho 555 - \rho 645}{\rho 555 + \rho 645 - \rho 469}$	*Gitelson et al. [2002]*
NDII6	$\frac{\rho 857 - \rho 1640}{\rho 857 + \rho 1640}$	*Hunt and Rock [1989]*
NDII7	$\frac{\rho 857 - \rho 2130}{\rho 857 + \rho 2130}$	*Hunt and Rock [1989]*
WI	$\frac{\rho 900}{\rho 970}$	*Penuelas et al. [1997]*
NDWI	$\frac{\rho 857 - \rho 1240}{\rho 857 + \rho 1240}$	*Gao [1996]*

Table 1 - Spectral index formulas defined by available MODIS channels, reproduced from Roberts et al. [2006]

According to Roberts et al. [2006], four main factors control LFM: leaf-level LFM, the age distribution of foliage, stem LFM, and the balance between stems and leaves. Satellite imagery can determine the large-scale reflectance of plots, which is largely driven by leaf reflectance in shrublands and forests. Of the greenness indices, the paper found that best predictors of LFM in a shrubland plot were VIg and VARI, both of which outperformed NDVI in in either MODIS or AVIRIS imagery. Of the moisture indices, WI and NDWI slightly outperformed the NDII indices. The paper also found that the moisture indices could be decreased by an increase in dead foliage as much as by a decrease in leaf-level moisture. Higher spatial resolution imagery which could identify individual plants as well as bare soil, roads, etc. may be able to improve some of these estimates. Additionally, VARI and VIg have been shown to have an almost linear relationship with vegetation cover, which may be useful for giving plant identifying algorithms a

starting point for determining the apparent footprint of live vegetation from high resolution imagery.

Poulos [2009] found that fuel distribution patterns for prioritizing fuel reduction treatments (i.e. prescribed burning) are influenced primarily by spectral characteristics, topographic position, soil moisture, and solar radiation. He used classification trees to identify four distinct fuel types in forested plots in Big Bend National Park in Texas, USA and Maderas del Carmen Protected Area in Coahuila, Mexico. Spectral information was taken from LANDSAT imagery, and topographic and solar radiation features were derived from a 30 meter Digital Elevation Model (DEM) from the US Geological Survey. The model was able to correctly classify plots one of into the four broad fire risk categories with over 80% accuracy, with the highest number of incorrect classifications occurring in grass and shrub plots. The paper concludes that these two vegetative groups have similar spectral qualities, but their burning characteristics are very different. Grasses are associated with low-intensity, high spread rate surface fires, whereas shrubs burn in more intense fires with slower spread rates. Despite this tendency, the results show that a model which integrates spectral measurements, local topography, soil condition, and solar radiation could be very useful for autonomously identifying fuel types for wide spread use in pre-fire risk analysis and mitigation.

Riggan, et al, [2010] observed that useful fire prediction would require accurate estimates of biomass accumulation, which in the case of southern California chaparral brush could be determined by a combination of historical tracking of the environmental conditions and remote sensing measurements of the spectral properties of the stand. In fact, the paper theorizes that the fuel state within a chaparral stand may be directly related to the reflective properties of the vegetation alone. The results of the analysis show a power-function relationship between NDVI and fine live biomass measurements when both are averaged across several stands of approximately the same age. Unfortunately, the low spatial resolution of the Landsat imagery

was too large to allow a detailed analysis of the effects of species composition within a stand, and extrapolation gave poor results in high-elevation stands and frequently burned stands.

Schmidt [2014] found that measuring chaparral ground cover by species gave a reasonable estimate for fuel loading. The test utilized aerial imagery of three stands, each with a different age since the last wildfire. Low altitude aerial imagery using ultra-high resolution cameras (spatial resolution less than 10 cm) was sufficient for a trained observer to identify plant species. When compared to the very labor-intensive process of destructive harvesting, aerial photography is an efficient means of surveying a large area on the ground. Plotting the observed ground cover of individual species against the measured fuel loading, the paper found that the data matched well to a linear fit. In fact, using a Leave One Out (LOO) regression scheme, the paper showed that the shrubs could be classified into broader functional groups rather than individual species and still follow a linear fit. LOO is often used in small sample sizes, where the training set is made of all data points but one, and the fit is tested against the one left out. This process is repeated for all data points, so that each one's fit is calculated as part of the validation. The paper even found that considering ground cover of all shrubs together - regardless of species - gave an even better fit for the two older stands. The technique tended to underestimate large plots and overestimate small plots. However, this phenomenon is within the error band of the data, and it could just be a coincidence given the small sample size.

Volumetric characteristics can play an important role in the prediction of wildfire behavior, especially catastrophic forest fires. Many of these characteristics can be estimated through active sensing such as LiDAR [Erdody and Moskal, 2010], and recent advances in photogrammetry could provide certain volumetric fuel characteristics from passive optical sensors. Fonstad, et al. [2013], constructed a bare-earth model using a low-altitude UAS platform equipped with a 10 megapixel Canon A480 compact digital camera. The system was able to produce point clouds with vertical and horizontal precision in the centimeter range. The paper compared the DEM

developed from of a LiDAR scan of Pedernales Falls State Park in Texas, USA in 2006 to the results of a Structure from Motion (SfM) analysis of photos taken from helikite blimp UAS flying between 10 and 70 meters above the ground. The accuracy of the two techniques, when compared to GPS ground surveys, were comparable, and the point density of the SfM point cloud was over thirty times as dense as the LiDAR acquisition.

SfM has some advantages over traditional photogrammetry. SfM algorithms do not require calibrated cameras like the ones used by NASA's Altair, even though most modern digital cameras usually have a focal length estimate encoded in the image tags. This feature would make the SfM calculations more efficient for programs that are optimized for it. [Snavely, 2008]

Like other photogrammetry techniques, if the images are geotagged with the camera's GPS coordinates or if ground reference points are added for landmarks then the georeferenced point cloud can be integrated into a Geographic Information System, or GIS. [Fonstad, et al., 2013] Mathews, et al., [2013] showed that SfM could determine volumetric characteristics of vineyards, where the ground points and the vegetation points are readily separable for creating a differential DEM, using a very simple unpowered UAS combination.

An industry presentation of the AirGon AV900 system [AirGon, 2015] showed that current systems are able to create dense point clouds in remote areas with 1-2 cm pixel size. The system uses a DJI S900 folding hexcopter frame equipped with a Sony NEX-5 camera and a gimbal mount to maintain a nadir orientation. This Vertical Takeoff and Landing (VTOL) system was designed for use in open-pit mines, where short landing areas and the risk of overflying populated areas would make a fixed-wing platform impractical. The system inputs images into Agisoft PhotoScan to produce a point cloud, and then uses LP360 to produce a volumetric analysis of specific areas (piles of gravel, in the mine example) by subtracting the base from the hull, or the above ground features. Like in Fondstat, et al. [2013], AirGon found that calibrating the camera

before the flight did not improve the accuracy, since SfM programming self-calibrates the images as it determines camera locations and orientations. The manufacturers admit that the exact accuracy of systems like this is unknown, and data should be interpreted conservatively until the accuracy in diverse environments is better understood. The entire system, including hardware, software, training, and support is just under $30,000, which is not much higher than estimates of a volunteer fire department's expected budget and well within the budget of a large fire department for acquiring a wildfire UAS. [Kurtley, 2014, Bradley, 2014]

CHAPTER III

METHODOLOGY

1. NEW TOOLS

The goal of this project is to research the capabilities of low-cost specialty UAS to identify ground fires and assess wildfire risk. The purpose of these experiments was threefold. First, the project would expand on previous wildfire UAS research by testing the effectiveness of small, relatively cheap commercial-off-the-shelf (COTS) sensors carried by a low-altitude airborne platform. Second, it would evaluate the minimum crew requirements to operate and monitor a small wildfire UAS at actual wildfire events. Third, it would research the firefighting impact of a wildfire UAS which was cheap enough that a rural fire department could afford to acquire and operate one.

Images were acquired from controlled burn experiments performed by the Oklahoma State University Fire Ecology department in the vicinity of the Marena Mesonet station and Lake Carl Blackwell in Stillwater. These tests demonstrated the operational and performance differences in platform and operating modes and imagery from various multi-spectral bands. Fixed wing platforms demonstrated a dramatic increase in range and endurance (roughly twelve times the range and four times the endurance with a similar payload) at the expense of an additional crew

chief responsible for hand launching the aircraft. Small COTS sensors could provide a much higher spatial resolution at low altitudes than more expensive sensors at very high altitudes. This tradeoff makes the platform more comparable to handheld sensors carried on board low-altitude helicopters used for mop up operations. A UAS will likely never achieve the situational awareness and flexibility that a dedicated helicopter will provide, however the operating cost of a single helicopter is orders of magnitude higher than a small UAS. The potential of nearly continuous coverage of a large area by a team of semi-autonomous UAS could give incident commanders more consistent situational awareness of hot spots after a fire. Additionally, a single UAS could give the incident commander at a small burn the same situational awareness available very large burns at a cost that is attainable to small volunteer fire departments.

Some flight tests were performed to test the usefulness of a 2-axis gimbal mount to reduce ego-motion of an airborne camera platform. An aluminum gimbal frame with two brushless motors was originally used to mount the camera, and several gimbal controllers were tested for compatibility. The first controller tested was a Basecam AlexMos 2-axis controller that came installed on the gimbal mount. The board was an outdated version, and it no longer supported the firmware that was available from the AlexMos. The second controller was a Quantum Micro AlexMos SimpleBGC, and it was damaged the first time a battery was attached to it. It was returned to the manufacturer as a defect. The third controller was a newer version of the BASECAM AlexMos 2-axis controller. It was able to maintain a more stable position for period of time, but any abrupt movement of the camera by approximately 20^{o} or more caused the gimbal to reference a new attitude as level. The white airframe visible at the top of the image shows the attitude of the aircraft, which is constantly changing to maintain a GPS position in the gusty winds. Any useful footage from this gimbal mount used the third gimbal controller.

After the third gimbal controller, a plug-and-play XAircraft STELL 2-axis gimbal was acquired for the project. This mount was designed specifically for the GoPro Hero3, and it is considered

the top-of-the-line COTS 2-axis gimbal for small UAS. This gimbal tested well in lab trials, but a damaged vibration absorber prevented it from being used in flight tests. Unfortunately, the gimbal's electronics were damaged in a lab test before more vibration absorbers could be purchased, and it was returned to the factory for repairs.

Figure 5 – DJI Phantom with GoPro camera

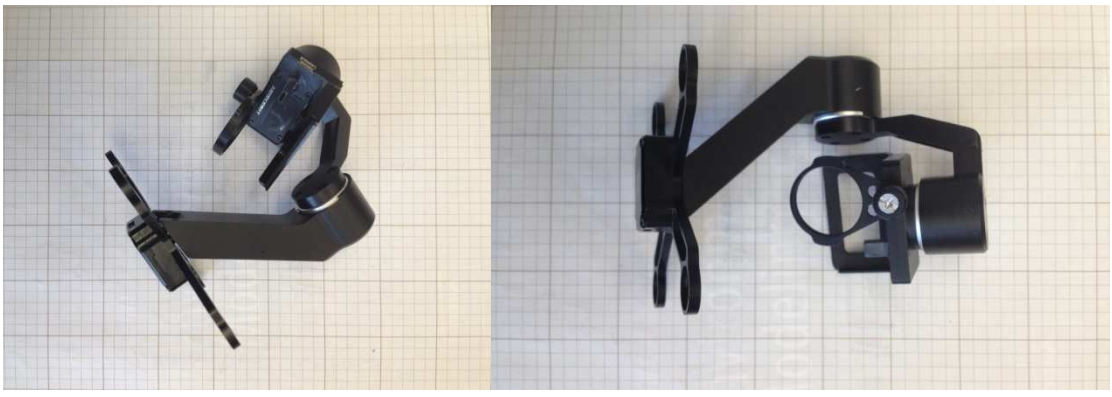

Figure 6 - XAircraft STELLA gimbal

2. EXPERIMENTAL SETUP

For the quadcopter tests, images were gathered by mounting a camera to the copter and recording for the entire flight, from just before takeoff to just after landing. There was no communication between the camera and the ground. All information was logged on an SD card in the camera. The pilot was not able to see a live feed of the video while flying, so he had to estimate whether the test object (smoke, fire, field, etc.) was in the camera's field of view or not. Similarly, exact altitudes are unknown other than a preprogrammed ceiling of 100 meters AGL based on GPS information, which was required to maintain compliance with the FAA mandated ceiling of 400 feet AGL without a Certificate of Authorization (COA) prior to changes in the FAA regulations [FAA Modernization and Reform Act of 2012]. All test flights were below 400 feet Above Ground Level (AGL) altitude and within visual line of sight of the operator and an observer. The differences in recording video and still images at intervals throughout the flight were also tested.

Some of the first flights were performed to test the viability of using raw GoPro video to detect fire or smoke. Videos were taken at a stabilized hover in order to capture clouds, buildings, roads, and other features that may confuse a smoke or fire detection algorithm. Stabilized slow hovering turns were also tested. Interviews with fire chiefs and trainers showed that one of the most difficult problems firefighters may have in interpreting color video data is maintaining awareness of the aircraft's position. These slow hovering turns would demonstrate a "400 foot periscope," which could perform a GPS position stabilized hover over the operator's position. This method of semi-autonomous flight and manual smoke and fire detection, when used with an On Screen Display which could give the aircraft's compass heading, would likely be the least sophisticated tool an incident commander would find useful for tactical firefighting.

An aircraft fixed down-facing GoPro camera was used in several flights lawn to identify the potential for stitching a photomosaic map of the area and using it for navigation and orientation through template matching algorithms. This technique was identified as an alternative to GPS navigation for the NASA UAS Airspace Avoidance Challenge. Tests were initially performed to evaluate the effectiveness of communicating the features on the ground to firefighters using a photomosaic. These tests were ended when it became evident that the extreme fish-eye distortion of the GoPro camera would produce nonlinear errors that require significant post-processing before image stitching could be applied.

Most of the data was acquired at the Oklahoma State University Fire Ecology test plots, located 13 km west of Stillwater, Oklahoma, USA. They are located 400 meters east of the "Marena" Mesonet site, which is the source of all relevant meteorological data. The site is relatively flat, with a 1 to 5% slope. The vegetation within each plot is a combination of tallgrasses, other grasses, forbs, legumes, sericea lespedeza (*Lespedeza cuneate*), woody plants, and litter. The site is organized into 14 plots, 20 meters by 30 meters each, with mowed paths between the plots.

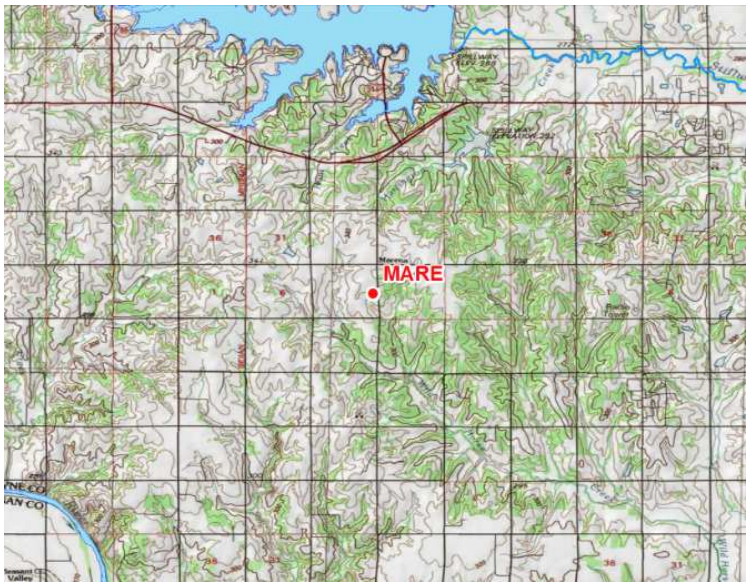

Figure 7 – Location of the Marena Mesonet station, west of Stillwater.

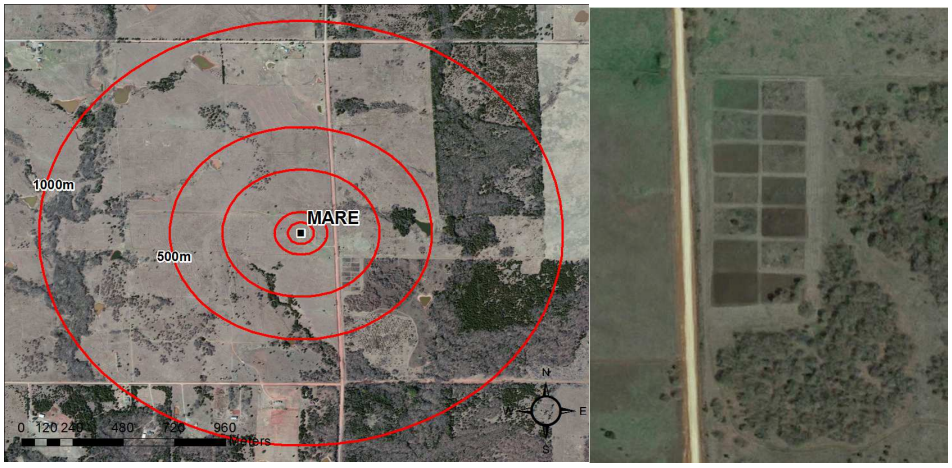

Figure 5 - The test plots are located approximately 400 meters from the Marena Mesonet station, west of Stillwater.

The primary purpose of the first test flights over a controlled burn was to gain aerial footage of smoke plumes during various stages of a fire using a hovering and slowly moving platform. The secondary purpose was to give the pilot practice flying near a fire and to develop a methodology for future flights at controlled burns. The Phantom was hand flown in the stabilized mode with a GoPro fixed under the aircraft. Most of the flight time this day devoted to gathering footage of the smoke plume from a hover. During one flight the aircraft was flown away from the fire and then back to it. Some issues were identified with aiming a camera while maintaining visual contact with the aircraft in the presence of smoke.

A second set of flights utilized the custom built aircraft fixed mount built for the modified Canon SX260 HS camera. This camera was pointed down in relation to the aircraft, but since it was fixed to the aircraft rather than gimbaled to maintain a strict nadir orientation this configuration will be referred to as "down facing." The aircraft was flown back and forth over the long axis of the plots and then over the short axis, simulating a search pattern that would cover the entire plot area. The camera took 1080p video of the entire flight. This caused two problems: each flight

used about 2 GB of storage space on the camera, and the constant motion of the aircraft relative to the ground caused the autofocus to lag the motion and caused most of the frames to be blurry.

The aircraft was flown at a controlled grass fire approximately half a mile west of the test plots. The CHDK was used to take still photos at two second intervals; however the program failed shortly after each takeoff. As a result, no useful footage was taken at this flight. Additionally, the thicker smoke made the aircraft harder to see, and so the return-to-launch failsafe had to be used. Designed for a loss of radio line-of-sight, the failsafe returns the Phantom to the GPS coordinate where it was turned on if the transmitter-controller is powered off. A subsequent flight at the test plots also failed to take more than a few still images before encountering the failure, and no useful images were collected from the flight.

The aircraft was flown at another controlled burn approximately 2 miles east of the test plots. The area had both crown fuels (trees) and surface fuels. This time a laptop computer was used to evaluate the footage and clear the memory card between flights. Because of this added step, the error that was causing the failure was discovered. Video was taken over wooded areas to evaluate the camera's ability to distinguish between surface and crown fuels, and the aircraft hovered over a burning area for three minutes to attempt to determine the spread rate. Unfortunately, the low ground clearance of the camera allowed dirt to get on the camera lens and shutter during one of the takeoffs or landings, so very little of the footage was useful for image processing. A subsequent flight was made at the test plots to gather video for SfM analysis of the plots.

Additional data was acquired The first flight was performed at a beginning of a small prescribed grass fire approximately two miles East of the test plots. The second was performed near the end of that burn, in order to test the capability of NIR imagery to locate hot spots on the ground during mop-up operations. The third was performed at the test plots in order to compare the SfM

and NDVI results with the previous two flights. All flights captured geotagged still images at two second intervals.

Additional flights were conducted at a 200 acre controlled grass burn on the northwest corner of Lake Carl Blackwell, 10 miles west of Stillwater, OK USA. The Phantom was flown to the edge of its visible line of sight range and back during these flights, and the controllable range in the presence of smoke was determined to be approximately 500 meters along the ground. Another two flights were made at the test plots to evaluate the difference between two flights on the same day under the same conditions using the same controls. Both flights were made in a back and forth search pattern across the long axis of the plots. The second flight took off approximately two minutes after the first flight landed, and no changes in illumination were observed between the flights. All of these flights utilized two second interval still photos. No video was taken of any flights.

For certain flights, hourly weather data for the Marena Mesonet station and OKFIRE satellite greenness maps for the state of Oklahoma were noted before, during, and after all the flights of that day. This included between two and four hourly weather and fire danger observations and the two weekly satellite maps: Relative Greenness and Visual Greenness.

3. PLATFORMS

The DJI Phantom quadcopter was the most used aircraft in this study. At its empty weight, the Phantom has an endurance of about 10 minutes with a 2.2 amp-hour battery. When loaded with a fixed camera this endurance is reduced to about 8 minutes, and with a camera and gimbal the endurance is about 5 minutes. This flight time is sufficient for gathering information, but a production system would need significantly longer endurance to be effective. The aircraft also lacks the payload capacity for onboard computations or reliable data communication with the ground. Because of these shortcomings, all data was post-processed in the lab after the flights.

The DJI S-900 folding-arm hexcopter was also built for this study. This aircraft has significantly greater payload capacity than the Phantom, and it has greater ground clearance to protect the sensors mounted under the main body. It is capable of carrying both a digital camera for SfM analysis, as well as a small LiDAR device to confirm the accuracy of SfM calculations. The aircraft was flight tested and shown to be uncontrollable, and redesign was not completed in time to integrate the aircraft into this study. For more information on the flight testing, refer to Section 5 Ground Control, below.

4. SENSORS

For color video used for smoke detection, a GoPro Hero was fixed to the aircraft, facing forward. The GoPro is capable of taking 1080p video at 30 frames per second or 12 megapixel still images at regular intervals (usually once per second). The fixed mount provided a wide field of view for surveying a large area in front of an aircraft at a high hover. Unfortunately, controlling an out-of-

ground effect hover requires significant motion in pitch and roll. These rotations make the video and images completely unusable for motion detection calculations, so an XAircraft STELLA 2-axis gimbal was also used to stabilize the camera in pitch and roll for optical flow and background subtraction algorithms. Unfortunately, the gimbal was damaged before any stabilized video could be taken in flight.

A modified Canon SX260 HS was used for fuel mapping and hot spot detection. Event38 modified this camera by replacing its red channel with near infrared (690 – 770 nm). As stated previously, near infrared reflectance is an indicator of plant health (chlorophyll) and can be combined with a color channel to calculate NDVI, an indicator of moisture content in grasses. Because this camera does not measure red, blue has been used instead as the visible color channel for NDVI calculation. This alternate definition of NDVI will be referred to bNDVI. The field of view was measured by analyzing the following picture taken from 12 inches. The heavy dashed lines represent 1 inch grid squares.

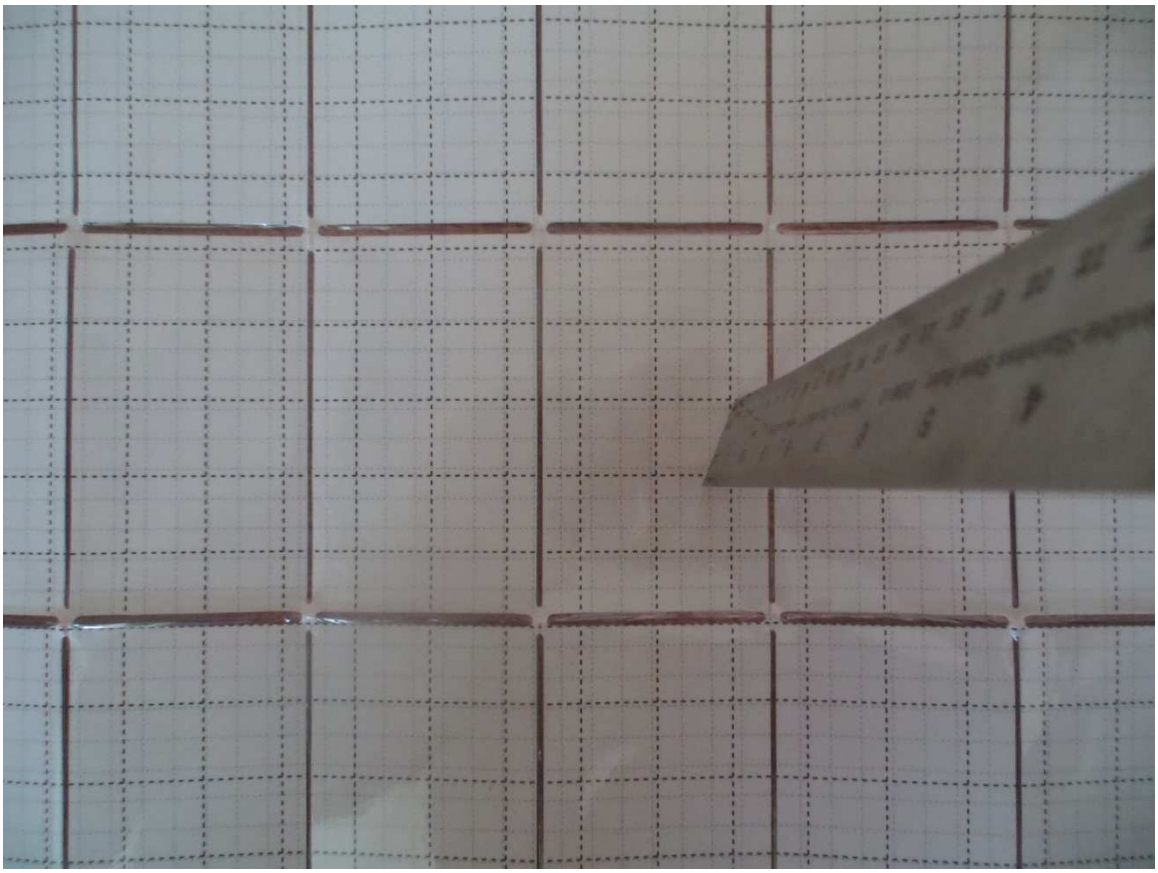

Figure 6 - A grid sheet held 12 inches from the camera lens. The heavy dotted lines represent 1 inch squares.

The picture shows that the image is 15 inches (64°) wide and 11.25 inches (50°) tall. Since the picture resolution is 4000 x 3000, the pixel size is approximately 3.75 x 10^{-3} inches squared, which at 12 inches is approximately 0.018° (0.3 milliradians) square in the center, using the following formula.

$$field\ of\ view = \tan^{-1}\left(\frac{l}{r}\right)$$

Where l is the length along the focal plane, and r is the distance to the focal plane, or 12 inches in this example. The camera also takes 23 frames per second (FPS) video at 1080p (1920 x 1080, 8 bit, 3 channel) resolution. Though the aspect ratio is different, assuming a similar coverage of (15" x 11.25" = 168.75 in^2) gives a pixel coverage of 8.1 x 10^{-5} in^2, or 9 x 10^{-3} inches square. Using the equation above, this gives an angular resolution of 0.043° (0.75 milliradians) square in

the center. This resolution is still significantly higher than the AMS-Wildfire multispectral sensor used by the NASA Ikhana, and the total field of view is comparable to the AMS-Wildfire.

The Canon camera can operate in two distinct modes: video or still images taken at a set interval. The camera was not designed to automatically take pictures at intervals, but the camera was loaded with the CHDK, which used a script called "Shot Interval" to take an image every two seconds for up to 300 images (approximately 10 minutes). In addition to giving a much higher resolution image and automating the step of frame grabbing, this process gave two distinct advantages over video that needed to be tested.

First, unlike video, which can only geotag the first frame of a movie, each image can be geotagged with the precise GPS latitude, longitude, and altitude at the time the picture was taken. Without precise Euler angles of the camera orientation this information would be insufficient for traditional photogrammetry, but using SfM this information should simplify the very computationally complex step of locating the cameras. It may also eliminate the need for ground reference points since the center of every image can be used as a ground reference point with the same latitude and longitude as the image.

Second, ego-motion of the camera in flight causes the automatic focus for lag behind the actual distance to the target, causing an intermittent blurriness in the video. When taking sample frames, these blurry images must be removed manually in order to get a useful solution from SfM. With still images the autofocus has some time to ensure the target is in focus before taking the picture. In order to test this theory, the blurriest images were not removed from the bank of still images. Only images before takeoff and after landing were removed, because in that condition the camera is very close to the ground and so navigational information can be derived from those images.

The camera was loaded with the CHDK on an 8 GB SD card. This software kit allowed the camera to be programmed to automatically take pictures at a regular interval (every 2 seconds in this study). This approach was a huge improvement over 1080p video. It provided six times the resolution and a sharper focus while reducing the memory requirements. Unfortunately, vibrations from the DJI Phantom at high throttle settings were significant enough to induce an error in the camera's internal clock, disengaging the process shortly after takeoff in almost all flights. Video was sampled using Aoao Video to Picture Converter to collect two images per second of video, and blurry images were manually removed.

Figure 7 - Modified Canon SX260 HS camera with custom build aircraft mount.

Some Long Wave Infrared (LWIR) video was also evaluated for its use in spotting fire-related hotspots from a UAS. LWIR radiation is often used for determining temperature (thermal infrared) of surfaces that are close to room temperature. Technically, any temperature above absolute zero will emit radiation at all wavelengths according to Planck's law for spectral blackbody emissive power, $E_{b\lambda}$.

$$E_{b\lambda}(\lambda, T) = \frac{C_1}{\lambda^5[\exp(C_2/\lambda T) - 1]} \quad (W/m^2 \cdot \mu m)$$

Where

$$C_1 = 3.74177 \times 10^8 \, W \cdot \frac{\mu m^4}{m^2}$$

$$C_2 = 1.43878 \times 10^4 \, \mu m \cdot K$$

T is temperature in Kelvin, and λ is wavelength in μm. Differentiating Planck's law with respect to λ while holding T constant and setting equal to zero gives Wein's displacement law for the wavelength for which the peak occurs for a specified temperature. [Çengel, 2007]

$$(\lambda T)_{\max power} = 2897.8 \, \mu m \cdot K$$

Therefore, a NIR camera which has a range of 0.72-1.00 μm (i.e. AHVRR imagery) will see peak emissive power from 2900-4025 K (4760-6785° F). On the other hand, a LWIR camera which captures a range of 8-14 μm (i.e. Lepton camera used in the FLIR ONE) [FLIR] would see peak emissive power from 207-362K (-87-192° F), which is a much more reasonable range for detecting fire.

A single-channel long-wave infrared (LWIR) camera (DRS Tamatisk320™) was mounted to a fixed wing aircraft (OSU's *Firebird*) and collected forward-and-down facing video in flight in both fire and non-fire environments. The camera used auto-scales the intensity for each frame, so that the intensity range falls between the brightest and dimmest pixels in the scene. This characteristic keeps bright pixels from saturating the intensity, but it prevents a direct measurement of brightness (or temperature) from the image intensity. Because of the auto-scaling function, the video was evaluated for qualitative characteristics only.

The evaluations of these systems will satisfy objective 5.

5. GROUND CONTROL

The DJI Phantom was hand-flown using the DJI model DJ6 transmitter-controller. The Phantom is automatically stabilized in four axes: heading hold using the magnetometer, and altitude, lateral position, and longitudinal position hold using the onboard accelerometers and GPS measurements. These modes assist in maintaining a stable hover, especially in gusty winds outside of ground effect (approximately 2 feet or higher AGL). The NAZA-m flight controller on the Phantom does not allow for flying preprogrammed routes. DJI publishes a ground control app for the iPhone, however this program is designed for DJI factory aircraft like the Phantom 2 Vision, not modified aircraft like the one used in this study, and so the app was not used to gather data for this study.

The DJI S-900 was also flight tested as part of its integration into this study. The transmitter-controller used was a commonly used fixed wing controller made by Futaba. The hexcopter used an Atlas flight controller, and was stabilized in four axes like the Phantom. It was uncontrollable during initial flight tests, and it was not ready in time for any of the information gathering flights. The Futaba controller is designed for fixed wing aircraft flying straight and level and level bank maneuvers, which is a very different profile than a level hover or very low speed maneuvers used throughout these tests. This difficulty comes from two fundamental differences in flying traditional fixed-wing aircraft and flying Vertical Takeoff and Landing aircraft.

The Futaba appeared to send continuous control signals to the aircraft, which in fixed wing aircraft is used to “trim” the aircraft for stable flight without any control inputs. Unlike fixed-wing aircraft, the hexcopter is an inherently unstable platform, and it is only stabilized by a complicated automatic control scheme, which results in the four controlled axis mentioned above. Any control input from the operator causes the hexcopter to simply re-reference the profile it is

trying to maintain. For instance, a continuous yaw input in a fixed-wing aircraft would deflect the rudder, which could be used to compensate for a sideslip condition. In a stabilized hexcopter it would induce a yaw rate by continuously re-referencing the heading angle.

Secondly, the Futaba's throttle, or thrust, control is designed with detents to hold one of several discrete positions during flight. In a fixed-wing aircraft, this is a desirable feature. Maintaining a constant speed is almost impossible without maintaining a constant throttle setting, since thrust is oriented forward and is the most responsive airspeed control. In rotary-wing aircraft thrust is oriented upward, so that in a hover altitude is maintained by constantly changing the throttle setting to adjust for updrafts, downdrafts, and side gusts (since any lateral, or transverse, airflow makes the propellers more efficient). In addition, takeoffs and landings are finesse maneuvers that cannot be performed well by the autopilot because of the risk of dynamic rollover. These maneuvers would require constant adjustment of all four control settings to pick up or land the aircraft smoothly without any lateral movement. In initial flight tests, the aircraft came off the ground abruptly and was also set down abruptly, causing the aircraft to rotate around the skid and invert on the ground. Damage to the aircraft was minimal, but further flight tests were postponed until a new transmitter-controller could be integrated into the system.

Based on the observations of the hexcopter test, a successful transmitter-controller for a rotary-wing aircraft must have three features. First, it must have the ability to completely zero-out the control inputs when the control force is removed. In other words, there must be no trim feature that could induce a yaw rate or lateral drift. The aircraft is trimmed automatically by the flight controller. Second, the gains must be small if the aircraft is going to be hand-flown during routine take-offs and landings. GPS and inertial systems are not precise enough to prevent dynamic rollover, especially in gusty wind conditions. Similarly, the pilot's control gains must be limited to reduce the potential for pilot-induce oscillations due to the large latency period inherent to remotely piloted aircraft. Third, the controls should include no detents except the

zero-input detent already mentioned. Detents eliminate the operator's ability to the make very small adjustments required while hovering. Also, they could induce a rate-of-change to the flight controller's settings, similar to the trim function mentioned above.

The use of a more complex ground control program, such as ArduPilot Mission Planner, is beyond the scope of this project. One goal of this study is to evaluate the usefulness of an aircraft that is deployed quickly by a single, minimally trained operator.

The flight testing of these platforms with operating sensors satisfies objective 6.

6. ALGORITHMS

Fire spotting algorithms were tested against one image of a blazing forest fire (a) for calibration and four aerial photos with no fire (b)-(e) for evaluation. Image (b) was taken by OSU's Firebird UAS at the OSU Unmanned Aerial Flight Station (UAFS) on a foggy morning. Image (c) was taken by an octocopter at the UAFS at sunset after a snow. Image (d) was taken by Firebird over a field near the UAFS, and it contains a small red "X" on the ground that was used to evaluate target detection capabilities. The "X" is in the left center of the image. Image (e) includes most of OSU's Stillwater Campus. It was taken at a high altitude from the East side of campus, and it includes several red brick buildings and snow on the ground, with overcast skies.

(a)  (b) 

(c)  (d) 

(e) 

Figure 8 - The test set of images (1 fire and 4 non-fire) used to evaluate smoke and fire image detection techniques.

Additional images were also added as needed to illustrate specific issues with each algorithm. The motion detection algorithms were tested using videos from online smoke databases (http://signal.ee.bilkent.edu.tr/VisiFire and http://cvr.kmu.ac.kr) to determine their effectiveness using stationary cameras. Successful algorithms were tested further using video gathered from GoPro color imagery captured by either a hovering copter or the *Firebird* fixed-wing UAS.

Some of the first tests performed were chrominance only tests for spotting wildfires in an aerial photo using RGB or some similar color space. A test image was broken down into histograms, with the non-fire and non-smoke pixels manually removed, to determine what RGB values were the most common in the fire pixels and least common in the non-fire pixels. These empirical value ranges were then applied to other images, with or without smoke and fire, to test the effectiveness of fixed chromatic thresholds. A similar test was performed for the HSV color spaces.

In accordance with Chen, et al. [2004], another chrominance test was conducted with thresholds that were relative to the other chrominance values, not absolute thresholds. In this test, a pixel was fire colored if all of the following were true:

$$R > R_t$$

$$R \geq G > B$$

$$S \geq (255 - R) * \frac{S_t}{R_t}$$

where R, G, and B are the Red, Green, and Blue pixel values, respectively, R_t is some fixed threshold for Red, S is the Saturation value, given as:

$$S = 1 - \frac{1}{R + G + B}[min(R, G, B)], \qquad 0 \leq S \leq 1$$

and S_t is the value of S when $R=R_t$.

Chen, et al. [2004] also includes a chrominance-only smoke test involved testing for the greyness, or the closeness of the R, G, and B values. The paper gives the following formula:

$$R \mp r = G \mp g = B \mp b$$

$$0 \leq r, g, b \leq a$$

where "a" is a fixed threshold for the minimum greyness of smoke. For calculation in MATLAB, the following equation was used instead:

$$max(R, G, B) - min(R, G, B) \leq a$$

Celik, et al. [2007] provided a three level flame test using chromatic values. First two steps used no fixed thresholds, and therefore they were used to test the effectiveness of relative thresholds. These two decision rules are written below:

$$R(u,v) > G(u,v) > B(u,v)$$

$$R(u,v) > R_{mean} = \frac{1}{k}\sum_{i=1}^{k} R(u_i, v_i)$$

After the greyness test proposed by Chen, et al. [2004], the second color smoke test evaluated was the dark channel test to confirm the assumptions of Ligang, et al [2014]. This technique was tested in MATLAB against images depicting various atmospheric conditions, such as clouds, fog, sunrise/sunset, and artificial lights. Still images were segregated into pixels that fall above or below a certain threshold of dark channel brightness, and video clips were tested by comparing a frame before the smoke plume was evident to various frames after the fire began to smoke. Because of the limited flight time of a small hovering UAS, each video was only tested for smoke plume identification in the first minute after the smoke starts.

Optical flow was also tested for its application to smoke detection. With a stationary camera, the upward movement of a smoke plume can sometimes make the smoke boundary evident within a few frames, since the background motion is small and often cyclic. With a moving camera, the camera's motion must first be estimated from the optical flow, and then the smoke plume can be identified by subtracting the optical flow due to camera motion from the optical flow of the entire frame. Since in-plane rotation (pitch and roll) would likely make this calculation impossible with current technology and computational techniques, only gimbal stabilized video was analyzed by this technique. A GoPro Hero3 was attached to a XAircraft STELLA gimbal and recorded video in the lab with the operator moving the gimbal mount in all tree directions and in pitch and roll relative to the camera orientation (the x-axis being perpendicular to the camera's focal plane). Because the GoPro produces video with an extreme fish-eye effect, the video was tested for symmetry of optical flow rather than uniform optical flow across every pixel in a single frame.

Dense optical flow calculation was calculated using the MATLAB code referenced in Sun, et al. (2010). The code can be downloaded freely at **http://cs.brown.edu/~black/code.html.**

Another Oklahoma State University UAS project had attempted to use optical flow in a down-facing camera for navigation. Due to the success of this technique, optical flow was also evaluated on down-facing NIR/G/B video originally collected for bNDVI and SfM analysis. The purpose of this test was to find discontinuities in the dense optical flow that would indicate a moving background, which could be a strong indicator of smoke. Discontinuities in the optical flow field could be determined by taking the Laplacian, as defined below. [Horn and Schunck, 1981]

$$\nabla^2(u,v) = \nabla \cdot \nabla(u,v) = \frac{\partial^2 u}{\partial x^2} + \frac{\partial^2 u}{\partial y^2} + \frac{\partial^2 v}{\partial x^2} + \frac{\partial^2 v}{\partial y^2}$$

CHAPTER IV

RESULTS

1. FIRE DETECTION

The first models tested were chrominance-only, fixed threshold, empirical flame color algorithms. The following pictures were broken into three histograms (Red, Blue, and Green channels) to analyze fire colors in RGB color space.

(a) 

(b) 

(c) 

Figure 9 (a) a wildfire image, (b) manually segmented fire and smoke only and (c) manually segmented fire only

The histograms from these three images are shown below, with the top row representing the red channel the entire image, fire and smoke only, and fire only respectively, the middle row representing the green channels of the same images, and the bottom row representing the blue channels of those images.

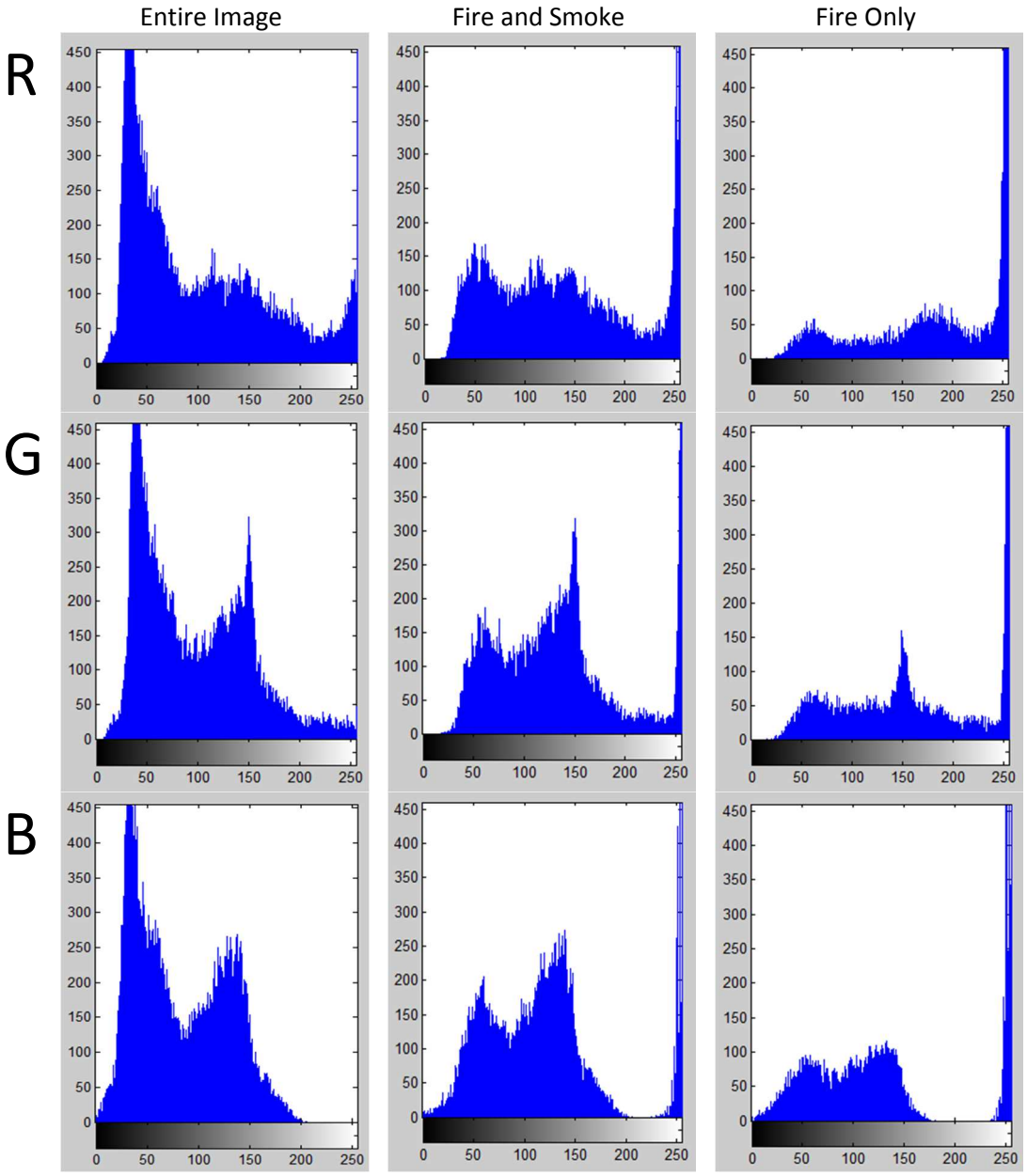

Figure 10 - Histograms of the Red, Green, and Blue channels of the full image and the manually segmented sub images.

The histograms showed that the most number of fire pixels and the least number of non-fire pixels met the following criteria:

$$R > 180, G > 100, B < 160, \qquad 0 \leq R, G, B \leq 255$$

These static thresholds were tested against the training image and the following non-fire images, with the following results. Fire alarms are indicated on the right.

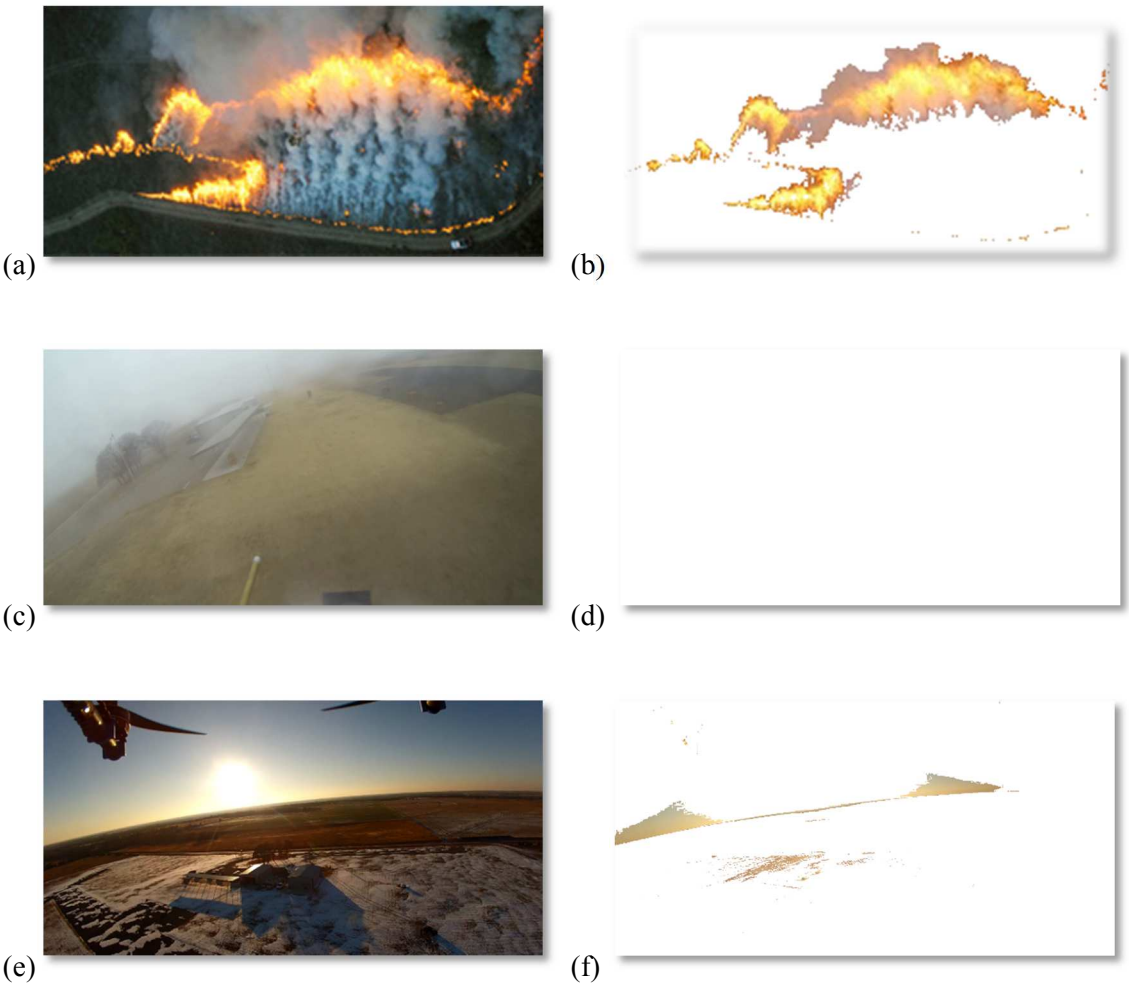

Figure 11 fixed RGB threshold results from the test images.

(g)  (h) 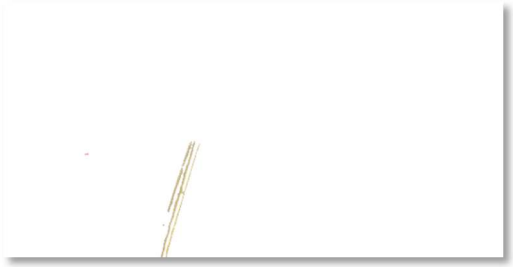

(i)  (j) 

Figure 14 (cont.) - fixed RGB threshold results from the test images.

From the images above, it appears that fixed RGB thresholds will produce excessive false positives when applied to images other than the one it was calibrated with. Variations in background, illumination, sky condition, humidity, etc. will cause a set of fixed RG thresholds to break. The same test was applied to the HSV color space. HSV stands for Hue, Saturation, and Value, and it was also tested because each channel represents different chromatic characteristics than RGB color. An evaluation of the HSV histograms of the fire image gave the following thresholds:

$$H < 50, S > 130, V > 200, \qquad 0 \leq H, S, V \leq 255$$

Further experimentation on the original image found that the following values gave the best results:

$$H < 50, \qquad S > 50, \qquad V > 50, \qquad 0 \leq H, S, V \leq 255$$

$$\boldsymbol{OR} \quad H < 0.2, \qquad S > 0.2, \qquad V > 0.2, \qquad 0 \leq H, S, V \leq 1.0$$

The second values represent the default scale given by the MATLAB function RGB2HSV. The 8-bit integer values were originally used because they were easier to develop into a histogram. The HSV static thresholds were tested against the training image and the following non-fire images, with the following results. Fire alarms are indicated on the right.

(a) 

(b) 

(c) 

(d) 

(e) 

(f) 

Figure 15 - fixed HSV thresholds results from the test images.

(g)  (h) 

(i)  (j) 

Figure 12 (cont.) - fixed HSV threshold results from the test images.

These tests illustrate the problem with defining static thresholds of chromatic characteristics alone to identify fire pixels. Snow, a rising or setting sun, red objects, and lights all have the potential to create false fire alarms.

In order to test the improvement from removing static thresholds, the previous images were also tested with the first two steps from Celik, et al. (2007), namely:

$$R(u,v) > G(u,v) > B(u,v)$$

$$R(u,v) > R_{mean} = \frac{1}{k}\sum_{i=1}^{k} R(u_i, v_i)$$

These relations are illustrated by the following breakdown of the Red, Green, and Blue channels of a wildfire image.

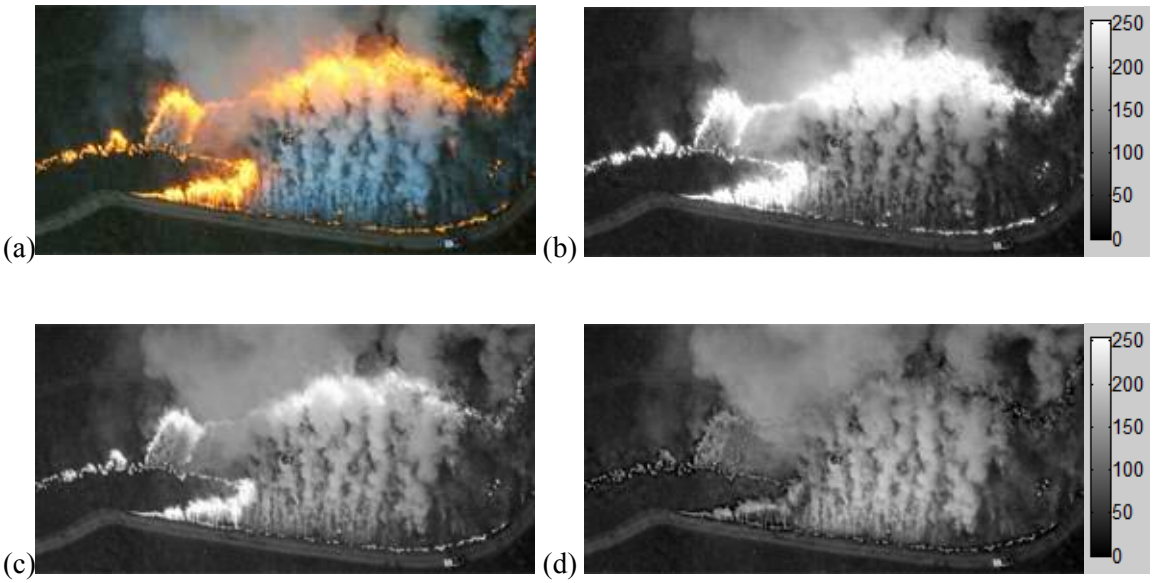

Figure 13 - (a) A wildfire image, (b) the Red channel only and scale, (c) the Green channel only, and (d) the Blue channel only and scale.

These relative thresholds were tested against the same set of images as the earlier tests, with the following results. Fire alarms are indicated on the right.

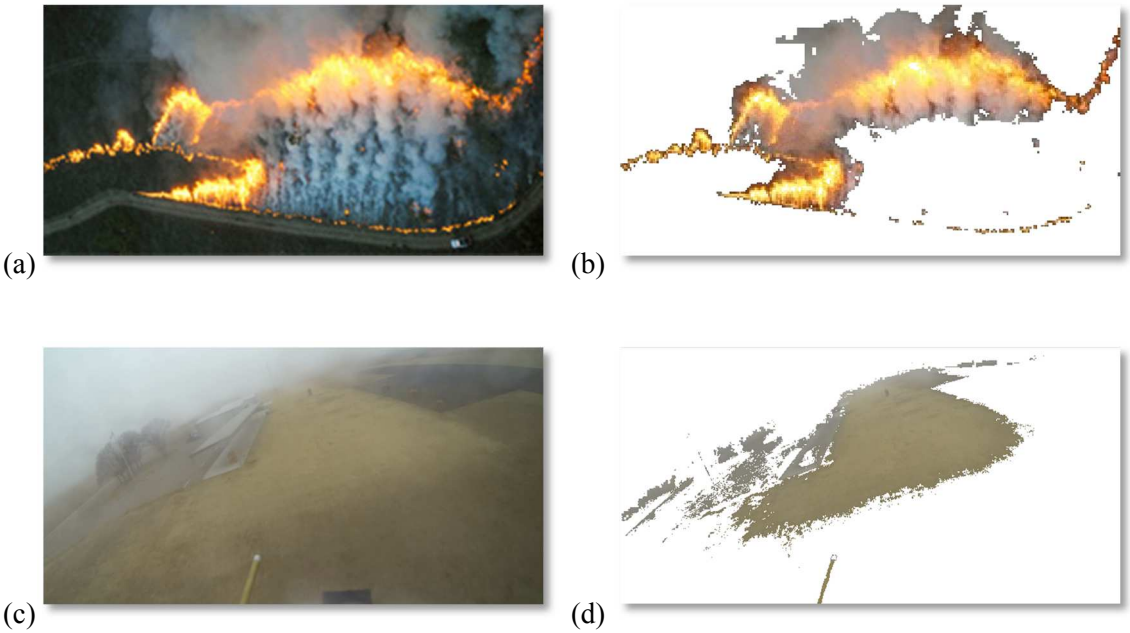

Figure 17 – Relative RGB threshold results from the test images.

(e)  (f) 

(g)  (h) 

(i)  (j) 

Figure 14 (cont.) - Relative RGB threshold results from the test images.

This increase in computational complexity results in an increase in the number of false alarms in the test images. Clearly, in the images tested, a transition from fixed thresholds to relative thresholds does not improve accuracy. The literature points to an improved performance from data from the infrared spectrum. The following images were taken over a controlled burn by a RGB camera that has been modified by replacing the Red filter replaced with an NIR filter, referred to as "color NIR." Vegetation viewed through this camera appears to be red, which is a result of the high NIR reflectance of vegetation.

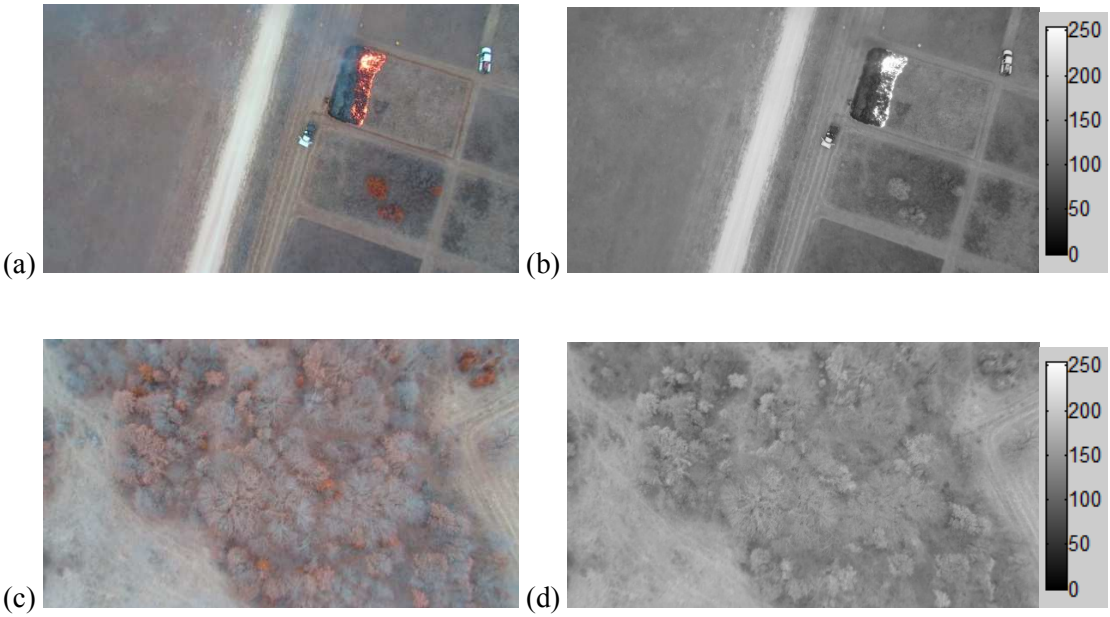

Figure 15 - (a) NGB image of a fire, (b) NIR greyscale of a fire, (c) NGB image of trees, and (d) NIR greyscale of trees.

In the non-fire image, the NIR values range from 69-196, while the road in the fire image has values as high as 230, and the white trucks and the fire each had several pixels that saturated the NIR channel at 255. Even in the non-fire image, almost all of the pixels above 160 were mowed pathways. Clearly, high NIR values are an indicator of non-natural features in these images, with fire emitting a stronger NIR signature than anything other than the white trucks in the image.

Another interesting feature of the NIR images is the lack of blurriness due to smoke in the fire image. Almost all of the blurring in the fire image comes from the Blue and Green channels. This agrees with Davenport's (2012) conclusion that almost none of the information useful for smoke plume identification came from the infrared bands when combined with color information. See the next section for a more detailed analysis of the use of NIR to identify smoke plumes.

Some Long Wave Infrared (LWIR) video collected from the OSU *Firebird* fixed wing UAS was also evaluated for this study. Surfaces close to room temperature emit their strongest radiation in the LWIR range, and therefore this type of sensor is often used to find hotspots on room temperature objects. The camera used was not calibrated for temperature sensing, and the

intensity auto-scales to prevent hot or cold spots in the frame from saturating the output. Therefore, the following images have been evaluated qualitatively for the merit of this type of sensor mounted to a UAS. The first two images show how well LWIR can locate animals (first image) or humans and urban structures like the OSU UAFS facility (second image).

(a) 

(b) 

Figure 16 - LWIR images of (a) cattle and (b) the OSU Unmanned Aerial Flight Station.

The next pair of images were taken one second apart. The first image shows the end of a right banking turn, where the aircraft has pitched up to maintain altitude in the turn. The second image is the aircraft recovering from the turn, levelling the wings and pitching back down to a cruise attitude. These images illustrate the total lack of information that comes from a LWIR camera looking at the horizon. The sky is so dark that horizon looks bleached out by comparison. If an LWIR camera points at the horizon, the only information it will get is the attitude of the horizon.

(a) 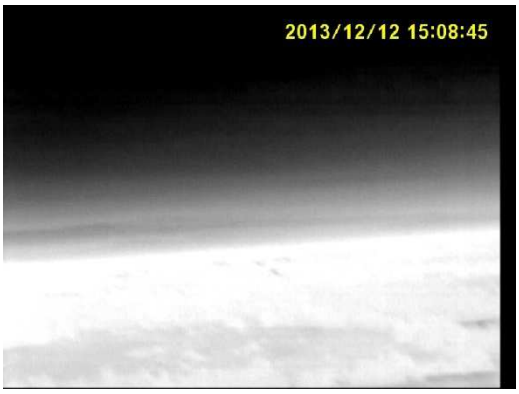

(b) 

Figure 17 - LWIR images of (a) the horizon during a banking turn and (b) the ground after recovery from the turn.

The next two images illustrate how a LWIR camera percieves water. Water and water vapor almost completely absorb all radiation in this band, so this type of camera will get virtually no information from the surface of water. These images also show a mild instance of the auto-scaling function, where the camera has reduced all the intensities due to bright objects in the scene, then has increased all the intensities as the dark pond begins to dominate the image. This feature would make direct measurements of surface temperature impossible, though relative temperatures may be measurable assuming there are no bodies of water or other anomolies present that could skew the results.

(a) 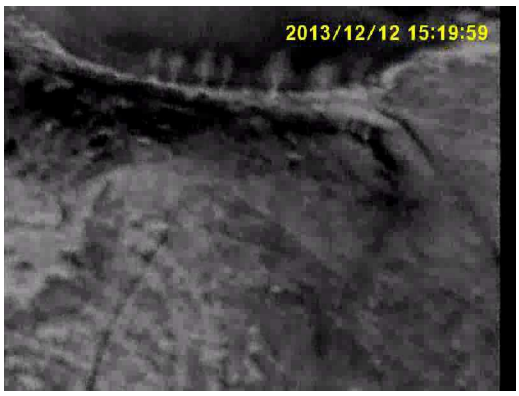

(b) 

Figure 18 - an example of auto-scaling intensity. (a) The lake is just coming into sight. (b) The lake is dominating the scene, increasing the intensity of everything else.

The remaining images were taken at a controlled burn on March 13, 2013. They clearly show the problems with the autoscaling function in the presence of fire. In the first image, the road is just coming into view at the top of the image. This road is being used as a backstop for the fire, and as the aircraft moves forward the fire comes into view one second later. The field behind the road, which previously was bright white, now has become black in relation to the very hot ground behind the fireline. Little imformation can be extracted from this second image, since the hot fire looks similar to a blurry field from a non-fire frame. The third image is about two minutes later, as the aircraft is finishing a pass over the fire from a different direction. The field in front of the bright fire line is dark and little information coud be extracted from it. A second later, as the fireline begins to pass out of view off the bottom of the image, the detail returns to the field in front of the fireline. This phenonomon of autoscaling could be dangerous if the LWIR camera is being used for locating both the fireline and humans or animals in the vicinity of the fire. It the target is too close to the fireline it will be bleached out by the bright fire and will not be detected. An effective tool would use a camera with a scale calibrated to find both warm targets (i.e. humans) and hot targets (i.e. fire) and maintain that calibrated scale throughout the flight. Color imagery can determine much more information about the surroundings, while LWIR information should be used primarily to determine temperature.

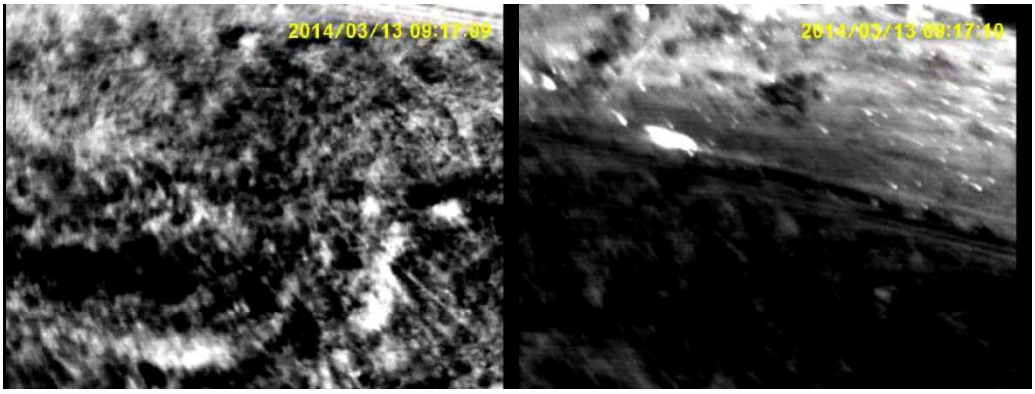

Figure 19- (a) Coming close to the fire line, the image is bright. (b) The fire line is in the image, and the brightness is reduced.

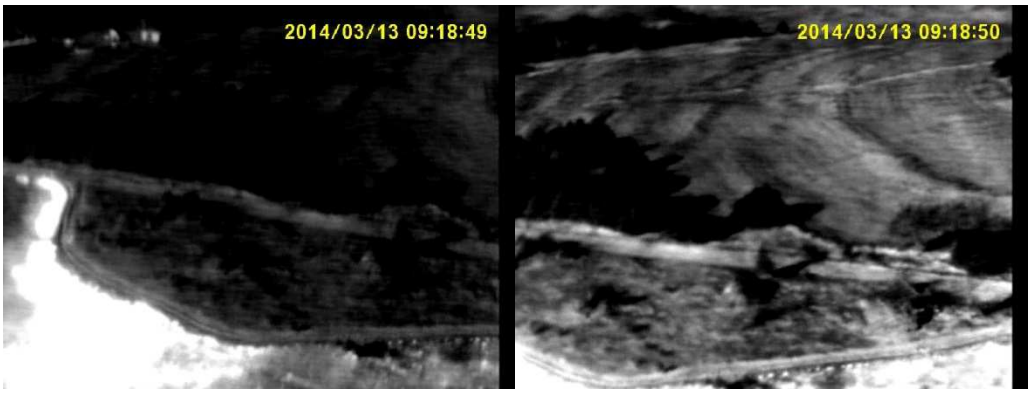

Figure 20 - (a) Passing the fire line, the image is dim. (b) Past the fire line, the image is bright.

2. SMOKE DETECTION

The first tests conducted on smoke were designed around analyzing a single frame. This approach could possibly negate the effects of the random motion of a camera attached to a small UAS. The simplest single frame tests are for color characteristics. The best examples of smoke color tests from the literature are greyness tests, or the closeness of the Red, Blue, and Green channels.

$$max(R, G, B) - min(R, G, B) \leq a$$

where R, G, and B are the Red, Green, and Blue pixel values, and "a" is an empirical threshold. This threshold can be fixed at some value (Ligang, et al [2014] recommends between 15 and 20) or varied so that only a certain number of pixels are identified. The following images illustrate one of the problems with a fixed threshold, in this case 20.

(a)  (b) 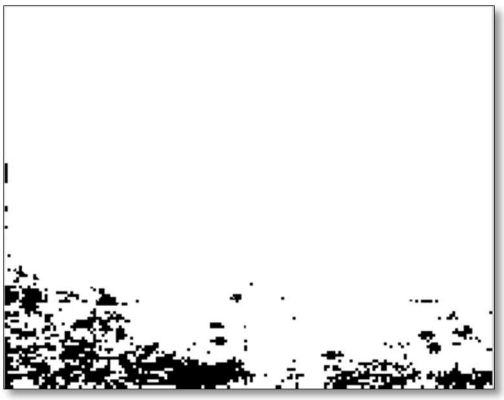

Figure 21- Example results for the assumption of gray smoke: (a) original frame, (b) pixels for which a = 20

Ligang, et al. [2014] claimed that smoke could be segmented by analyzing the dark channel of each candidate block. Non-smoke, non-sky blocks would have a zero value in at least one channel of one pixel in the block. Smoke, on the other hand, is gray in color and therefore all the channels in each pixel will have at least a small value. This study first tested that the dark channel is very small for non-smoke blocks and found that this foundational assumption, referred to as the "dark channel prior," could not be validated for various conditions. The figure below shows a frame from a video smoke sequence, and the smoke plume is just beginning to be visible. Each pixel in the image was evaluated, and the pixels with at least one channel ≤ 25 are shown as white. 25 was chosen because it is 10% of the full range of values (0-255). Clearly, there are very few reasonably sized blocks that would satisfy the criteria of a very small or zero dark channel. An increase in the dark channel due to the appearance of smoke is unlikely to be noticed in this video sequence.

(a)  (b) 

Figure 22 – Example results for the assumption of dark channel for smoke: (a) Background frame; (b) Pixels for which dark channel is 10% of the maximum RGB values (≤25).

For consistency, the dark channel prior assumption was tested against the test set of images. The images on the left are the original image, and the images on the right show the highest dark channel value in a 9 pixel wide and 7 pixel tall window around each pixel. Clearly, the dark channel prior assumption fails under even mundane conditions. The smoke blocks have a small dark channel value, but so do most of the non-smoke blocks. In some of the images every block has a non-zero value.

(a) 

(b) 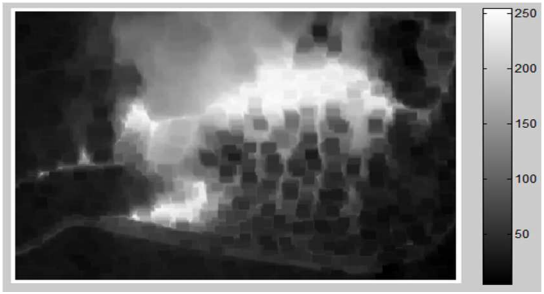

(c) 

(d) 

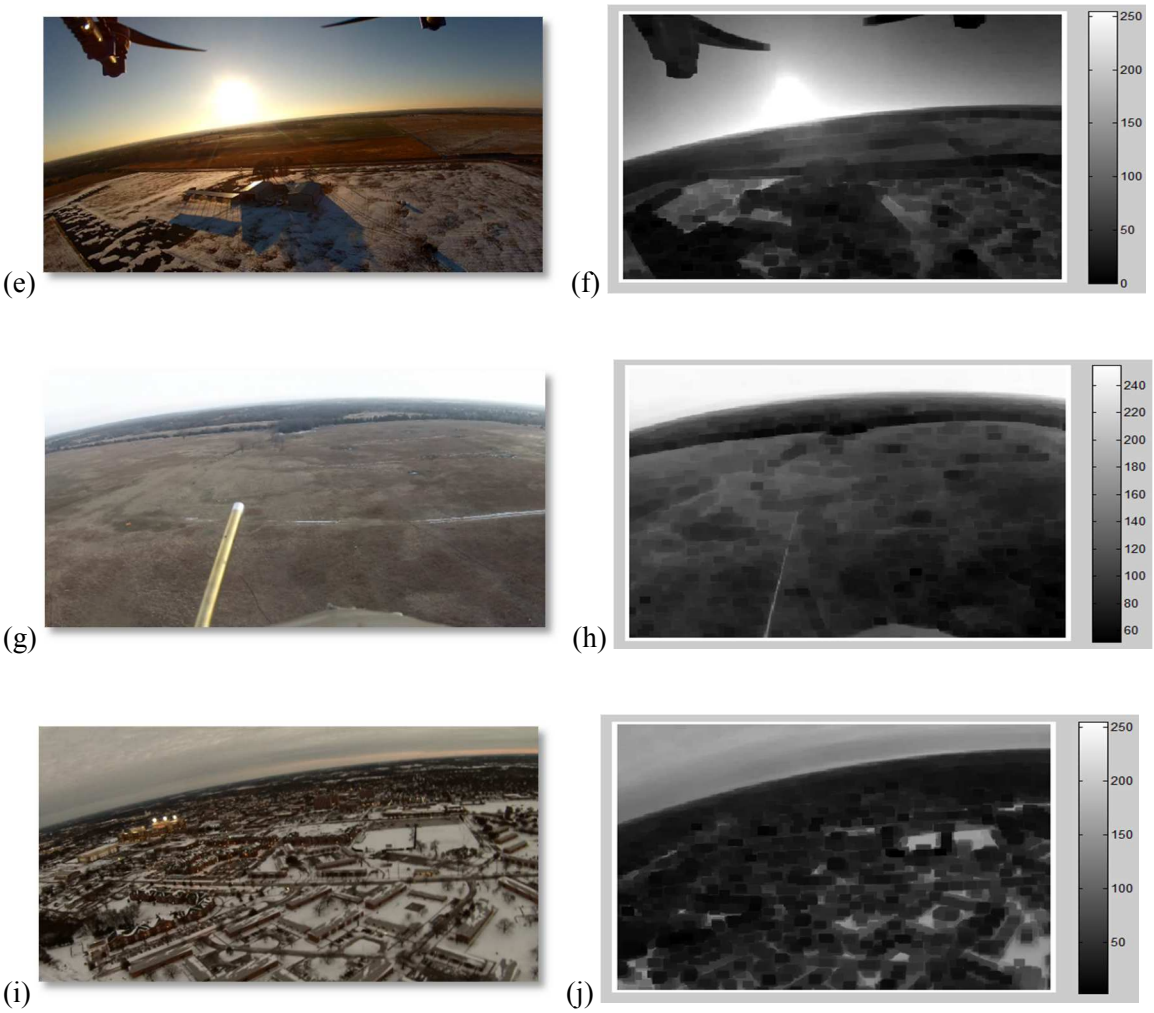

Figure 23 - The dark channel results from the test images.

One smoke video was tested for the overall effectiveness of the dark channel test for smoke detection. The first images are the background image from before the smoke plume is apparent and its dark channel values, as calculated above. The second images are the foreground image once the smoke plume has developed. The last image is the difference in dark channel values.

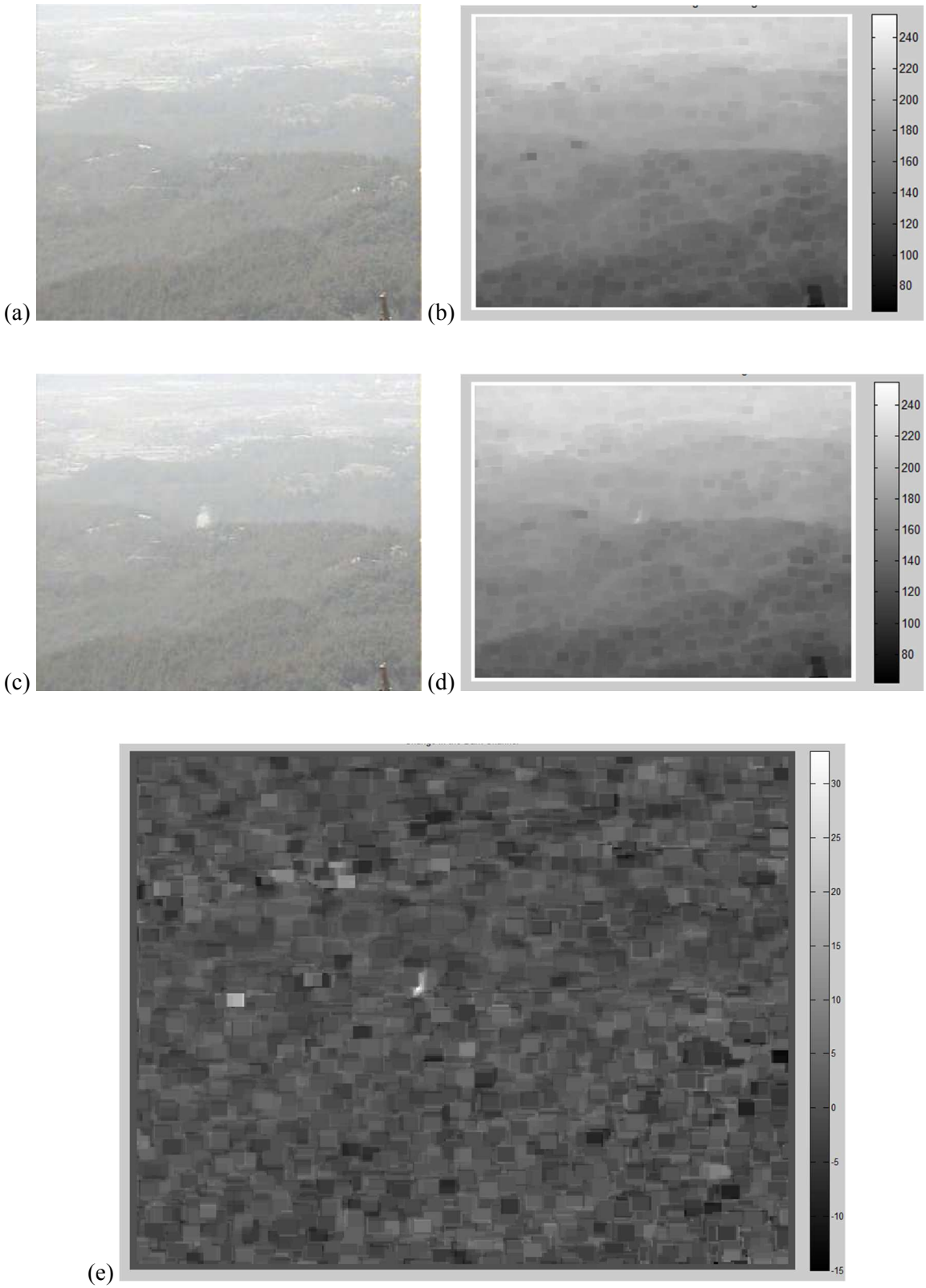

Figure 24 - (a) The background image, (b) its dark channel image, (c) the smoke image, (d) its dark channel image, (e) the increase in dark channel values from background to smoke images.

The dark channel difference image does seem to capture a small portion of the smoke plume, but it does not add any information that color image background subtraction would not give. Also, depending on the threshold set for triggering an alarm, this technique would allow several false positives resulting from a change in background illumination.

A more complex technique uses wavelet transforms, similar to those used in image compression, to determine high frequency energy in an image. The following transformed images were found using the "dwt2" function in MATLAB. In theory, a smoke plume should have less high frequency energy than the background, because the smoke tends to blur the pixels it covers. This technique appears to have some promise. The thin smoke at the top of the fire image does have a very low value. However, the thick smoke at the bottom of the image has some high values, due to its sharp edges. The foggy image, (c), seems to have a lower value throughout the entire image than in the smoke plume in image (a). Also, the low values at the top of the fire image do not appear to be any lower than the smoke-free background along the left side. If we were to observe several frames as the smoke plume started to form, then we may have seen a stronger indication of smoke obscuration. Wavelet transforms like this are an important part of many successful indoor smoke-detection techniques. This type of analysis may require a highly stabilized camera which can observe minute changes in energy between frames without creating false positives from illumination changes, fog, or haze.

(a)  (b) 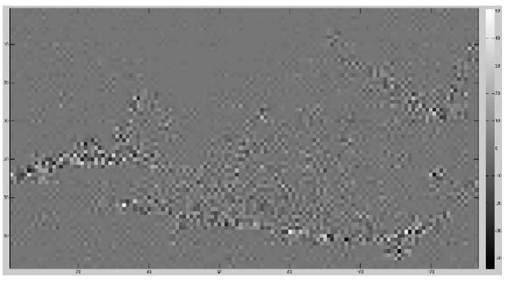

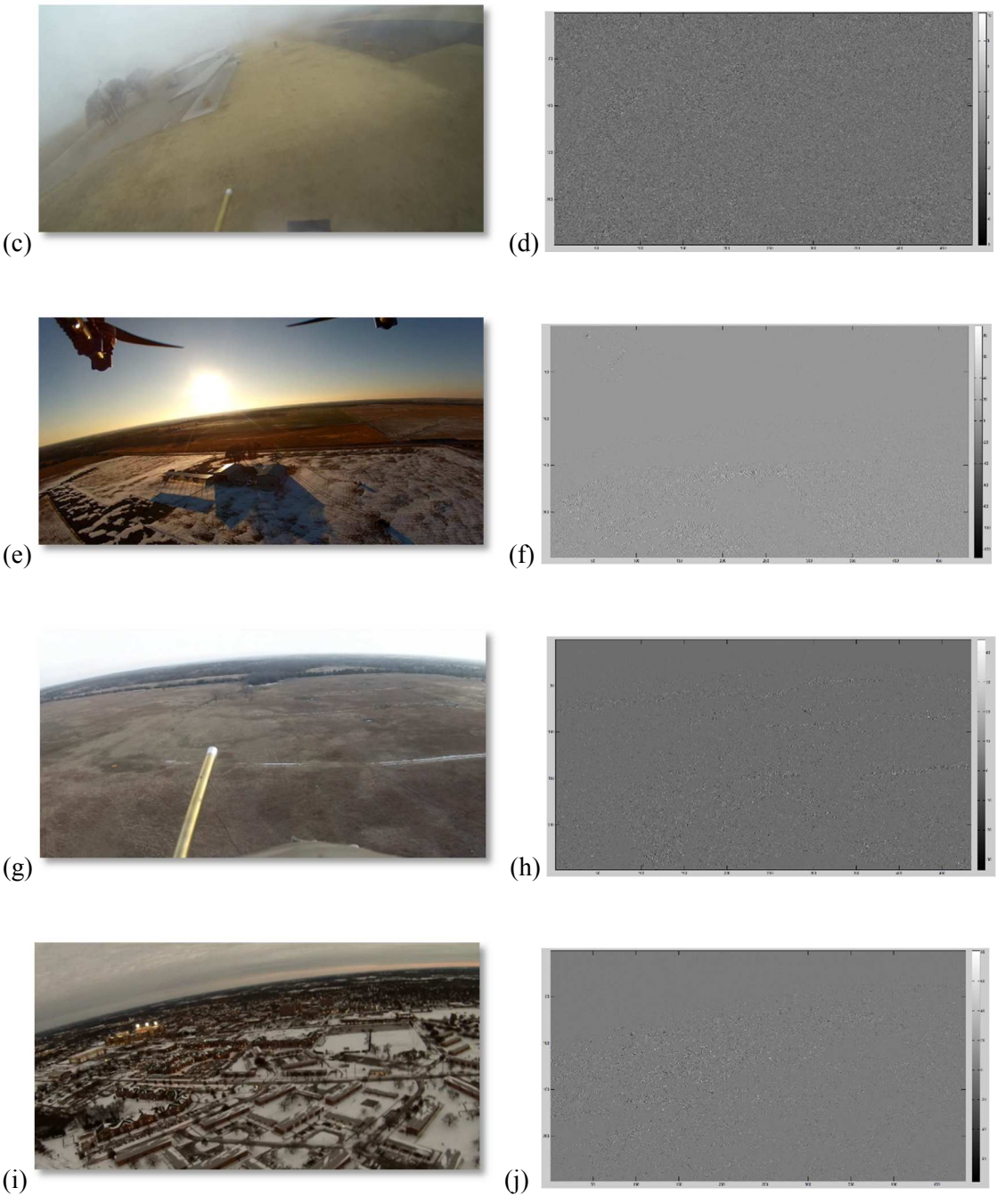

Figure 25- The high frequency wavelet transform of the test images.

The wavelet transform was also applied to two subsequent images taken from a down facing camera over a controlled burn on January 30, 2105. The figure below illustrates the results of that process. This might be the ideal condition for the wavelet transform. The background – the ground – is highly textured and the light wind makes the smoke visible and opaque without

completely obscuring the background. The results show a clear reduction in high frequency energy in the area obscured by smoke. This technique shows some promise for real-time smoke detection from an airborne platform.

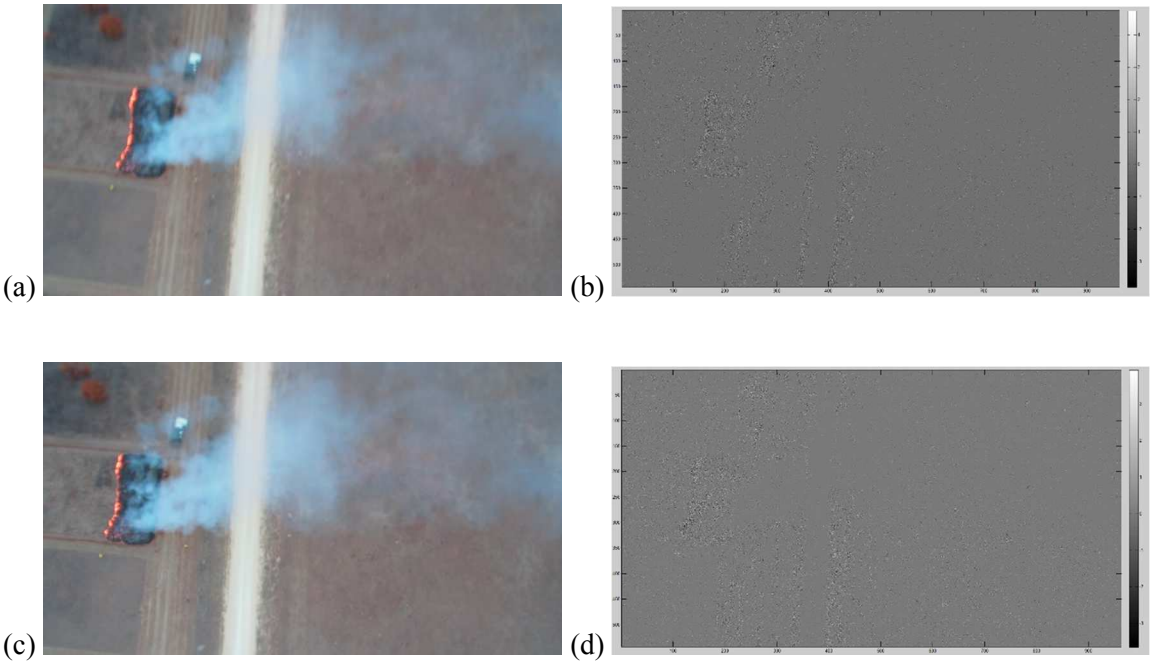

Figure 26 - (a and c) Images from a flight over a controlled burn. (b and d) Their high frequency wavelet transforms, respectively.

The previous techniques are generally spatial in nature, or corresponding to a single frame. A very common temporal algorithm involves the calculation of optical flow, or

$$I(u + \Delta u, v + \Delta v, t + \Delta t) - I(u, v, t) = \frac{\partial I}{\partial u}\Delta u + \frac{\partial I}{\partial v}\Delta v + \frac{\partial I}{\partial t}\Delta t = 0$$

in the vicinity of each pixel in the current frame. The time derivative is found by differencing the corresponding pixels from adjacent frames, and the u and v derivatives are determined from the neighboring pixels. Dense optical flow was calculated using Sun, et al. [2010], which is not compatible with real-time processing but is a good benchmark for other techniques. This dense optical flow was used to determine if the two-axis STELLA gimbal would reduce the pitch and roll motion to sub-pixel levels, which would be necessary in order to use any of the temporal

techniques for video smoke detection in the literature. The camera took video inside the lab while the gimbal base was waved back and forth by hand. The gimbal was rotated at an average of about 120 degrees/second and translated at about an average of about 4 feet/second. This is the results from optical flow taken at two separate instances in the video. The images are from subsequent frames, so they are separated by approximately 33 milliseconds. The second set of images represents the optical flow estimates for each pixel. The first image represents the right motion, and the second represents the up motion.

(a)  (b) 

(c) 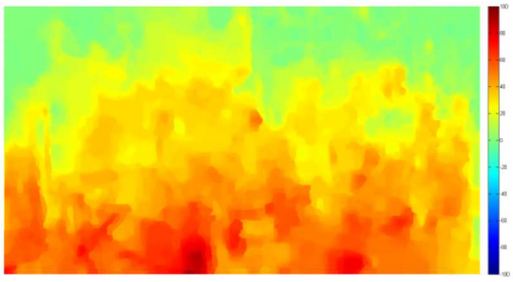 (d) 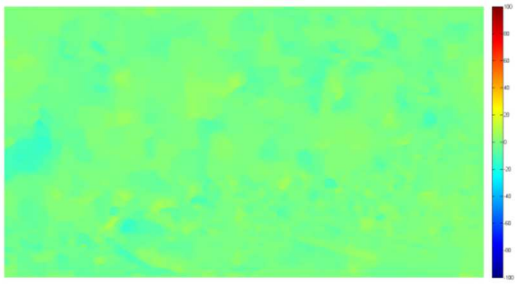

Figure 27 - (a) The first image, (b) the second image, (c) the optical flow "right,", and (d) the optical flow "up."

These results are inconclusive, and so a second test was also performed, approximately 3 seconds after the first in the video. The results are displayed below, in the same format as above.

(a) 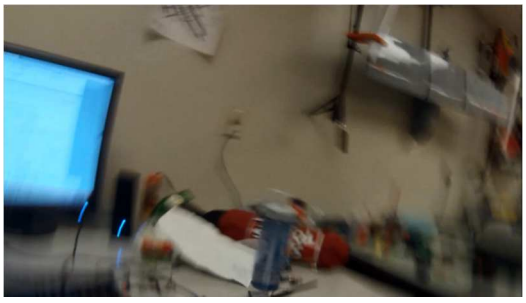 (b) 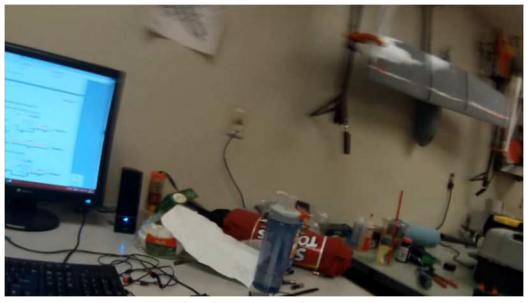

(c) 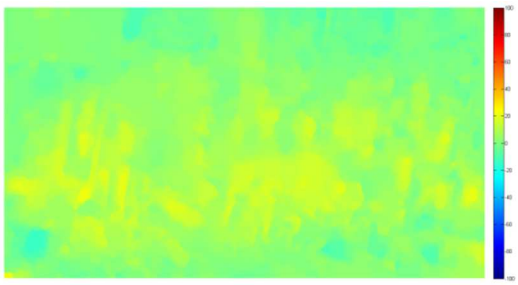 (d) 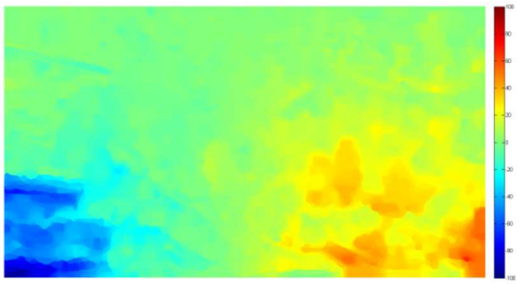

Figure 28 - (a) The first image, (b) the second image, (c) the optical flow "right,", and (d) the optical flow "up."

Some reasonable conclusions can be drawn from this second image set. First, the rightward motion (left image) seems to be almost symmetric from top to bottom. This situation would imply that there is little or no rotation in the image. Not that the increased motion in the center of the image is likely due to the fish-eye effect of the GoPro camera. The upward motion is more chaotic. The bottom half looks like an extreme counterclockwise rotation, with the largest movement close to 10% of the image height. The top half, of the other hand, appears to have a much smaller rotation, closer to 2% of the image height at the edges. Inspecting the images, one can easily see that blurriness in the left image could contribute to erroneous optical flow results in the bottom left and bottom right of the images.

These results are far from conclusive, but unfortunately the STELLA gimbal was damaged before any further tests could be performed. The initial tests do seem to imply that any motion detected in video footage could be the result of blurriness or lag in the GoPro autofocus or processing, rather than actual camera rotation. Further testing of the STELLA gimbal in flight would be required before any conclusive results could be taken, but initial results appear to show that the gimbal could potentially minimize camera rotational ego-motion to sub-pixel levels.

Optical flow was also evaluated in the segregation smoke pixels when viewed from above. This is a very difficult scenario for color smoke detection since the background – the ground – can have a variety of colors within a single frame. Optical flow was tested to determine if noticeable

discontinuities could be found in video taken from a slow-moving (on the same order as the smoke motion) aircraft, in this case the Phantom quadcopter. The following images were taken from a flight over a controlled burn. These images are 3-channel NIR/G/B color from a down facing camera. They are blurry due to the autofocus lag inherent in video taken from a moving platform. The Laplacian of the optical flow field shows the large discontinuities that highlight the entire smoke plume.

(a)  (b) 

(c)  (d) 

Figure 29 - (a) the first frame, (b) the second frame, (c) the optical flow directional orientation, (d) the Laplacian of the optical flow field.

Two tests were performed in order to extrapolate the results of Davenport [2012], which claimed that SWIR and LWIR were not useful for smoke identification when compared to visible colors, into the NIR spectrum. The first test confirmed the uselessness of NIR information for smoke identification. The images below are of a smoke plume several miles away in front of a setting sun with no clouds, where infrared information may be most useful because the smoke would scatter the sunlight as it passed through the plume on the way to the camera. From the first picture, smoke makes a vertical plume in the center of the picture and wind shear is causing a separate plume to the right of the first to become more horizontal, spreading to the right as

viewed in the picture. The second picture shows the NIR channel alone, where the vertical smoke plume is weak and the horizontal plume is barely visible. The third and fourth pictures show the green and blue channels, respectively, where both plumes are much more identifiable.

(a)  (b) 

(c)  (d) 

Figure 30 - (a) an image of smoke, (b) the NIR channel, (c) the Green channel, (d) the Blue channel.

Another image set was also evaluated for the effectiveness of NIR information for smoke detection with a thick plume from about 100 feet away, this time integrating the red channel into the test. The first image is a RGB color image taken by an iPhone 4. The color channels are again broken down to illustrate the effectiveness of each one for smoke plume identification. The second picture is the same scene taken with the Canon color NIR camera. Here the channels are also broken down to compare to the first image. The RGB image was taken about 1 second before the color NIR image, to the smoke plumes have drifted slightly up and right in that time.

(a)  (b) 

Figure 31 - (a) An RGB image of thick smoke and (b) an NGB image of the same scene.

Though NIR may give more useful smoke identification information than shortwave IR or longwave IR as tested by Davenport (2012), it is still performs very poorly when compared to color information.

3. FUEL MAPPING

NGB images and videos used for fuel mapping were taken at the OSU Fire Ecology test ranges near the Marena Mesonet station. Blurry images were manually removed and the remaining 262 images were combined in Microsoft Photosynth to create a photomosaic for color manipulation. The images were also input to Agisoft Photoscan and Pix4D to create 3D point clouds for geometric measurements. The first flight was taken, during a controlled burn of one of the plots. The results of the photogrammetry steps are shown below, with a similar scene taken from Google Maps for comparison.

The images show that Pix4D can create a photomosaic that is more correlated with the ground truth than the free Photosynth. However, the Pix4D software took hours to compile the images into a point cloud, whereas Photosynth provided a solution in about a quarter of that time. Pix4D

eliminated some of the blurriness from the smoke and the bright spots from the fire, whereas Photosynth kept them both since it simply combines images like a panorama. If Pix4D cannot find a particular feature in enough images then it discards them. The constantly changing smoke plume and moving fire is not a good target for this kind of reconstruction. Also, Pix4D was more likely to throw out the far North and South features. These images were taken while the aircraft was in a bank, so they were likely thrown out because they did not have a straight nadir point of view, as a result or the aircraft-fixed camera mount.

Figure 35 shows the output of each program: (a) is a Google Maps clip of the area, (b) is the Pix4D point cloud from above, (c) is the Agisoft Photoscan point cloud from above, and (d) is the Photosynth photomosaic. Pix4D created a more detailed photomosaic than Photoscan, as pointed out in (AirGon, 2015), but otherwise the two images are similar.

(a)  (b) 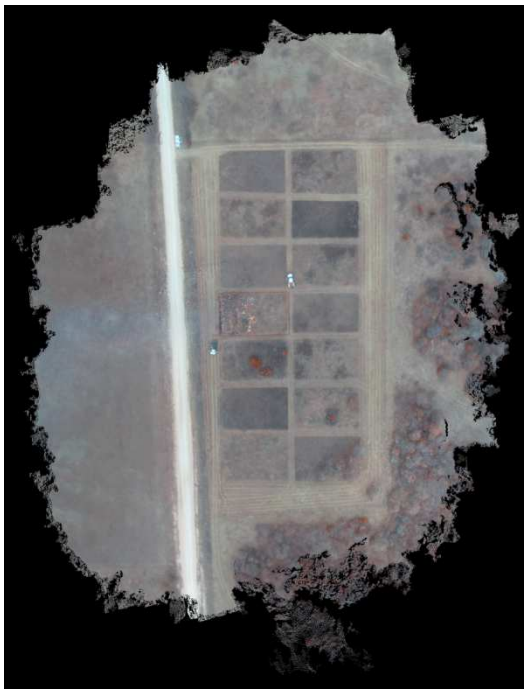

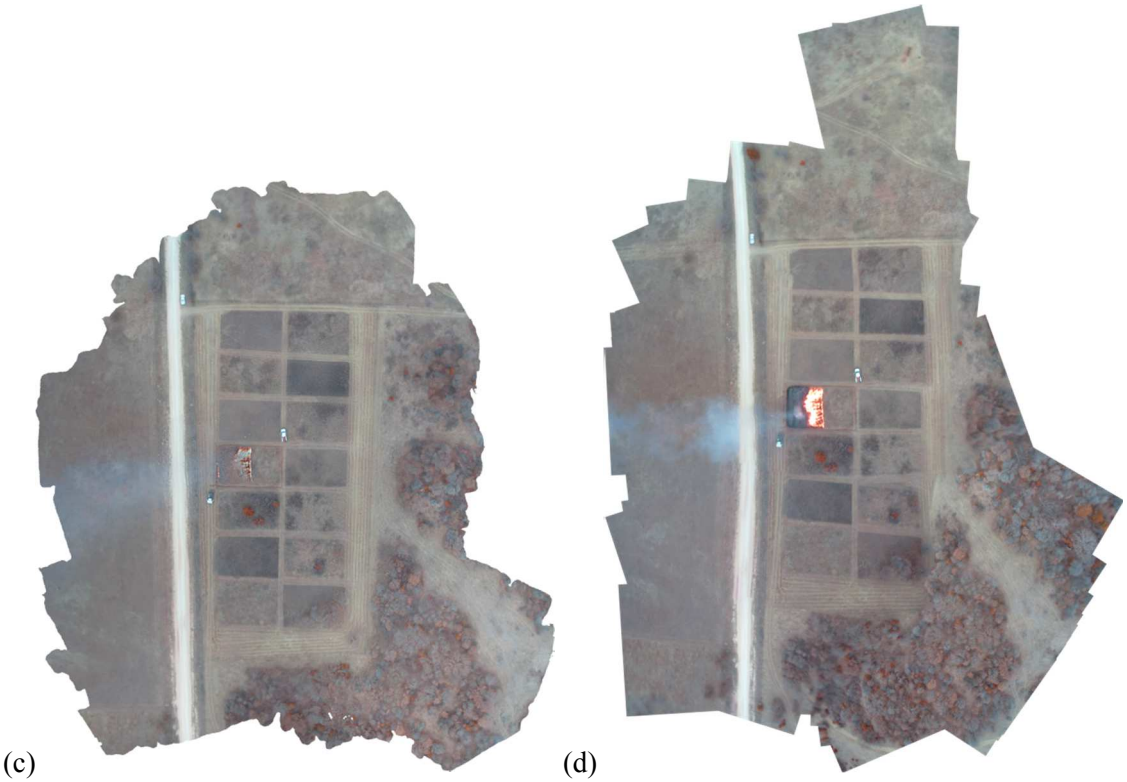

(c) (d)

Figure 32 - (a) A Google Earth image of the test plots, (b) A Pix4D mosaic, (c) an Agisoft Photoscan mosaic, and (d) a Microsoft Photosynth stitched image.

Agisoft Photoscan was able to capture more of the fire and smoke features that Pix4D, though it is still much less than the stitched image produced by PhotoSynth.

For comparison, another flight was made on February 12. Several flights were made at another controlled burn site that day, and only one flight was made over the test plots, with the plots not burning. The images were sampled from video taken with a down-facing camera. Again, blurry images were manually removed, and only the best 316 images were used. The following images are (a) the Google Maps image of the test plots, (b) a Pix4D point cloud of the plots, (c) an Agisoft Photoscan point cloud, and (d) a Photosynth photomosaic of the plots. Obviously, Photosynth failed to create a useful photomosaic with the images provided. All of the images including the operator were removed on the assumption that a moving operator was the cause of the failure. This improved photomosaic is shown as (d). Even this improved product gives greatly distorted proportions when compared to the SfM programs.

(a)  (b) 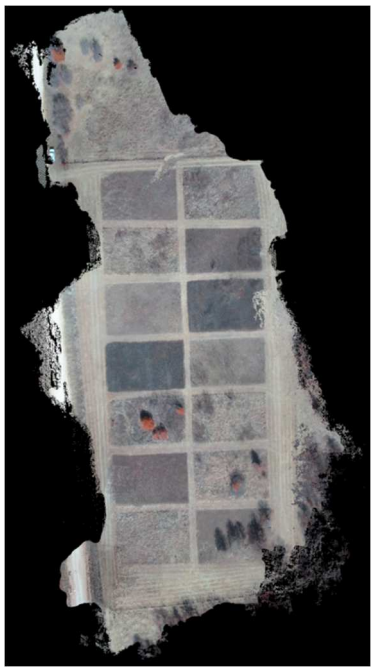

(c)  (d)  (e) 

Figure 33(a) A Google Earth image of the test plots, (b) A Pix4D mosaic, (c) an Agisoft Photoscan mosaic, and (d) a Microsoft Photosynth stitched image, and (e) another Photosynth image with images selectively removed.

The pictures clearly show that Microsoft Photosynth images have a much greater distortion than either SfM program, even when this program is using images that are not geotagged with GPS

latitude, longitude, and altitude. Tagging images with GPS position or manually adding georeferenced points to the point cloud (such as known locations at the corners of plots) would further reduce the distortion. The advantage of stitching programs like Photosynth is the processing time required. For example, all of the Photosynth mosaics took on the order of 20 minutes to process, whereas Pix4D and Photoscan required between 4-6 hours to produce a dense point cloud. Even with this reduced processing time, Photosynth was prone to breaking or freezing with certain image sets.

We also demonstrated the capabilities of the CKHD loaded on the Canon SX260 HS. This kit allows the camera to operate from an alternate menu, allowing reprogrammed scripts such as "Shot Interval." Using this script, the camera was programmed to capture one image every two seconds, up to 300 images (approximately 10 minutes of flight time). These images would be taken at 12 Megapixel resolution, approximately 6 times higher than 1080p video, and would be geotagged with latitude, longitude, and altitude from the internal GPS receiver.

This feature was also tested at the two previous flights (January 30th and February 12th), but each time the camera failed to take more than a few pictures before encountering an error and ending the process. The company that modified the camera suggested that vibrations were causing an error in the camera's internal clock. A UAS with higher ground clearance was purchased so that vibration isolators could be mounted between the aircraft and the camera. Fortunately, once the pilot was aware of the problem he was able to reduce vibrations by performing only smooth, low-power maneuvers during flight. At the March 20th flight, under the new flying procedure, the error was not encountered, and all three flights captured still images from takeoff to landing without a failure.

As stated above, three test flights were performed on March 20th. The first flight was performed at a beginning of a small prescribed grass fire approximately two miles East of the test plots. The

second was performed near the end of that burn, in order to test the capability of NIR imagery to locate hot spots on the ground during mop-up operations. The third was performed at the test plots in order to compare the SfM and bNDVI results with the previous two flights.

The plots were analyzed from the March 20th flight just like as in the two previous flights. By eliminating only those images where the camera was too close to the ground to gather any useful information, 186 images were chosen to analyze the plots. Because the images were all geotagged, the initial processing steps took approximately half as long as with the images ripped from video. On the other hand, the higher resolution produces almost ten times the number of distinguishable points per image, from just over 4000 to up to the maximum of 40,000 points in Agisoft. Pix4D found an average of 17,116 points per image, with the highest image having 72,860 recognizable points. The result was a greater processing time, but a much clearer mosaic. Agisoft was not able to use the highest resolution available for the dense point cloud. At the highest resolution, resulting mesh, which uses a 14 level tree search, required more than the 16 GB of memory available on the processing computer. By using the second highest resolution setting, almost 50 million points were identified and the mesh calculations required 12 GB of memory. Figure 36 shows the resulting mosaics, followed by the approximate processing time in parenthesis. (a) Google Earth clip for reference, (b) Agisoft (4 ½ hours for the dense point cloud, 10 hours total for the mosaic), (c) Pix4D (2 hours total), and Microsoft Photosynth (20 minutes). The decreased processing time for Pix4D is partly due to that program's ability to make assumptions based on the camera calibration estimates implanted on all Canon SX260 HS images.

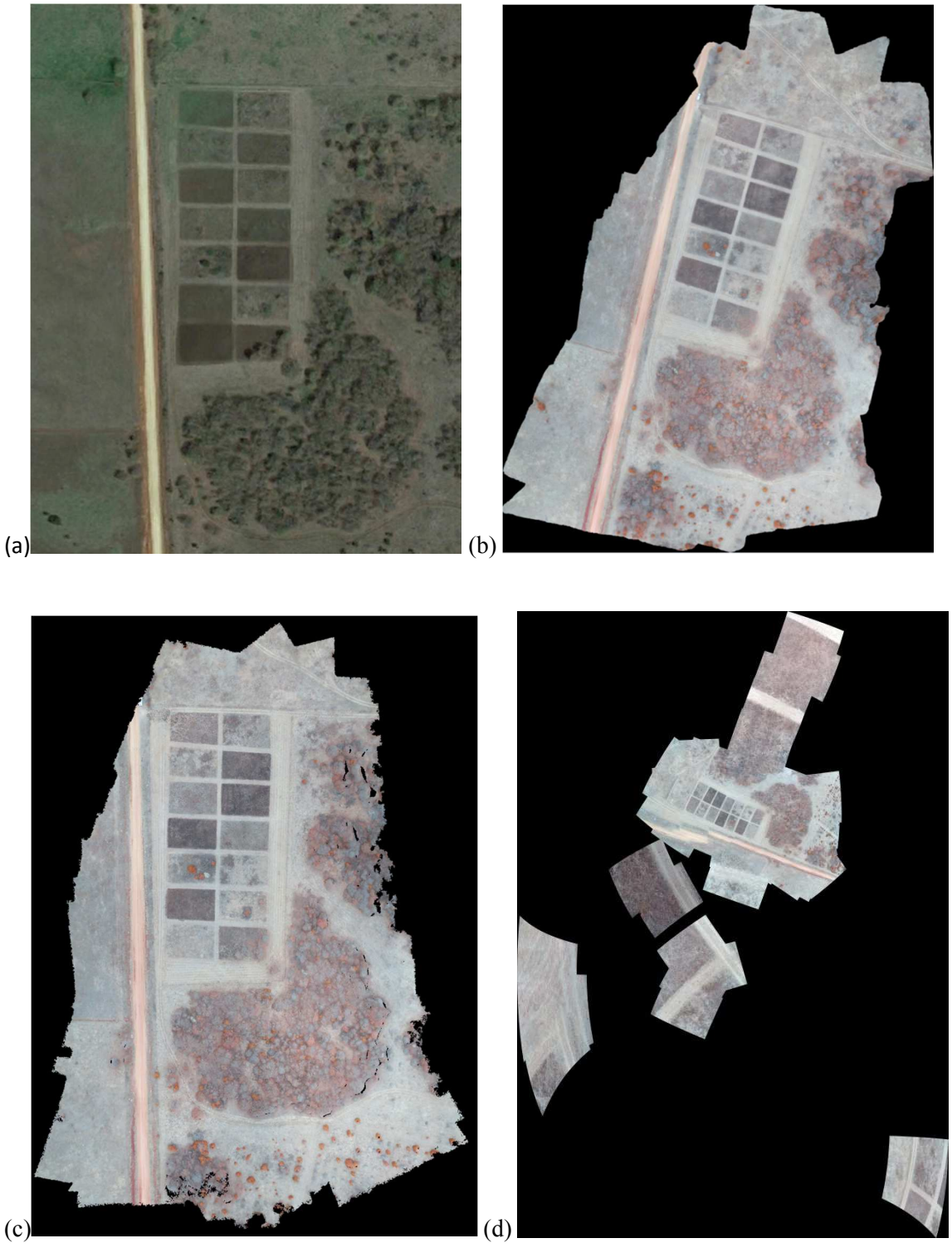

Figure 34 - (a) A Google Earth image of the test plots, (b) an Agisoft Photoscan mosaic, (c) a Pix4D mosaic, and (d) a Microsoft Photosynth stitched image.

Photosynth again failed to create a useful mosaic from the images. This program will no longer be considered as a candidate for any image processing. Two tests were performed to determine the variability of two flights taken under the same conditions. Below are the mosaics produced on both flights using Agisoft Photoscan, then Pix4D.

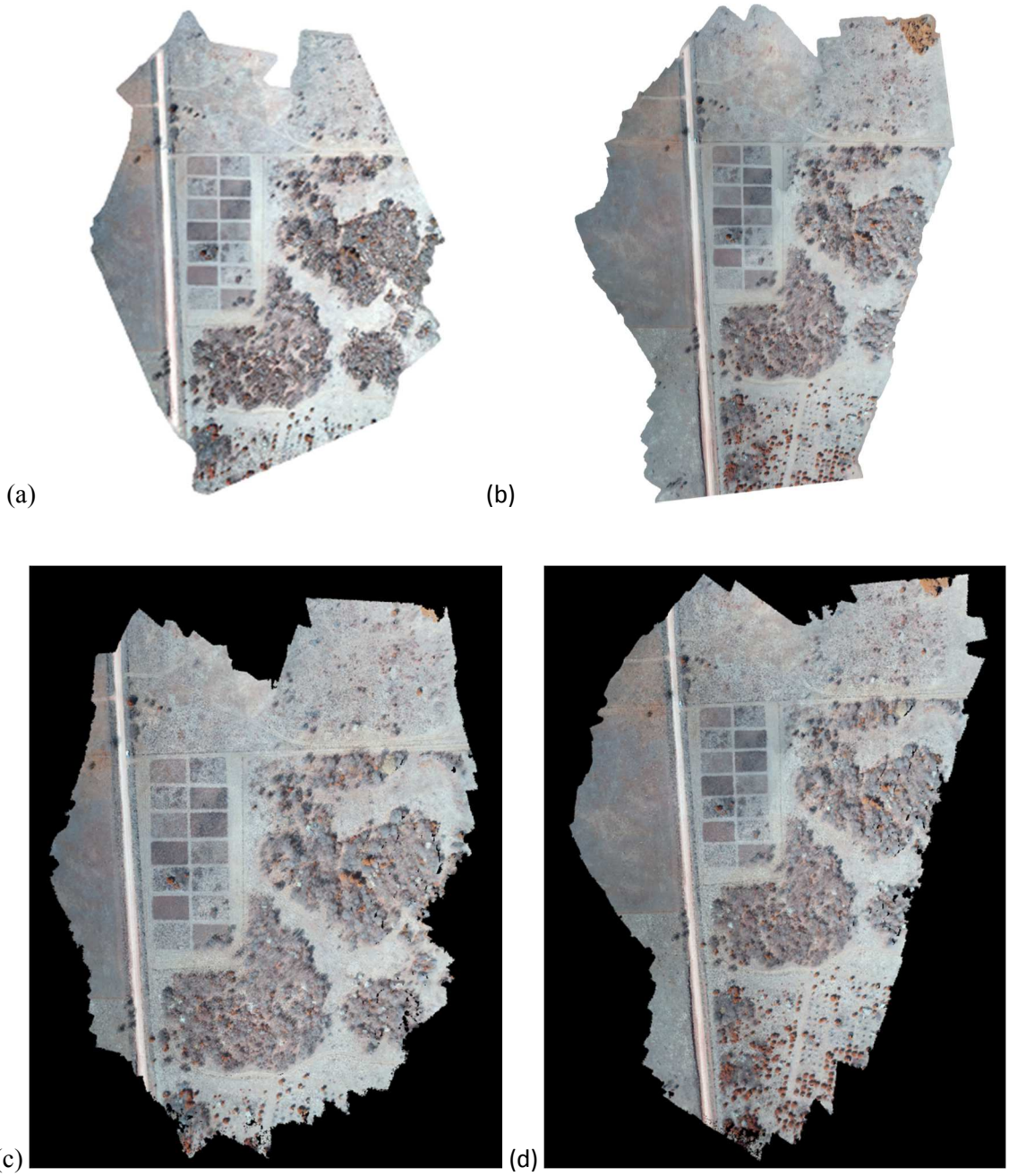

Figure 35 - (a) An agisoft mosaic from the first flight, (b) an agisoft mosaic from the second flight, (c) a Pix4D mosaic from the first flight, and (d) a Pix4D mosaic from the second flight.

These mosaics show variability in the NIR reflectance that is not evident in color imagery (see Google Earth map). This NIR reflectance, combined with prior knowledge of local species could be used to train a classification program that could autonomously separate fuels by type. For example, the big bright red tree on the fifth row is an Eastern Red Cedar, and the smaller trees and shrubs are Mexican Plums, Post Oaks, and several Winged Sumac shrubs. Information like this could be extrapolated over the local area to classify a number of fuel types without increasing a land manager's workload. Implementation of this type of classification is beyond the scope of this paper, but the large differences in NIR reflectance (interpreted as the RED channel in the above mosaics) between trees could provide a level of distinction that color imagery cannot, in the context of autonomous fuel classification.

Pix4D provides information on the calibration of images and the accuracy of geolocation of geotagged images. Geolocation error (RMS error x/y/z) is the difference between the initial and computed image positions, and it is not a primary indicator of the accuracy of the 3D points. The following table summarizes the results from the three flights over the test plots.

DATE	Calibrated Images	Mean Reprojection Error (pixels)	Geolocation Error		
			RMS X	RMS Y	RMS Z
Jan 30	237/262	0.199	N/A	N/A	N/A
Feb 12	163/316	0.291	N/A	N/A	N/A
March 20	135/186	0.162	4.94%	8.57%	14.50%
March 27	167/185	0.208	8.81%	13.01%	22.15%
March 27	167/184	0.204	6.84%	11.55%	13.71%
Advertised GPS Accuracy			5%	5%	10%

Table 2 - Pix4D error calculations from all five mapping flights over the test plots.

The alternate blue Normalized Difference Vegetation Index (bNDVI) was also calculated for each pixel of the photomosaic using the following formula.

$$NDVI = \frac{NIR - VISIBLE(BLUE)}{NIR + VISIBLE(BLUE)}$$

Where NIR is the spectral reflectance measured in the band (690 to >800 nm), and BLUE is the spectral reflectance measured in the band (380 to approximately 450 nm) according to the following chart from the manufacturer's website. [event38.com]

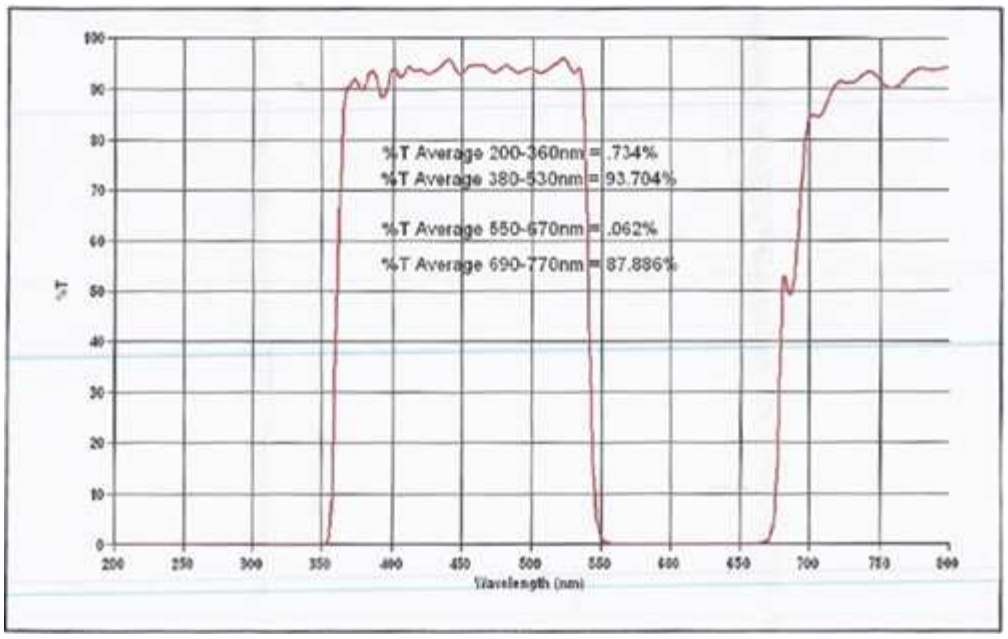

Figure 36 - The spectral characteristics of the NIR (minus red) filter on the modified Canon camera.

Because chlorophyll absorbs red and blue radiation but not NIR, NDVI (or bNDVI) is an indicator of chlorophyll content, normalized to the range [-1,1]. Higher NDVI or bNDVI values in the image likely indicate higher chlorophyll content in the plant. In low-moisture plants like grasses, chlorophyll content is a good indicator of moisture content. The images below show the photomosaic from the January 30th flight from Agisoft PhotoScan, Pix4D, and Microsoft Photosynth, respectively, on the left, and their corresponding bNDVI image on the right.

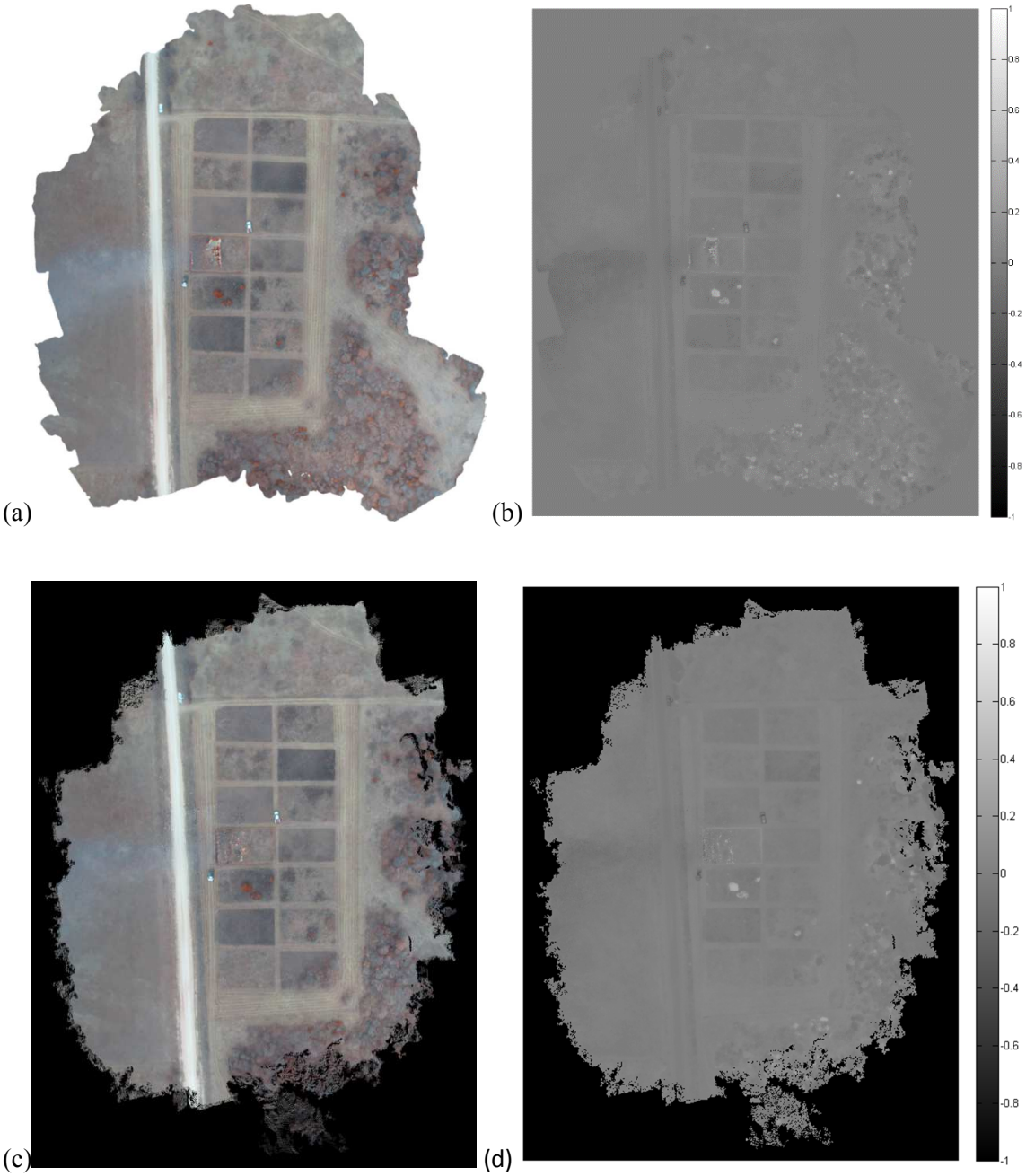

Figure 37 – (a) A Agisoft mosaic, (b) its NDVI map, (c) a Pix4D mosaic, (d) its bNDVI map.

OKFIRE provides a way to compare these measured bNDVI values to AHVRR satallite data compiled weekly by the EROS Data Center, U.S. Geological Survey. OKFIRE uses “greennesss”

satellite maps of Oklahoma updated every seven days using NDVI, caculated with the following formula.

$$NDVI = \frac{NIR - RED}{NIR + RED}$$

Where NIR is the spectral reflectance measured in the band (720-1000 nm), and RED is the spectral reflectance measured in the band (572-703 nm). OKFIRE is in the process of transitioning from AVHRR to MODIS spectral data by the end of 2015. MODIS provides a finer spectral resolution (841-876 nm for NIR and 620-670 nm for RED) and a finer spatial resolution (500 meter pixels instead of 1 km). [Carlson email, March 2015] Below are two greenness maps generated by OKFIRE for the week of January 30th.

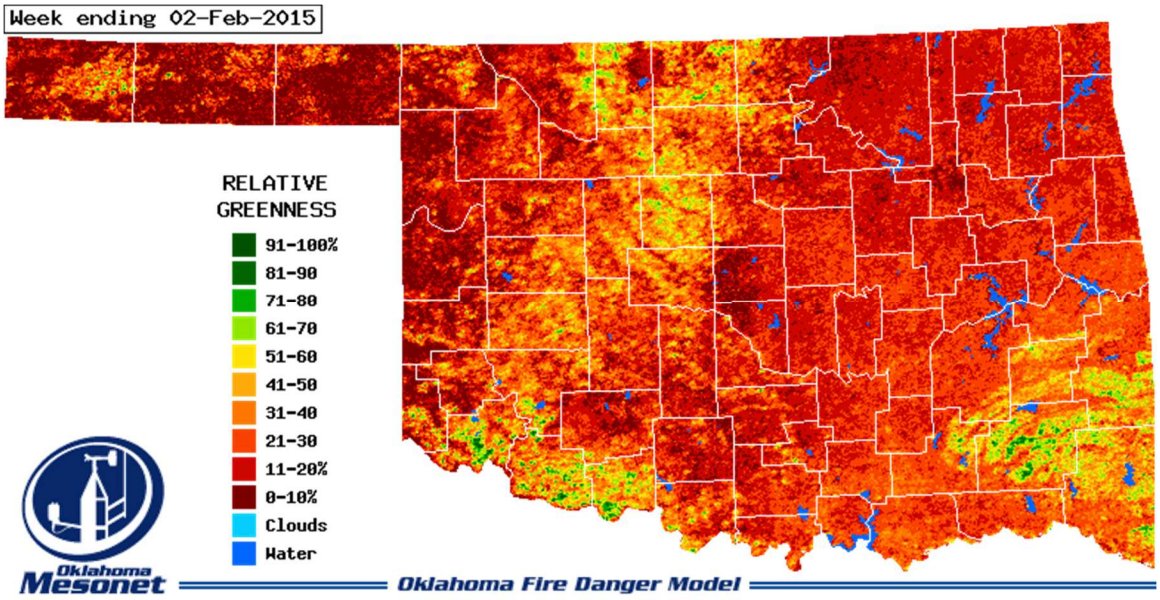

Figure 38 - An OKFIRE Relative Greenness map

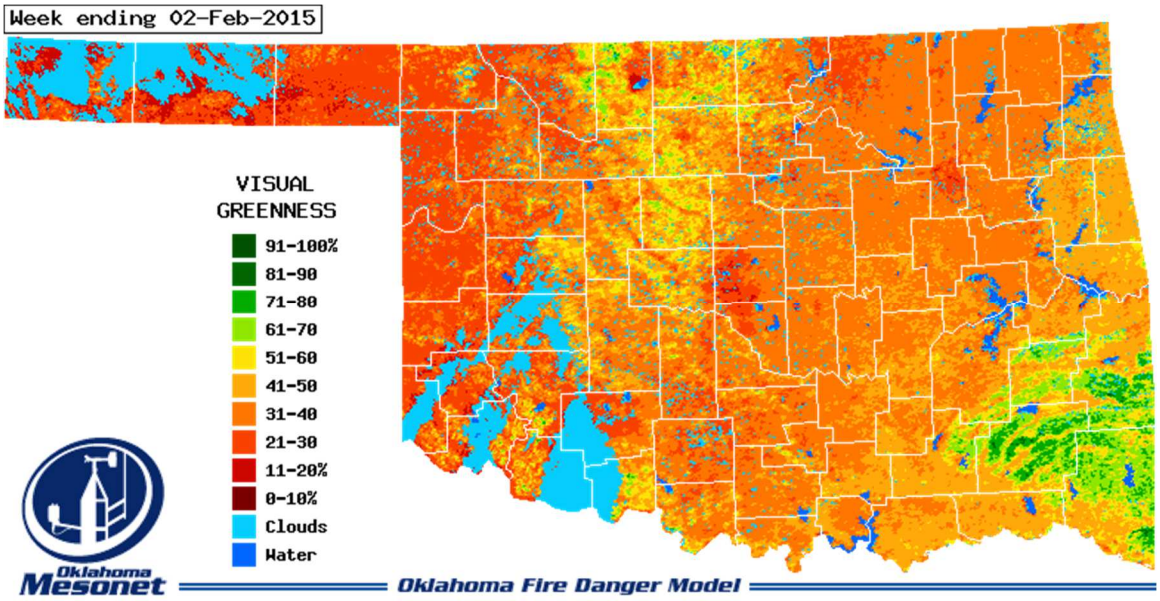

Figure 39 - An OKFIRE Visual Greenness map

Because these values are based on multispectral satellite data, they are only available with a spatial resolution of 1 km per pixel, which would put the test site in either the same pixel or an adjacent pixel to the Marena Mesonet site 400 meters to the west. OKFIRE database gives a Visual Greenness (VG) value of 38% and a Relative Greenness value of 23% for the Marena site that week. The test lasted approximately nine minutes. The weather conditions from Oklahoma Mesonet before and after the flight are noted below. All calculations are based on the "Tallgrass with brush" model. For more information about what these variables are and how they are calculated, see [Carlson, et al. 2002, Carlson and Burgan, 2003]

TIME	BI	SC	ERC	IC	1-HR	10-HR	100-HR	1000-HR	HERB	WOODY	KBDI	RAIN_24H
3:00 pm	21	9	7	7%	9%	12%	10%	9%	58%	95%	290	0.00 in.
2:00 pm	13	5	5	5%	10%	12%	10%	9%	58%	95%	290	0.00 in.

Table 3 - The weather and fire danger conditions during the January 30th flight, from the Marena Mesonet station.

According to OKFIRE website, RG is calculated with respect to a historical database for that particular pixel, and so it would not give an accurate representation of the raw spectral data without a long (16 years, in OKFIRE's calculation) history of that pixel's minimum and maximum NDVI values. RG is the value OKFIRE uses to estimate Life Fuel Moisture (LFM)

and to determine the distribution between 1-hour dead (1-h), live herbaceous (HERB) and live deciduous woody (WOODY) fuels. It is a crucial value to determine fire danger; however it is not evaluated in this study because (1) it is based on historical values that are not available at a fine spatial scale, and (2) it is dependent on VG, which can be directly compared to discrete measurements. VG uses only calculated NDVI as an input, and is calculated below:

$$VG = \left(\frac{NDVI}{0.66}\right) * 100\%$$

So a VG value of 38% would give an NDVI value of 0.25 for the 1km pixel containing the Marena Mesonet site. The NDVI values from the other flights have been calculated the same way and collected in the table below.

The average bNDVI value for all pixels in the January 30th mosaic is 0.0083 for Agisoft and 0.0016 for Pix4D, both of which are significantly lower than the OKFIRE calculations from that week. There are several possible reasons for the discrepancy. First, EROS published a 7-day composite image, keeping only the highest NDVI values gathered that week in order to minimize the effects of clouds, haze, off-nadir view angles, and other factors. [Burgan, et al., 1996] Agisoft Photoscan and Pix4D use the pixel values observed during the flight. Secondly, though the exact spectral bands of each channel in the Canon color NIR camera are not published, they appear to be more restrictive than the AVHRR bandwidths (280 nm wide for NIR, 131 nm wide for visible red light). Additionally, the Canon camera does not capture visible red light, and so blue light is substituted in the calculation since chlorophyll also absorbs light from that band during photosynthesis. However, it is possible that the photosynthetically active vegetation is absorbing more blue light than red light, depending on the exact spectral band measured. [McCree, 1972] The table below shows the comparison of OKFIRE's NDVI measurement for each flight with the bNDVI calculated from the average NIR and Blue values of the Agisoft and Pix4D mosiacs. Note the values are different than above because this is calculating bNDVI from

the average blue and average NIR, not averaging the bNDVI from each pixel in the image. This derivation using average values is more similar to satellite imagery, in which one pixel captures the total reflectance of a 1 km square for calculating NDVI. Also, it would be less computationally complex since bNDVI is only calculated once. bNDVI is calculated using this formula:

$$NDVI_{image} = \frac{\text{sum}(NIR) - \text{sum}(BLUE)}{\text{sum}(NIR) + \text{sum}(BLUE)}$$

DATE	**OKFIRE**		**Agisoft average**			**Pix4D average**		
	VG	*NDVI*	*NIR*	*BLUE*	*bNDVI*	*NIR*	*BLUE*	*bNDVI*
Jan 30, 2015	*38%*	*0.25*	*0.5391*	*0.5290*	*0.0095*	*0.5094*	*0.5047*	*0.0046*
Feb 12, 2015	32%	0.21	0.5714	0.5640	0.0065	0.5444	0.5390	0.0050
Mar 20, 2015	27%	0.18	0.6612	0.6472	0.0107	0.6572	0.6468	0.0080
Mar 27, 2015	31%	0.20	0.6669	0.6708	-0.0029	0.6203	0.6233	-0.0024
Mar 27, 2015	31%	0.20	0.6061	0.6046	0.0013	0.6000	0.6003	-0.0003

Table 4 - Average spectral measurements and calculated NDIV from five tests and two SfM programs.

Rearranged into a scatter plot, the values come to this:

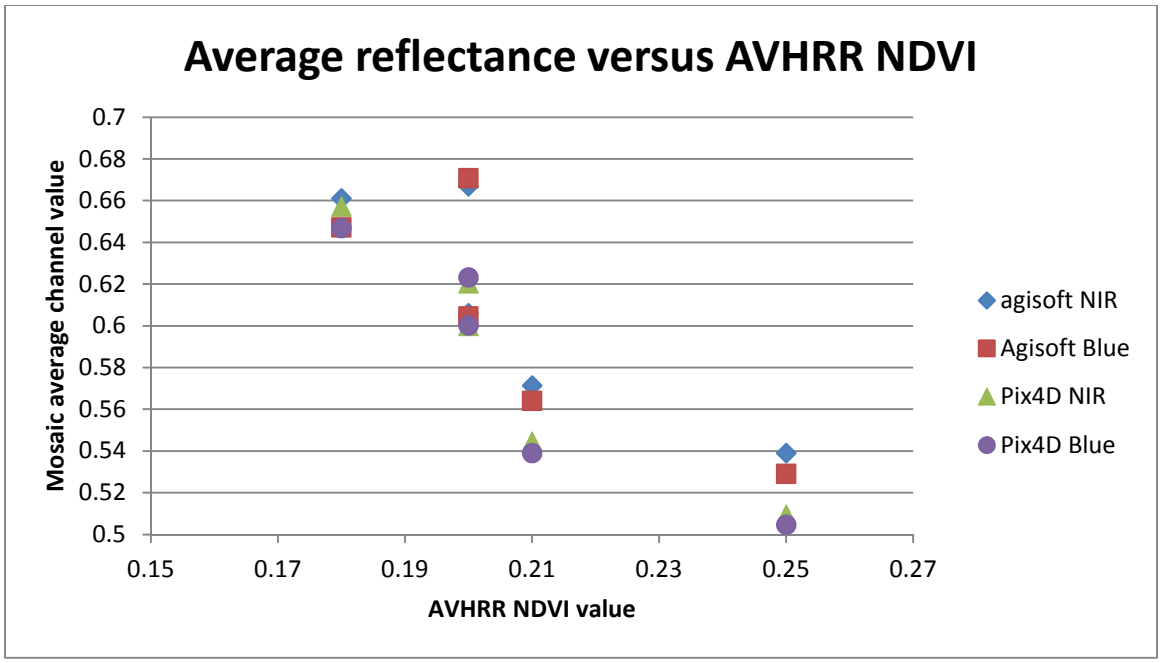

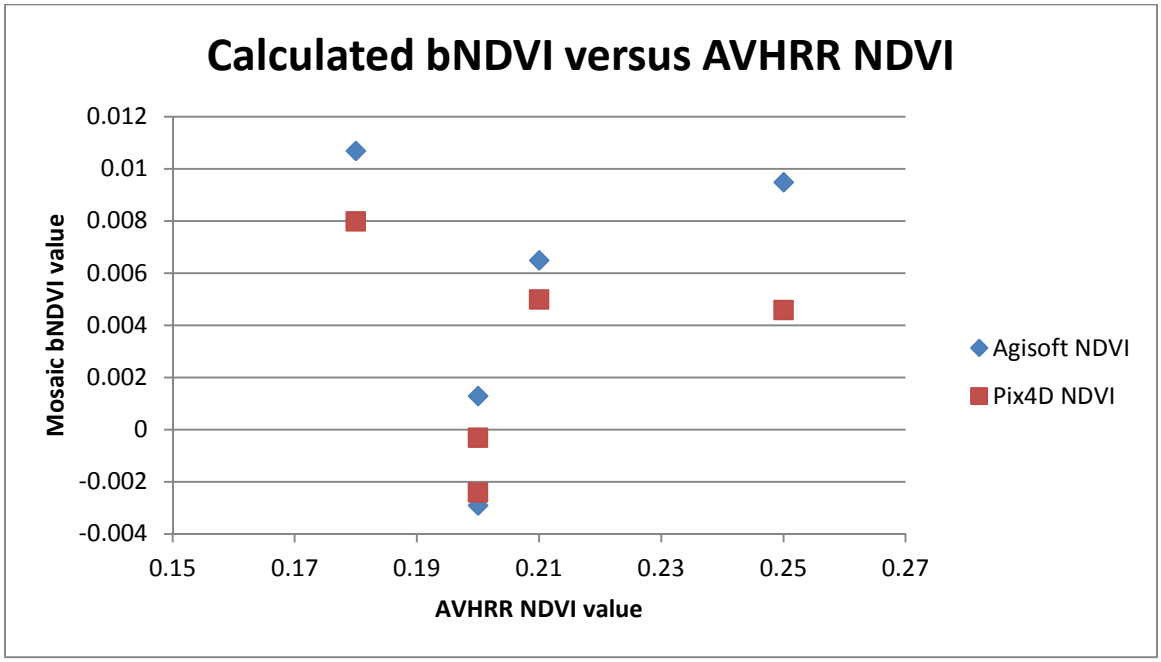

Figure 40 - Measured reflectance and calculated bNDVI plotted against EROS NDVI data from Marena Mesonet station.

The two flights in March 27th show that separate flights paths over similar areas under the same conditions can produce large variations in the average reflectance measured, as illustrated in the table below.

DATE	NIR		BLUE	
	Agisoft	Pix4D	Agisoft	Pix4D
27-Mar-15	0.6669	0.6203	0.6708	0.6233
27-Mar-15	0.6061	0.6	0.6046	0.6003
Mean	0.6365	0.61015	0.6377	0.6118
Variance	4.78%	1.66%	5.19%	1.88%

Table 5 - Variation from the mean for each program.

Despite the small sample size, there is an obvious difference in the consistency of the two programs. Pix4D appears to agree much better than Agisoft for this sample set, but more evaluation would be needed to determine the actual agreement. Additionally, the small value of bNDVI can vary widely due to these small changes, even becoming negative. As noted earlier in the work to use higher resolution MODIS data to calculate fire risk in Oklahoma, changing spectral bands can change the interpretation of the measured sepctral values. The following is an evaluation of the consistency of the measured NIR and BLUE reflectance values for estimating error bars.

The following table rearranges the reflectance values from table 4 in order to show the variance due to program choice. The error is half of the difference between the two values, as a percentage of the mean.

DATE	NIR			BLUE		
	Agisoft	Pix4D	Error	Agisoft	Pix4D	Error
30-Jan-15	0.5391	0.5094	2.83%	0.529	0.5047	2.35%
12-Feb-15	0.5714	0.5444	2.42%	0.564	0.539	2.27%
20-Mar-15	0.6612	0.6572	0.30%	0.6472	0.6468	0.03%
27-Mar-15	0.6669	0.6203	3.62%	0.6708	0.6233	3.67%

27-Mar-15	0.6061	0.6	0.51%	0.6046	0.6003	0.36%
RMS error			2.34%			2.20%

Table 6 - Variance from the mean of Agisoft PhotoScan and Pix4D average reflectance values.

This table shows that the difference due to program selection is very small variance due to choice of program. The highest variance from the mean notes was 3.67%, and the standard deviation for this set is 2.34% in NIR and 2.20% in BLUE. Given the goal of estimating relative fire danger of small plots, these small errors are probably acceptable.

Since the flights on March 20th and March 27th were also georectified, their topography can also be generated for vegetation volume estimates. The following is the results of using Agisoft Photoscan to create the digital elevation models of the three flights in .asc format (Arc/Info ASCII grid). The DEMs were then imported into ESRI ArcMap for GIS comparison with the curent USGS 30 meter DEM, represented by a contour map in the images. The GIS data shows that the highest point in the plots is northwest corner, and the lowest point is the southeast corner. The following figures illustrate these results.

Figure 41 - USGS 30 meter DEM contour map (10 foot contour intervals) of the test plots

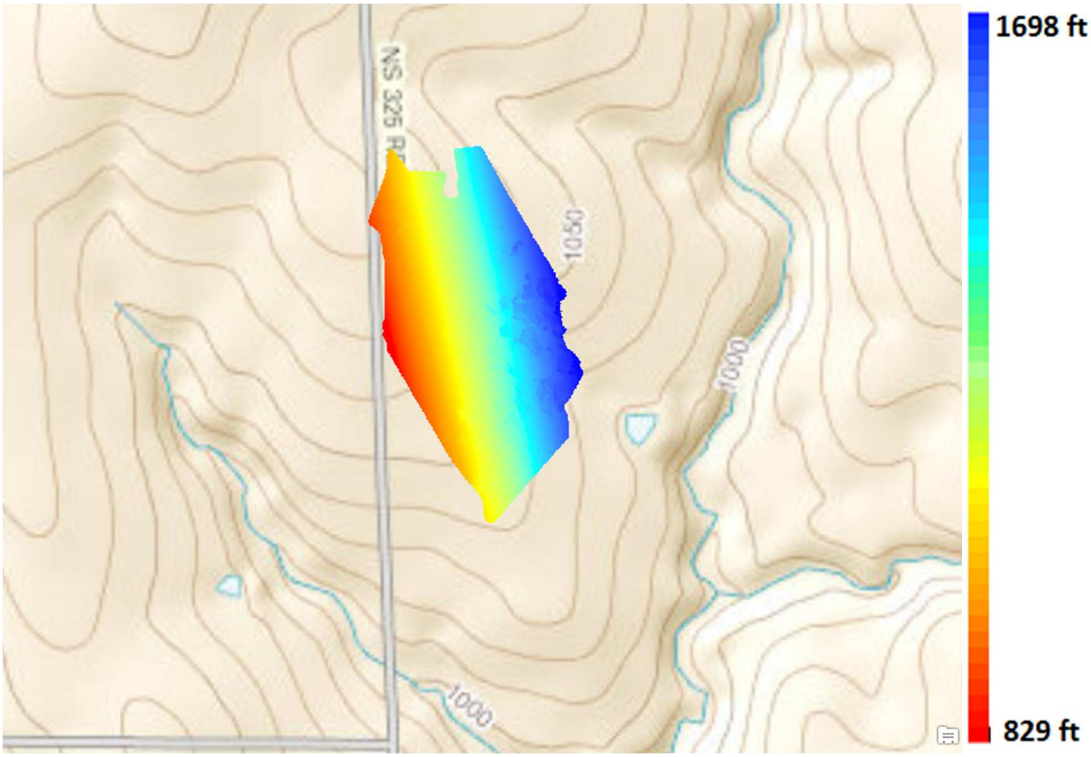

Figure 42 - DEM from the first flight on March 27th

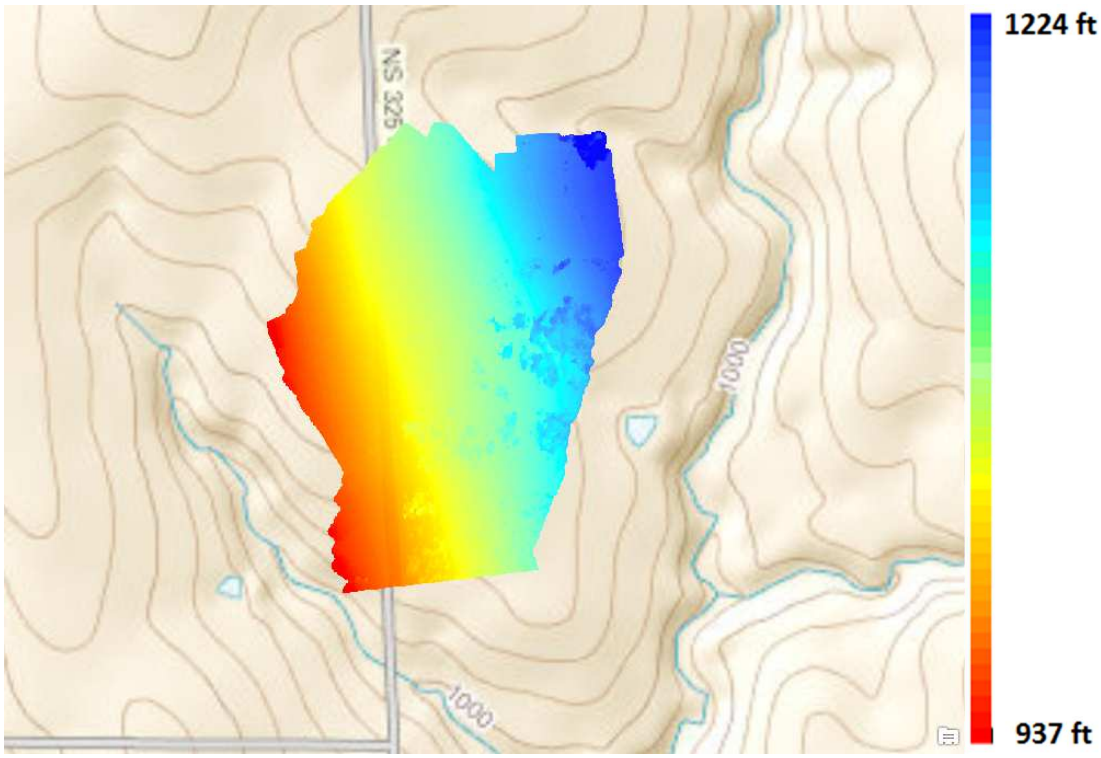

Figure 43 - DEM from the second flight on March 27th.

These images show a disparity in the two DEMs, though the same tall trees seem to appear in both as discontinuities on the south and west sides. It appears that the DEM from the first flight is tilted, giving a much steeper slope than the second flight. Closer examination of the second flight shows that that image is also likely tilted since it shows a downward slope from northeast to southwest, not northwest to southeast. The ground height also appears to change at least 200 ft in the DEM, though the USGS ground truth only shows a change of about 50 feet in the same area. This type of error would be unacceptable for quantitative calculations. Evaluating any improvements from better calibration practices – such as easy to see ground reference points at precisely known locations at the edges of the area of interest – are beyond the scope of this study. These problems would have to be solved before the DEMs could be implimented into GIS compatible products. Volumetric properties might still be available through more complex software from the ArcGIS suite or manually orienting the DEM to the contour map, however the software purchase and programming required are also beyond the scope of this study.

A simple visual analysis shows that the Pix4D point cloud from the second March 27th flight suffers from a similar tilt. This point cloud appears to have a 30 foot upward slope from the northwest corner to the southeast corner, rather than the 20 foot downward slope expected. Fortunately, Pix4D can calculate some useful volumetric characteristics without the need for precise geolocation or even correct orientation, because it can calcuate a volume's base using the relative x,y,and z coordinates of the vertices, not simply the apparent latitude and longitude of the point cloud. Using the "New Volume Object" tool, a box was drawn around each plot, as in the figure below. The boundary around each plot was manually set approximately halfway between adjacent plots, and the boundaries without adjacent plots were set approximately the same distance from the plot as the boundaries with adjacent plots. This arrangement adds from 1-2 meters to the height and width of each plot. For this study the plots are numbered as illustrated below, with the northwest plot being 1, the southeast plot being 14, and the numbers increasing from west to east and then north to south. For example, plot 2 is highlighted in the example below.

Pix4D outputs three variables that may be useful in analyzing the fuel composition of the plot, namely Enclosed 3D Area (meaning using x,y,and z coordinates rather than simply latitude and longitude), Terrain (surface) 3D Area, and Total Volume above the base. They are collected in the following tables, along with when the plot was last burned and other useful information.

(a)  (b)

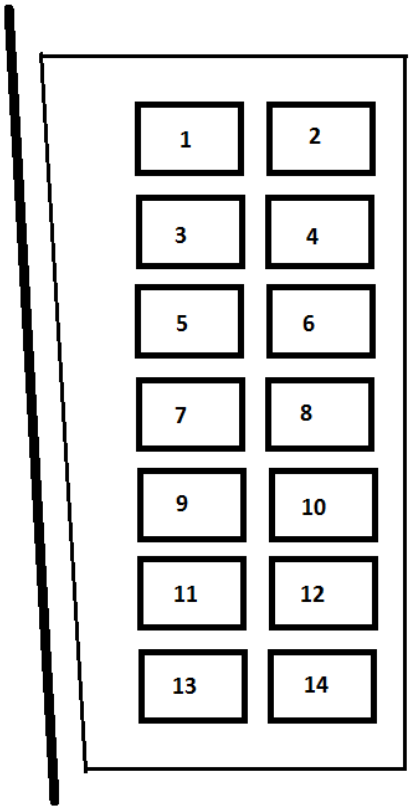

Figure 44 - (a) An example of segmenting a single plot (plot 2), and (b) the plot numbering.

One major source of variation in these measurements is the choice of vertices. The mowed grass between each plot may vary by a few centimeters depending on the exact point chosen and the time since it was last mowed. No consistent methodology was identified to control or measure this variable, and so it remains an unknown in this evaluation. It would primarily influence the precision of volume and vegetation height measurements.

Two ratios were evaluated for their correlation to fuel type and fuel load within a cell. The first is Terrain 3D Area divided by Enclosed 3D Area, which would give a nondimensional indicator of the chaotic nature of the canopy top. The rationale for this variable is the assumption that a canopy full of trees or trees with space between would have a more chaotic surface than a field

full of surface fuels only. Below is a chart of the surface variation observed in each of the 14 plots over the five flights.

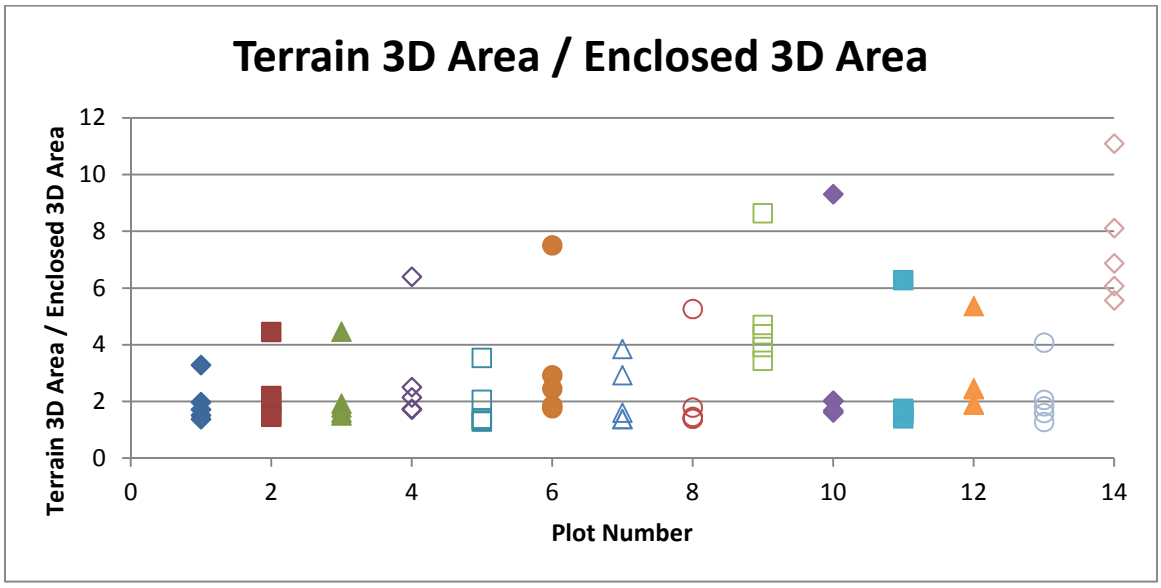

Figure 45 - The calculated surface variation within each plot during each test flight.

The chart illustrates how there seems to be at least one outlier from each plot. Close examination of the data (Appendix D) shows that every plot during the Feb 12th flight resulted in an outlier due to an excessively high Terrain 3D Area. This mosaic was constructed from video data, so there was no geotagging to rectify the mosaic with latitude, longitude, and altitude. As a result, the mosaic was tilted sharply and all lengths were stretched by approximately 50%.

The second ratio was Total Volume divided by Enclosed 3D Area, or average height above the base. If the ground can be identified, than the height of the canopy above it would be a good indicator of the presence of trees or other crown fuels that could be significant carriers of fire in a high intensity wildfire event. The presence of trees could also alter the complex flow of fresh air above an active fire. The following chart shows the surface variation observed in each of the 14 plots over the five flights.

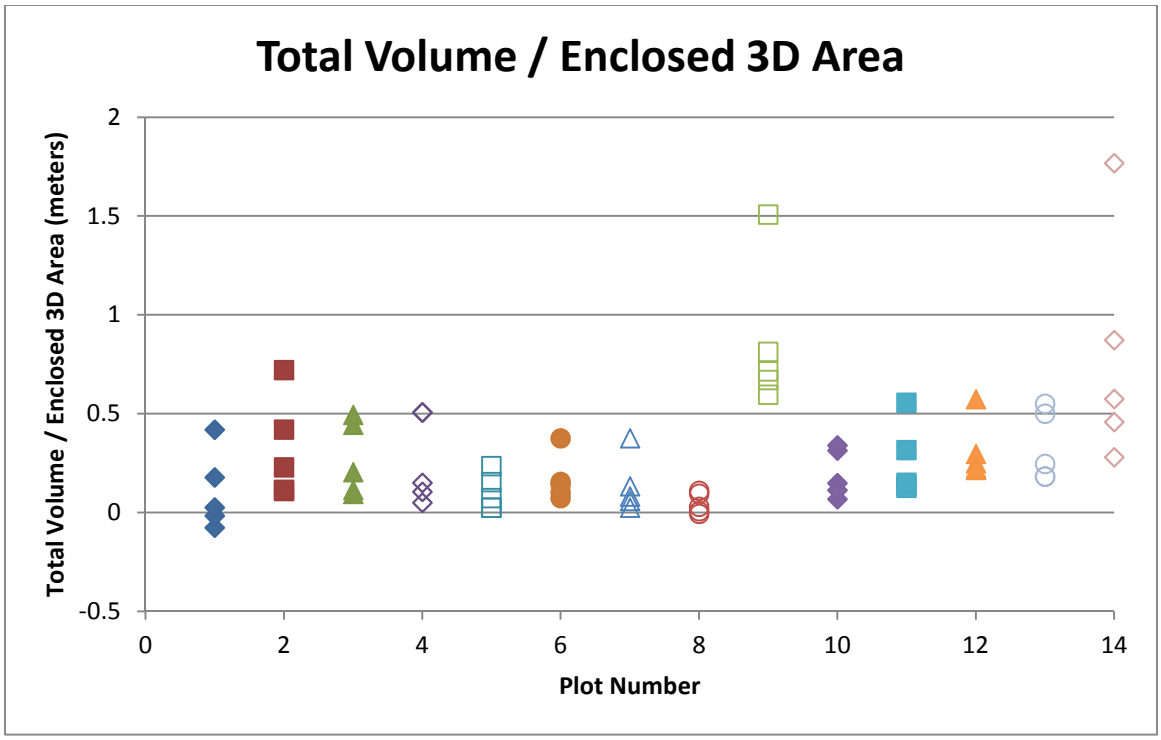

Figure 46 - The Average height within each plot during each test flight.

This chart also shows at least one outlier from each flight. Evaluation of the data shows that this time the Jan 30th flight was a high outlier in every flight, and almost every Feb 12th flight also had an excessively high average height. This phenomenon is likely the result of the length distortion noticed above. As all the lengths are increased, a volume divided by an area is going to increase linearly with them. Because of these outliers, the Jan 30th and Feb 12th flights have been removed from the volumetric evaluation, and future tests should only be conducted using still images which have been tagged with latitude, longitude, and altitude, at a minimum. The following chart shows the two ratios above plotted against eachother for the three flights that meet this criteria.

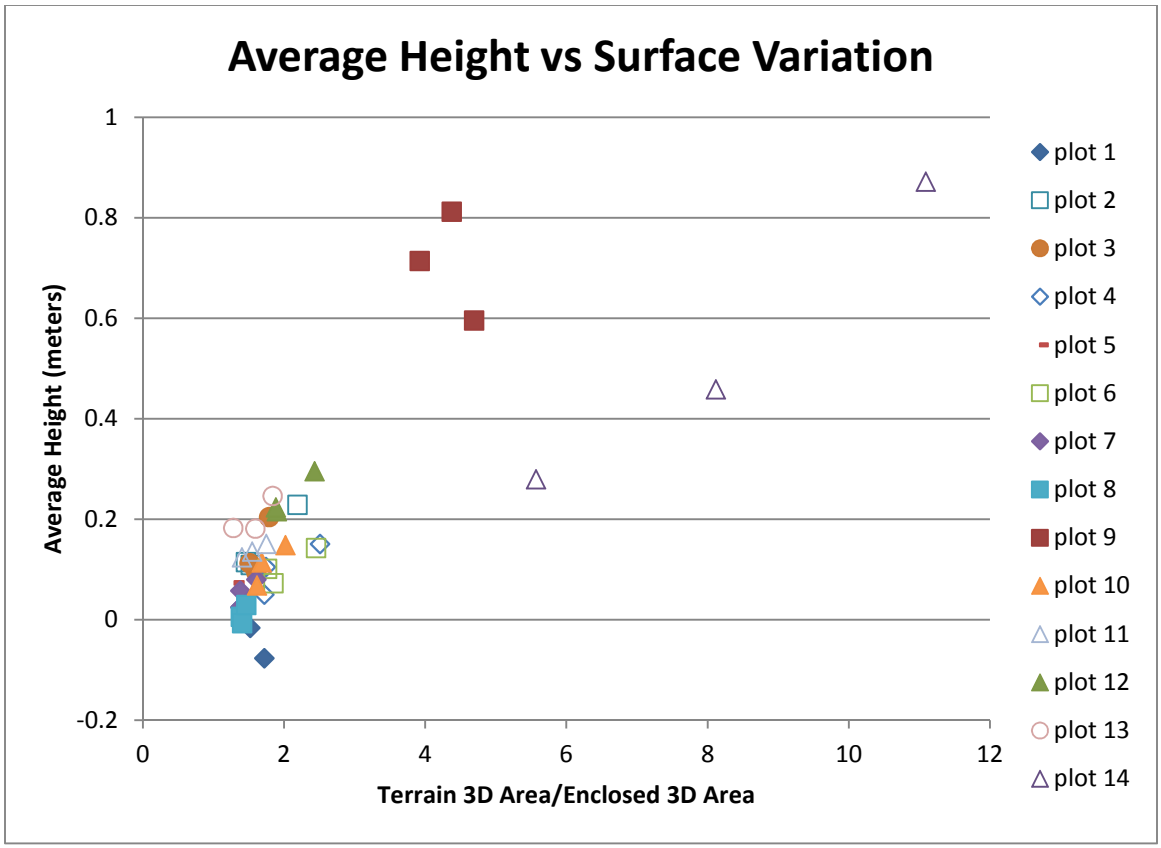

This graph shows a separation of the center of mass of the three plots with trees (plots 9, 12, and 14) from the center of mass of the other plots. Though a sample size of three is hardly convincing evidence, these two variables seem to be strong indicators of the presence of crown fuels within a plot. This evaluation assumes that the ground level can be evaluated, which is not always possible with passive sensors observing a closed canopy from above. In order to extend these results into envoronments with closed canopies, an active sensor like canopy penetrating LiDAR or a separate ground survey and accurate ground reference points must be utilized.

These results appear to show that SfM volumetric outputs could be strong indicators of the presence of canopy fuels within a plot. Unfortunately, there is yet no compreensive study of the accuracy of SfM measurements. Fortunately, the two flights on March 27th – under identical conditions and seperated by mere minutes – can give some insight into the initial error

estimates when using the current methodology. The following table shows the two ratios calculated for each plot for each flight using the three outputs from Pix4D analysis, finds the difference between each pair, and calculates the percent variation of each value from the mean. Note that variation here is half of the difference. All values have been rounded off to four significant digits, because that is the published accuracy of the smallest output.

Plot No.	Terrain 3D Area/Enclosed 3D Area				Total Volume / Enclosed 3D Area (m)			
	First	Second	Difference	Variation	First	Second	Difference	Variation
1	1.521	1.386	0.135	4.64%	-0.01631	0.02596	0.04227	438.01%
2	1.527	1.461	0.066	2.21%	0.1085	0.1142	0.00575	2.58%
3	1.607	1.508	0.099	3.18%	0.09428	0.1127	0.01838	8.88%
4	1.720	1.741	0.021	0.61%	0.04991	0.1049	0.05501	35.53%
5	1.388	1.323	0.065	2.40%	0.02335	0.02459	0.00124	2.59%
6	1.850	1.760	0.090	2.49%	0.07230	0.1010	0.02868	16.55%
7	1.381	1.377	0.004	0.15%	0.02440	0.05739	0.03299	40.34%
8	1.404	1.466	0.062	2.16%	-0.007016	0.02929	0.03631	163.00%
9	4.692	3.922	0.77	8.94%	0.5953	0.7137	0.1184	9.05%
10	1.615	1.684	0.069	2.09%	0.06803	0.1134	0.0454	25.02%
11	1.401	1.746	0.345	10.96%	0.1238	0.1507	0.02697	9.82%
12	1.895	1.884	0.011	0.29%	0.2154	0.2233	0.00793	1.81%
13	1.279	1.593	0.314	10.93%	0.1823	0.1810	0.001262	0.35%
14	8.114	5.566	2.548	18.63%	0.4584	0.2796	0.1788	24.23%

Table 7 - Calculated variation between the normalized Pix4D outputs.

The highest variation noticed in the left columns is 18.63%, with a standard deviation of 7.19%. Therefore, a 10% error is probably a conservative initial estimate of the error of this non-dimensional ratio. The highest variation noticed in the average height is 438.01%, but the smallest is 0.35%. Closer examination shows that the highest variations are on the order of only 2 cm. This variance is almost exclusively a result of the choice of vertices close of the ground, not the actual variance due to errors in the SfM analysis. If ground points are chosen manually from a point cloud, an additional error should be added based on the difficulty of choosing vertices that accurately represent the ground. If canopy penetrating active sensors are used, their error in finding the ground level should likewise be evaluated before height or volumetric characteristics can be accurately interpreted.

These measurements were confirmed using a common feature in all three flights. A white truck was visible in the same location in all flights in March 20th and 27th. The height of the truck was measured in the images by finding the plane defined by three points on the ground around the truck and the perpendicular distance from that plane to a point on the top center of the truck's cab. The following formulas were used:

$$line_{a-b} = (x_b - x_a)i + (y_b - y_a)j + (z_b - z_a)k$$

$$line_{b-c} = (x_c - x_b)i + (y_c - y_b)j + (z_c - b)k$$

$$plane_{abc} = line_{a-b} \times line_{b-c} = \begin{vmatrix} i & j & k \\ x_b - x_a & y_b - y_a & z_b - z_a \\ x_c - x_b & y_c - y_b & z_c - z_b \end{vmatrix} = ax + by + cz + d = 0$$

$$height = \frac{ax_{top} + by_{top} + cz_{top} + d}{\sqrt{a^2 + b^2 + c^2}}$$

where x_a, y_a, and z_a are the x, y, and z coordinates of point a (and, respectively, b and c) on the ground and x_{top}, y_{top}, and z_{top} are the x, y, and z coordinates of the top of the cab. The distance between the axles was also measured using the following formula:

$$length = \sqrt{(x_{front} - x_{rear})^2 + (y_{front} - y_{rear})^2 + (z_{front} - z_{rear})^2}$$

where x_{front}, y_{front}, and z_{front} are the coordinates of a point on the front tire and x_{rear}, y_{rear}, and z_{rear} are the coordinates or an identical point on the rear tire on the same side. The actual height of the truck and distance between the wheels was measured with a measuring tape.

Figure 47 - an example of the available points for measuring the distance between the tires. The identical points on the front and back tires were selected.

	Height (m)	% Error	Length (m)	% Error
Actual	1.651 (65 in)	N/A	3.175 (125 in)	N/A
	1.700354	2.99%	3.293478	3.73%
	1.742197	5.52%	3.507677	10.48%

	1.475936	10.60%	3.148269	0.84%
Mean	1.639495	0.70%	3.316475	4.46%

Table 8 - Structure from Motion errors from Pix4D measurements

This chapter satisfies objectives 2 and 4.

CHAPTER V

CONCLUSION

1. RECOMMENDATIONS

A UAS is capable of surveying a large area with visual and infrared sensors in order to determine variations in fuel type, load, and condition. NIR and color information can be combined to calculate a "greenness" index that can indicate the fire danger within small fuel cells when compared with historical information. Infrared reflectance information could also be used for broad fuel type classification, or potentially region-specific species identification using machine learning techniques. The test results show that SfM volumetric outputs can also give strong indications of the presence of crown fuels within small (600 m^2 in the experiment) cell. This process could give a fast estimate of the location of isolated trees and other fuels far from the surface which could influence the effectiveness of a flame spread model. This information can then be turned into a GIS compatible fuel map that can be combined with ground slope and weather information to create a very fine scale fire danger map for implementation of effective fire prevention measures.

A small instrumented UAS also has the ability to perform several tasks that would make firefighters more effective and efficient at observing and containing wildland fires. LWIR spectral information, when combined with color information for scene identification, can be extremely effective at locating hot spots that could indicate a fire line, a new spot fire, or humans

and animals that are in harm's way. Aerial surveys of a recently burned area could be used to confirm or disprove the presence of surface or subsurface fires that could flare up into new fires if not extinguished. Finally, video smoke detection provides the possibility of discovering new fires autonomously at great distances and around obstacles that would obscure ground observation.

2. OBJECTIVES

The first objective of this paper was to determine the specific situational awareness needs of an incident commander responding to a wildfire that can be solved using image processing techniques. This objective was completed by interviews with firefighters and fire trainers at Oklahoma State University, Stillwater, OK municipal fire department, and various other fire departments across Oklahoma. An incident commander needs information related to where the fire is and where it is going. He also needs to know where his firefighting resources are to ensure they are where he wants them. Topographic hazards, natural fire breaks, and any nearby wildland-urban interface are also critical for the placement and maneuver of resources.

Category	Specific Need	Small UAS solution
Resources	Location of Resources	Visual beacons on vehicles and firefighters
	Communication	Extend line-of-sight radio range with airborne repeater
Terrain	Hazards	GIS hazard overlay on incident commander's electronic maps
	Natural Fire Breaks	GIS overlay of roads, water, and recognized bare soil
Fire	Fire Location	Smoke and Fire detection
	Fire behavior	Fuel maps for predictive models
Fire Danger	Fuels	Fuel maps from regular SfM surveys

	Ground Slopes Weather	SfM or LiDAR DEM of ground level Wind estimates in flight at various altitudes
High Risk Areas	Wildland Urban Interface Dangerous Fuels	Manual or semi-autonomous recognition from regular surveys Fuel maps of type, density, height, and moisture content

Table 9 - Situational Awareness needs of an incident commander that can be addressed by a small UAS with image processing capability

The second objective was to evaluate the capabilities of image processing to increase an incident commander's situational awareness. Autonomous flame detection from color video was evaluated, but it was found to be much less effective than thermal infrared sensors currently used. Autonomous smoke detection was evaluated, and showed some real promise with a down-facing, zero distortion camera. Optical flow discontinuity and wavelet transforms were the most effective of the techniques tested. bNDVI maps were created from georeferenced mosaics and volumetric analysis was evaluated using SfM point clouds, but a full evaluation of fuel load mapping was not completed because it would require creating a history of values for each plot.

Plant identification using multispectral sensors was investigated under the second objective, and SfM programs gave some strong indicators which could determine whether a plot contained trees, tall shrubs, or only surface fuels. Spectral analysis of plant type would also require historical values to delineate annuals versus perennials or evergreen versus deciduous trees.

The third objective was to evaluate multiple UAS platforms in order to determine the best one for firefighting. The DJI Phantom was evaluated extensively for usefulness in this study. The short flight time and small payload capacity would limit this aircraft from use in fighting active wildfires. Larger hexcopter platforms were identified for this study, but unsuccessful test flights prevented information gathering flights in the field. A successful firefighting UAS would require some onboard processing and ground communication capability to provide the incident commander with useful information in real time. Additionally, range should be increased through the use of a first person view camera and semi-autonomous waypoint navigation.

The fourth objective was to evaluate the effectiveness of information gained through various sensors when applied to firefighting. The GoPro camera and the modified NIR/G/B camera were evaluated for use in fire spotting. GoPro imagery is difficult to use for optical flow calculations because of its fish-eye distortion. Though NIR was shown to be a weak indicator of the presence of a smoke plume, information from the NIR/G/B camera was useful for identifying smoke when it was pointed down. A LiDAR active sensor is identified below as a potential sensor for determining ground height for fuel mapping, though it was not evaluated specifically in this paper.

The fifth objective was to evaluate Commercial-Off-The-Shelf (COTS) products for their usefulness. Several commercial-off-the-shelf platforms and sensors would be appropriate for firefighting or fuel mapping purposes. An industry SfM survey product designed for similar work was quoted at $30,000, including equipment, training, and software. A cost this low or lower should be a requirement for a product marketed to a volunteer fire department.

The final objective was to evaluate the minimum crew requirement for a wildfire UAS by determining the amount of information that could be gained by a single operator UAS. A single operator system could be useful for firefighting or fuel mapping given a sufficient degree of onboard processing or post processing is acceptable. Current FAA rules require visual line of sight between the operator or an observer and the UAS during the entire flight, but single-operator control is practical for the short ranges required by a firefighting or fuel mapping mission.

3. PLATFORMS

A larger platform with more endurance and payload capacity will be needed to expand on these experiments. The current platform, a DJI Phantom, lacks the ground clearance or lifting capacity to carry more than one sensor at a time, or to protect that sensor from foreign object damage (FOD) in harsh environments. Another DJI platform, the S900 folding arm hexcopter, is being developed for subsequent tests. This platform would have the ability to carry more than one sensor and the ground clearance to mount sensors to a stabilized gimbal. It will also have the lifting capacity to carry more than one battery, potentially increasing the flight time significantly.

4. SENSORS

Color cameras like the GoPro could potentially be used for autonomous smoke detection, which would give firefighters an early warning of fire without a direct human observer. This paper shows the ineffectiveness of many techniques that attempt to detect smoke within a single frame. Current video smoke detection programs require the observation of a scene over time, with minimum camera ego-motion. The low endurance and constant motion of a hovering UAS prevents continuous monitoring of a specific scene, and therefore eliminates many effective smoke detection techniques developed for use in fire towers. Gimbal stabilization and optical flow show some potential for minimizing camera ego-motion so that more effective techniques can be tested. Down-facing video also provides some potential for smoke detection by finding discontinuities in the optical flow.

The Canon SX260 HS, modified to provide interval NIR/G/B imagery, performed very well in gathering imagery for SfM mapping. NIR imagery identified stark differences in reflectance characteristics of different trees within the plot, which did not appear in color imagery. This information could be used by land managers for fuel type classification (i.e. annuals versus perennials, deciduous versus evergreen trees) when comparing 12-month historical imagery. bNDVI observations compared to satellite imagery were inconclusive, but this disagreement was expected given the difference in plot sizes, spectral bands, bandwidths, and time of acquisition. The tests do confirm that detailed bNDVI maps can be produced from imagery taken by this camera; however much more detailed analysis of the effects of the previous variables is required before this information could be used for actual fire danger. Potentially, historical bNDVI surveys could be used to produce very high resolution fire danger maps similar to the process EROS uses to convert NDVI observations into nation-wide "relative greenness" maps.

The modified Canon SX260 HS NIR/G/B camera performed well in the absence of large vibrations, however at high power settings the camera's internal clock would malfunction, causing the interval picture process to fail. This phenomenon was not noticed in any of the tests after the operator was notified of the problem and became more intentional about reducing abrupt control inputs. The importance of avoiding abrupt maneuvers should be communicated to operators of VTOL platforms in all future tests.

The LWIR sensor evaluated suffered from lack of reliable temperature information and loss of situational awareness when landmarks were not identifiable in the scene. A small FOV camera like this could potentially be used for identifying firelines, spot fires, and humans and animals during observation, containment, and mopping-up operations, assuming an accurate calibration of the camera and other situational awareness information (i.e. GPS position and/or color imagery) is also used.

As infrared sensors become smaller and cheaper in the future, UAS mounted sensors like this are only going to become more effective at sensing fire, smoke, and fuel conditions. A promising sensor for future tests is the FLIR ONE, an IPhone or Android phone-mounted multispectral sensor. This sensor weighs just 110 grams, and contains both a Lepton thermal imager for reading temperatures between 0-100^{o} C and a color camera. [FLIR] This sensor could gather color information for a SfM analysis and visible reflectance measurements during the day and at the same time identify hot spots on the ground. A similar infrared-only smartphone camera, Seek Thermal, advertises a temperature detection range of -40-300^{o} C. [Seek Thermal] Calibrated thermal infrared cameras like these, when coupled with smartphone GPS and orientation information, could potentially produce highly-detailed GIS compatible thermal maps for use in wildfire fighting, observation, and mopping-up operations.

A gimbal mount which could maintain a nadir orientation at all times would improve the photogrammetry measurements, especially at the edges of the search area where the aircraft would be in steep banking turns. No COTS gimbals are designed for cameras like the Canon SX260 HS; however several gimbals are available for carrying various GoPro cameras on aircraft, especially underneath multirotor UAS. Gimbal-stabilized GoPro color cameras should be utilized for future testing of color smoke detection techniques of hovering aircraft. As more ego-motion of the camera is removed from the video, smoke detection algorithms should produce more conclusive results with fewer false positives.

5. GROUND CONTROL

Ground control, other than manual aircraft control by visual line of sight though a hand-held transmitter controller, was not evaluated in this study. A more complex ground control system

would be required to increase the operating range substantially beyond the 500 meters observed in the test flights. Some improvements in the ground control would include autonomous flight of preprogrammed waypoints, First Person View (FPV) video transmitted to the pilot in flight, and an On Screen Display (OSD) that can give the pilot information critical to safe flight. Current FAA rules require the operator of an observer to be within visible line-of-sight of the aircraft at all times, and flight tests with the DJI Phantom show that the maximum range for line-of-sight control in the presence of smoke is 500 m. Therefore, observers (i.e. firefighters) should be spaced throughout the flight area at no more than 1 km intervals, as the following diagram illustrates.

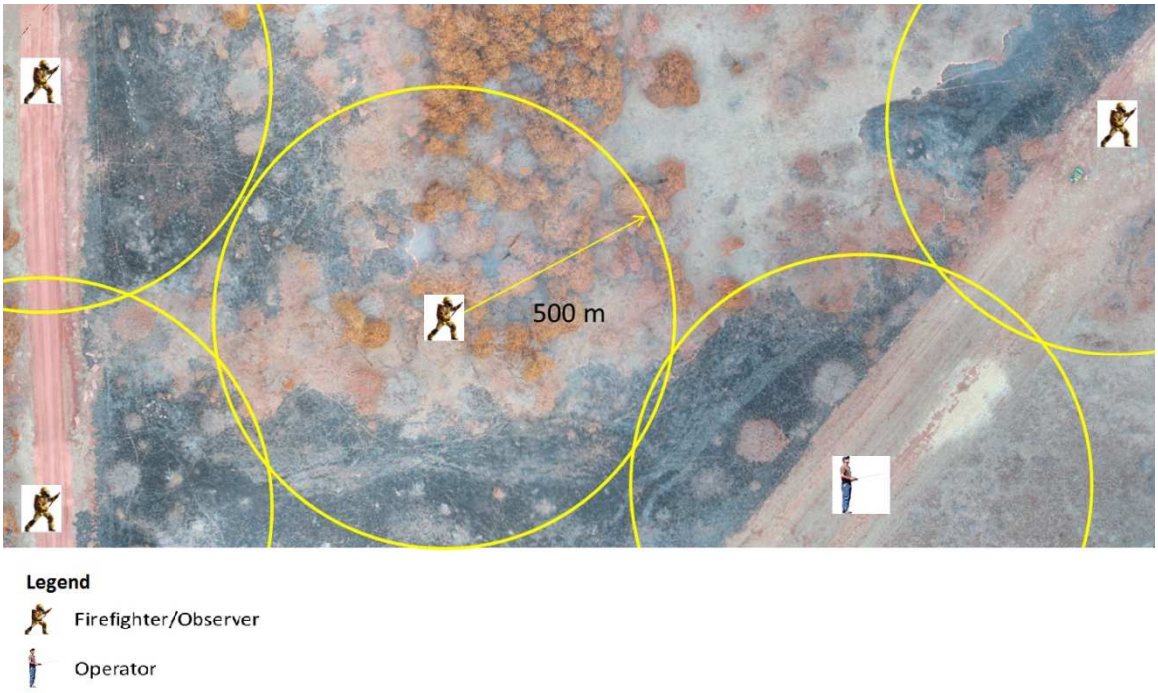

Figure 48 - The maximum range between observers when using a small VTOL UAS at an active burn.

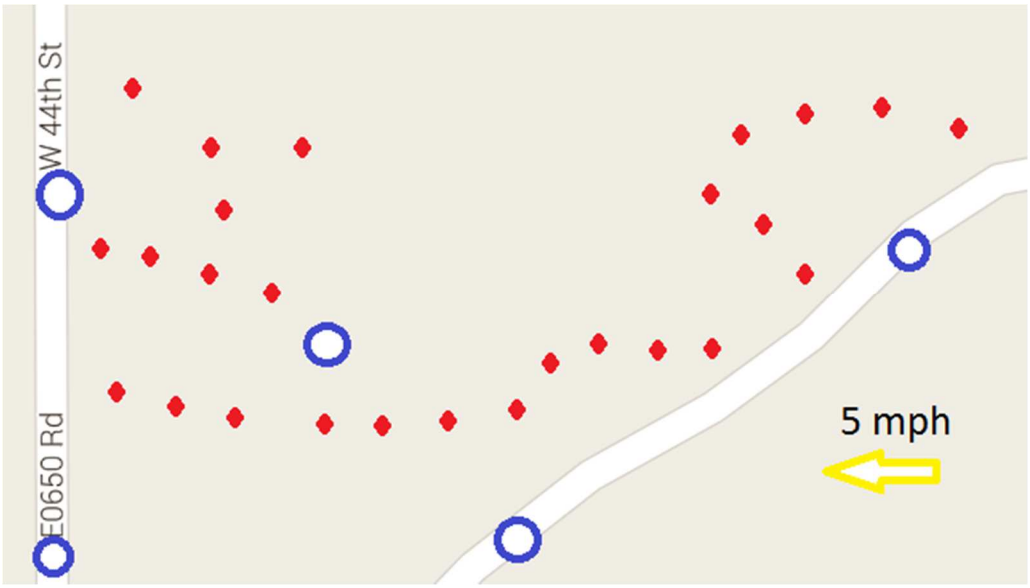

Figure 49 - Example map overlay provided to the incident commander during a controlled burn

The observations of the last three sections satisfy objective 3.

6. ALGORITHMS

The smoke detection algorithms tested had very little success when applied to imagery taken from a UAS platform. Techniques for detecting smoke in a single image produce an excessive number of false positives, and most of the techniques for video stoke detection break down in the presence of significant ego-motion of the camera. One technique that shows significant potential is applying optical flow to a down-facing camera with no distortion (pinhole camera). Because the Phantom is designed to maintain a magnetic heading in flight, there is very little rotation in down facing video except in a turn. This condition results in nearly constant optical flow results across all pixels in the image. If the aircraft flies over a smoke plume, the movement of the smoke creates a large discontinuity in the otherwise continuous flow field. Taking the Laplacian of the flow field will highlight the discontinuity, allowing for autonomous detection of smoke in a

color video. More work is required to evaluate the discontinuities found by moving rigid objects, moving people, or wind-blown objects in order to validate the technique.

SfM analysis was able to produce very high resolution, georeferenced mosaics for input into GIS. The spatial accuracy of these mosaics cannot currently be verified, and significant rotation was found in DEMs produced by geotagged imagery input into Agisoft Photoscan. Without ground reference points, these DEMs will be unusable for volumetric analysis, and even with ground reference points the interpolation errors cannot currently be verified. However, chromatic analysis of a manually oriented photomosaic in a program like MATLAB can produce non-georeferenced NDVI or color fuel maps that could be compared qualitatively.

7. FUTURE WORK

This study has found a number of roadblocks to progress that need to be addressed before a reliable tool can be put in the hands of the end user. Passive sensors, such as color or infrared imagery, are limited to observing the vegetation canopy only. They are unable to find the ground through the vegetation. If accurate height or volume assessments are desired then some type of active sensor needs to be used as well. One solution to this problem comes from canopy penetrating LiDAR. These devices act as laser rangefinders which use the aircraft position and attitude and the direction to the target to find the exact location of the target in three dimensions.

Figure 50 - the PulsedLight mini LiDAR device

The device above is an example of a short range LiDAR device designed for small UAS. In order to find the ground, the system would have to filter out any reflections off of canopy or surface fuels and only keep the reflections from the ground. The information from the LiDAR would need to be timed with position and orientation information in order to calculate a DEM. Calibration with objects of known distance and a comparison with SfM calculations would also be needed to ensure the DEM is at least as reliable as the DEM produced by SfM. If possible, the LiDAR and the camera need to get their position and orientation information from the same source in order to minimize the errors associated with GPS and inertial sensors. Finally, the corrections to camera position and orientation applied by the SfM program will also need to be applied to the LiDAR information, if significant. If successful, the LiDAR data could potentially increase the accuracy of fire spread models by determining local ground slopes and combining with SfM point clouds to directly measure certain canopy characteristics.

More work is required to correlate NDVI (or bNDVI) measurements from an aircraft sensor to actual fire danger analysis. During this process, the investigators should research the ongoing OKFIRE update, since the OKFIRE administrators are currently evaluating MODIS imagery as a higher-resolution alternative to the AVHRR imagery currently being used. Additionally, the effects of illumination levels and angles should be evaluated so a consistent methodology can be applied to correct for these differences, if necessary.

Another method for evaluating fire risk would be to compare current measurements of a well-defined plot to historic evaluations, similar to the way EROS produces their weekly "relative greenness" maps. Because the mosaics are being produced by imagery with spatial resolutions on the order of centimeters, they could generate a fuel map with any practically small cell size. However, more analysis would be needed to determine the true spatial accuracy of SfM over a variety of conditions before super-high-resolution fuel maps could be compared to determine historic trends. Alternatively, fuel cells delineated by permanent ground reference points could be used to confirm the accuracy of high resolution fire danger maps without determining the exact errors in SfM spatial analysis. Flights performed at different times of the day and different times of the year could be normalized over time using weekly EROS greenness readings and compared to each other.

Flights in the vicinity of prescribed grass fires have shown the potential of SfM mosaics for post-burn and post-disaster assessment. For instance, this mosaic was produced from images taken during mopping-up operations after a 60-acre grass fire. The image shows clearly the extent of the burn and the position of the fireline. Coupling camera locations and orientations with thermal infrared information could give firefighters exact locations and intensities of local hot spots to extinguish.

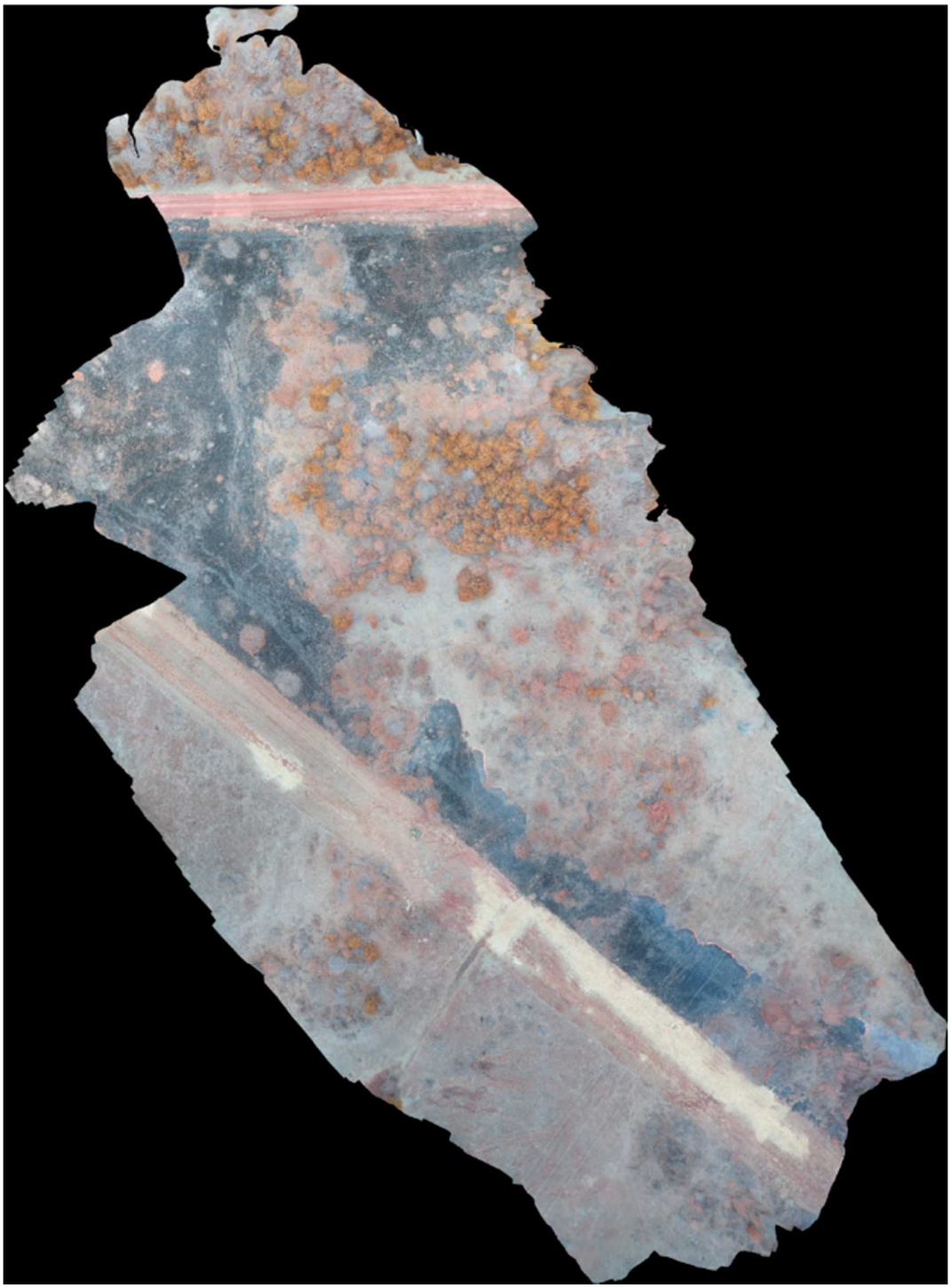

Figure 51 - Mosaic produced from imagery taken during mopping-up operations after a prescribed grass fire.

Similar mosaics were produced during a 2000 acre prescribed grass fire. The first image is a mosaic of images from the first flight, before the fire spread into the area of interest. The second image is a mosaic of images from all three flights, illustrating the extent of the fire spread in approximately 20 minutes. Future research should look into methods of producing mosaics like these over large areas quickly, in order to aid firefighters in locating and containing rapidly spreading firelines.

(a) 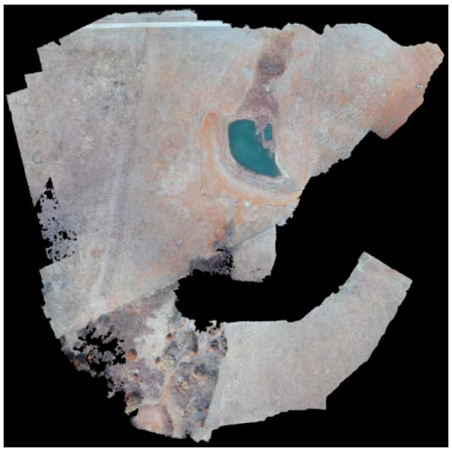 (b) 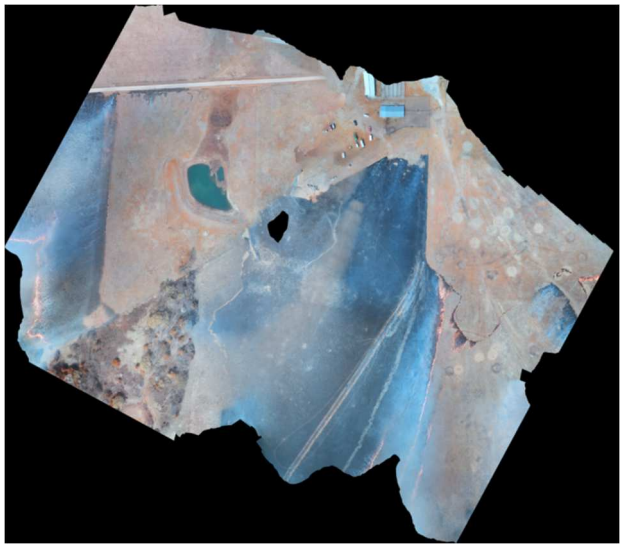

Figure 52 - Mosaics of (a) single image set and (b) all three image sets at a controlled burn.

REFERENCES

AirGon "AirGon Presents Small UAS Metric Mapping Workflows," online webinar, March 4, 2015.

Ambrosia, V. G., Wegener, S., Zajkowski, T., Sullivan, D. V., Buechel,S., Enomoto, F., Lobitz, B., Johan, S., Brass, J., Hinkley, E., "The Ikhana Unmanned Airborne System (UAS) Western States Fire Imaging Mission: From Concept to Reality (2006-2010)," *Geocarto International*, Vol. 26, No. 2, pp. 85-101, April 2011.

Blair, J. B., Rabine, D. L., Hoftman, M. A., "The Laser Vegetation Imaging Sensor: A Medium-Altitude, Digitization-Only, Airborne Laser Altimeter for Mapping Vegetation and Topography," *ISPRS Journal of Photogrammetry and Remote Sensing*, Vol 54, pp 115-122, 1999.

Bruce D., "Drones on the Fire Ground – Australia Update," *Wildfire*, Jan/Feb 2015, http://www.wildfiremagazine.org/

Bradley, T., conversation with author, June 30, 2014.

Burgan, R. E., Hartford, R. A., Eidenshink, J. C., "Using NDVI to Assess Departure From Average Greenness and its Relation to Fire Business," General Technical Report INT-GTR-333, Ogden, UT, U.S. Department of Agriculture, Forest Service, Intermountain Research Station, 1996.

Carlson, J. D., conversation with author, June 15, 2014.

Carlson, J. D., email to author, March 19, 2015.

Carlson, J. D., Burgan, R. E., "Review of Users' Needs in Operational Fire Danger Estimation: the Oklahoma Example," *International Journal of Remote Sensing*, Vol. 24, No. 8, pp. 1601-1620, 2003.

Carlson, J. D., Burgan, R. E., Engle, D. M., Greenfiels, J. R., "The Oklahoma Fire Danger Model: An Operational Tool for Mesoscale Fire Danger Rating in Oklahoma," *International Journal of Wildland Fires*, Vol 11, pp. 183-191, 2002.

Carlson, J. D., Coen J., "Weather Environments for UAVs in Wildfire Situations," UAV *Workshop,* June 2014, Oklahoma City, OK.

Celik, T., Demirel, H., Ozkaramanli, H., Uyguroglu, M., "Fire detection using statistical color model in video sequences," *Journal of Visual Communication and Image Representation*, Vol 18, Issue 2, pp. 176-185, April 2007.

Çengel, Y. A., *Heat and Mass Transfer: A Practical Approach*, Third Edition, McGraw-Hill, pp. 710-711, 2007.

Chen, L., Wang, Y., Tian, Y., Huang, T., "Wavelet Based Smoke Detection Method with RGB Contrast-Image and Shape Constraint," *2013 Visual Communications and Image Processing (CVIP)*, IEEE, Kuching, Malaysia, 2013.

Chen, T. H., Wu, P. H., Chiou, Y. C., "An Early Fire-Detection Method Based on Image Processing," 2004 International Conference on Image Processing (ICIP), 2004.

Chen, T. H., Yin, Y. H., Huang, S. F, "The Smoke Detection for Early Fire-Alarm Systems Based on Video Processing," *IEEE 2006 International Conference on Intelligent Information Hiding and Multimedia Signal Processing (IIHMSP)*, pp. 427-430, 2006.

Christensen, N. L., Agee, J. K., Brussard, P. F., Hughes, J., Knight, D. H., Minshall, G. W., Peek, J. M., Pyne, S. J., Swanson, F. J., Thomas, J. W., Wells, S., Williams, S. E., Wright, H. A., "Interpretting the Yellowstone Fires of 1988: Ecosystem response and management implications," *Bioscience*, Vol. 39, No. 10, pp. 678-685, 1989.

Damir, K., Darko, S., Toni, J., "Histogram-Based Smoke Segmentation in Forest Fire Detection Systems," *Information Technology and Control*, Vol. 38, No. 3, pp. 237-244, 2009.

Davenport, T. M., "Early Forest Fire Detection Using Texture Analysis of Principal Components from Multispectral Video," M.S. Thesis, Electrical Engineering Dept., California Polytechnic State University, San Luis Obispo, CA, 2012.

Dawson-Howe, K., *A Practical Introduction to Computer Vision with OpenCV*, Wiley & Sons, 2014.

Event38, http://www.event38.com/ProductDetails.asp?ProductCode=CAM-NGB260, accessed March 2015.

FLIR, http://flir.com/flirone/, accessed April 4, 2015.

Fonstad, M. A., Dietrich, J. T., Courville, B. C., Jensen, J. L., Carbonneau, P. E., "Topographic Structure From Motion: a New Development in Photogrammetric Measurement," Earth Surface Process Landforms, Vol 38, pp. 421-430, 2013.

Gabbert, B., "2012: Third highest number of wildfire acres burned," *Wildfire Today*, Nov 23, 2012, http://wildfiretoday.com/, accessed Feb 2015.

Grossman, L., "Drone Home," *TIME Magazine*, http://content.time.com/time/magazine/article/0,9171,2135132,00.html, Feb. 11, 2013, accessed April 13, 2015.

Gubbi, J., Marusic, S., Palaniswami, M., "Smoke Detection in Video Using Wavelets and Support Vector Machines," *Fire Safety Journal*, Vol. 44, pp. 1110-1115, 2009.

Henry A. Wright, "Role of Fire in the Management of Southwestern Ecosystems," Effects of Fire Management of Southwestern Natural Resources, Proceedings of the symposium, November 1988, Tucson, AZ, USA.

Hill, M. S., "Field Report: A Pilot Use of Unmanned Aircraft Systems (UAS) for 2014 Wildfires," *Wildfire*, Jan/Feb 2015, http://www.wildfiremagazine.org/

Hill, R., conversation with author, July 18, 2014.

Horn, B. K. P., Schunck, B. G., "Determining Optical Flow," *Artificial Intelligence*, Vol. 17, pp. 185-203, 198.

Hornby, L. G., "Fuel Type Mapping in Region One," *Journal of Forestry*, Vol. 66, No. 1, pp. 67-72, 1935.

Iriarte, J., "Using UAV LIDAR and Spectral Technology to Detect Human Landscape Changes in Amazonia," AAAS 2015 Annual Meeting, San Jose, CA, USA, Feb 13, 2015.

Kurtley, E., conversation with author, July 1, 2014.

OKFIRE, ***http://okfire.mesonet.org/***, last accessed April 1, 2015.

Loveland, T. R., Merchant, J. W., Ohlen, D. O., Brown, J. F., "Development of a Land-Cover Characteristics Database for the Conterminous U.S." *Photogrammetric Engineering and Remote Sensing*, Vol. 57, No. 11, pp. 1453-1463, 1991.

Mathews, A. J., Jenson, J. L. R., "Visualizing and Quantifying Vineyard Canopy LAI Using an Unmanned Aerial Vehicle (UAV) Collected High Density Structure From Motion Point Cloud," *Remote Sensing*, Vol. 5, pp. 2164-2183, 2013.

Matthews, S., Sullivan, A., Gould, J., Hurley, R., Ellis, P., Larmour, J., "Field Evaluation of Two Image-Based Wildland Fire Detection Systems," *Fire Safety Journal*, Vol. 47, 2012, pp. 54-61.

Mitchel, T., "Detecting Atmospheric CO2 Plumes Using Unmanned Aircraft," Presentation at Oklahoma State University, Feb 2015.

McCree, K. J., "The Action Spectrum, Absorptance and Quantum Yield of Photosynthesis in Crop Plants," *Agricultural Meteorology*, Vol. 9, pp 191-216, 1972.

Murphy, R. R., *Disaster Robotics*, MIT Press, 2014.

NASA Armstrong, "An Earth Science Aircraft for the 21st Century," NASA Armstrong Fact Sheet: Altair, July 8, 2014.

Ojo, J. A., Oladosu, J. A., "Video-based Smoke Detection Algorithms: A Chronological Survey," *Computer Engineering and Intelligent Systems*, Vol. 5, No. 7, pp. 38-50, 2014.

Okamoto, H., Murata, T., Kataoka, T., Hatam S., "Plant Classification for Weed Detection Using Hyperspectral Imaging with Wavelet Analysis," *Weed Biology and Management*, Vol. 7, No. 1, pp. 31-37, 2007.

Poulos, H. M., "Mapping Fuels in the Chihuahuan Desert Borderlands Using Remote Sensing, Geographic Information Systems, and BioPhysical Modeling," *Canadian Journal of Forestry Reseearch*, Vol. 39, pp. 1917-1927, 2009.

Reed, C., Metcalf, P., Louthan, J., conversation with author, July 3, 2014.

Rouse, J. W., Haas, R. H., Schell, J. A., Deering, D. W., "Monitoring Vegetation Systems in the Great Plains with ERTS," *Third ERTS Symposium*, NASA SP-351, pp. 309-317, 1973.

Running, S. W., Loveland, T. R., Pierce, L. L., Nemani, R. R., Hunt, E. R., "A Remote Sensing Based Vegitiation Classification Logic for Global Land Cover Analysis," *Remote Sensing of Environment*, Vol. 51, No. 1, pp. 39-48, 1995.

Saatchi, S., Halliga, K., Despain, D. G., Crabtree, R. L., "Estimation of Forest Fuel Load from Radar Remote Sensing," *IEEE Transactions on Geoscience and Remote Sensing*, Vol. 45, No. 6, 2007.

Schmidt, I. T., "Use of Ultra-High Resolution Imagery in the Estimation of Wildfire Fuel Load Across Chaparral Vegetation," M.S. Thesis, Department of Geography, San Diego State University, San Diego, CA, 2014.

Seek Thermal, http://www.thermal.com/thermal-cameras/, accessed April 9, 2015.

Snavely, N., Seitz, S. M., Szeliski, R., "Skeletal Graphs for Efficient Structure From Motion," *CVPR*, Vol. 1, 2008.

South Carolina Forestry Commission (SFCS), "Fuel Load Estimation Guide for South Carolina," *Smoke Management Guidelines for Vegetative Debris Burning Operations in the State of South Carolina*, July 2014.

Sun, D., Roth, S., Black, M. J., "Secrets of Optical Flow Estimation and Their Principles," I*EEE Conference on Computer Vision and Pattern Recognition (CVPR),* 2010.

Sun, D., Roth, S., Black, M. J., "A Quantitative Analysis of Current Practices in Optical Flow Estimation and the Principles Behind Them," Technical Report, Brown-CS-10-03, 2010.

Toreyin, B. U., Yigithan D., and Enis, C., "Wavelet Based Real-Time Smoke Detection in Video," *European Signal Processing Conference*, EURASIP, Poznań, Poland, 2005.

Tucker, C. J., "Red and Photographic Infrared Linear Combinations for Monitoring Vegetation," *Remote Sensing of Environment*, 8, No. 2, pp. 127-150, 1979.

US Geological Survey, *http://ned.usgs.gov/,* National Elevation Dataset, accessed April 1, 2015.

Wang, N., Zhang, N., Dowell, F. E., Sun, Y., Peterson, D. E., "Design of an Optical Weed Sensor using Plant Spectral Characteristics," *Transactions of the ASAE*, Vol. 44, No. 2, pp. 409-419, 2001.

Wang, S., He, Y., Zou, J. J., Zhou, D., and Want, J., "Early Smoke Detection in Video Using Swaying and Diffusion Feature," *Journal of Intelligent and Fuzzy Systems*, Vol. 26, 2014, pp. 267-275.

Wildland Fire Management RD&A, "Annual Report: FY2013," on behalf of the National Fire Decision Support Center, December 2013.

Yoon, S. H., Min, J., "An Intelligent Automatic Early Detection System of Forest Fire Smoke Signatures using Gaussian Mixture Model," J Inf Process Syst, Vol 9, No 4, pp 621-632, December 2013.

Yuan, F. "A fast accululative motion orientation model based on integral image for video smoke detection," *pattern recognition letters,* vol. 29, no. 7, pp. 925-932, May 2008.

APPENDIX A

CONSTANT ARC LENGTH CAMERA

High-altitude airborne and satellite volume sensors (like calibrated cameras or multi- or hyperspectral sensors) often give their resolution in degrees or radians rather than in width and height at a certain focal length. Taken literally, this definition of field of view by an arc length would produce the type of distortion commonly referred to as "fish-eye effect." Since the GoPro camera produces a similar distortion effect, this appendix will investigate the advantages or disadvantages of this type of representation and whether the GoPro imagery would be useful for certain wildfire missions.

As stated in Chapter 3, the fish-eye effect of a GoPro would not be appropriate for creating a stitched photomosaic or a Structure from Motion point cloud from nadir images because of the nonlinear distortion, but it may have some uses where certain types of distortion would be preferable to a pinhole camera. In the pinhole camera model, an undistorted image of a 3-D world is projected onto a 2-D focal plane, giving the appearance of something like the center of a human eye's field of view.

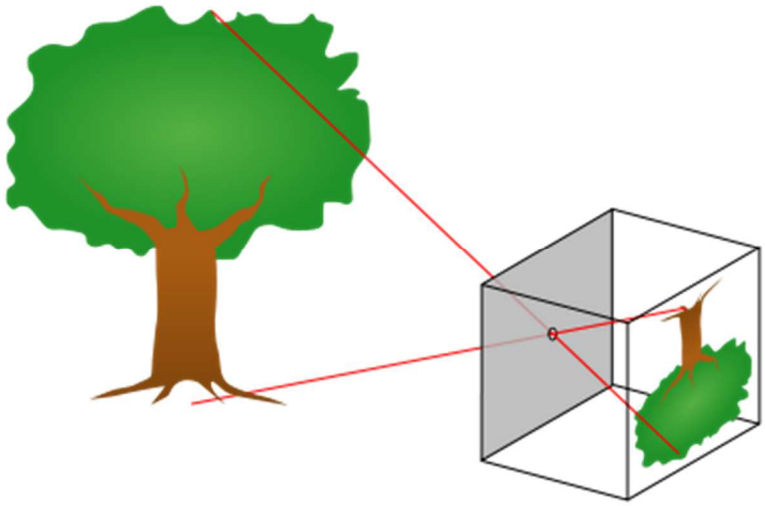

Figure 53 - A simple pinhole camera, [Wikipedia.org]

If a camera followed a different model, where a pixel swept out a certain angle of space rather than a distance in the focal plane, then it could more effectively portray very wide fields of view – even 360º panoramas – easily. This model would curve the focal plane so that it is an equal distance from the camera at every point. This effect is essentially the same as combining the center pixels of several pinhole cameras at different orientations.

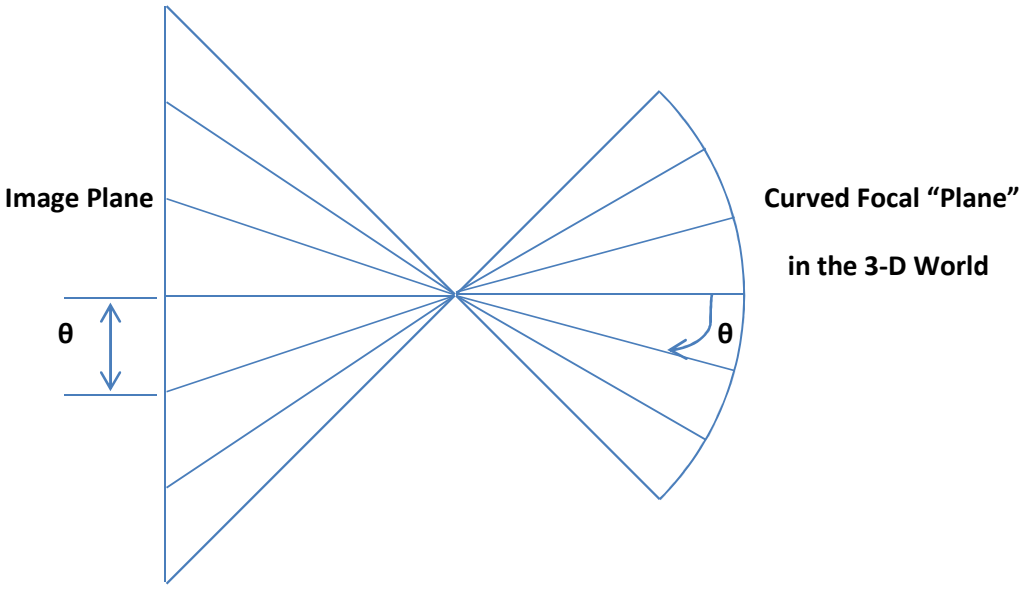

Figure 54 - a representation of the distortion apparent with a constant arc length camera.

There may be two distinct advantages to this approach, from an image processing point of view. First, if a constant arc length camera is rotated in-plane (pitch or roll, if the x axis is perpendicular to the center of the focal plane); the image is simply translated vertically or laterally, with no other distortion. See the simulations below for a demonstration of a constant arc length camera looking forward and down (45°) at a square grid mat from 4 inches above the mat. As the camera is rotates in pitch or roll, the lines would not change shape. They would simply translate up, down, left, or right. If a pinhole camera was used to create a panorama it would have to distort each image to match each adjacent image, and the result would be similar to this model.

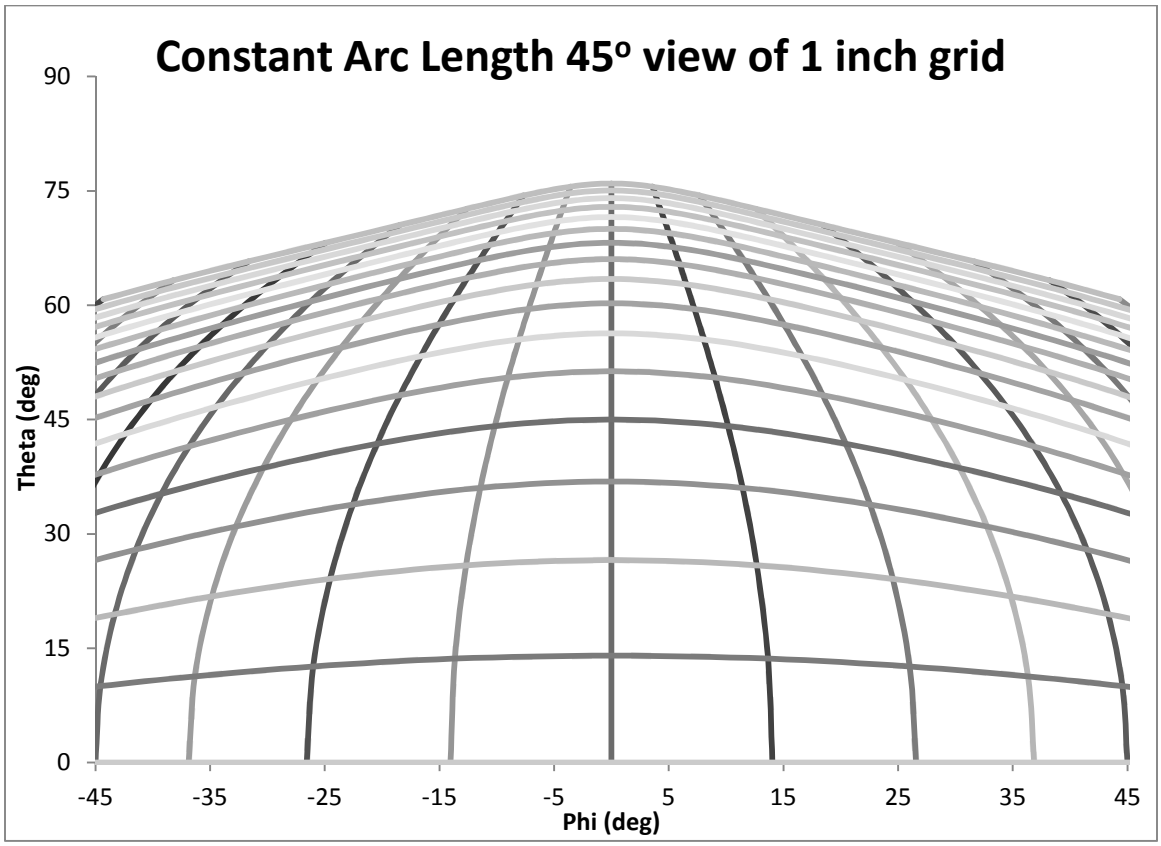

Figure 55 - a 90 degree FOV, constant arc length looking forward and down. The horizon is at the top of the image.

Therefore, while the pinhole camera is a better model for stitching nadir images into a photomosaic, the constant arc length camera may be a better model for stitching images of the horizon into a panorama.

The second advantage of the constant arc length camera involves measurement of radiation intensity at the edges of the image. In a pinhole camera, a certain area in the image covers a similar area in the focal plane. As the distance from the center of the image grows, the orientation of the object changes relative to the camera, reducing the intensity of the radiation seen by the camera. The following diagram and equation is from [Çengal, 2007].

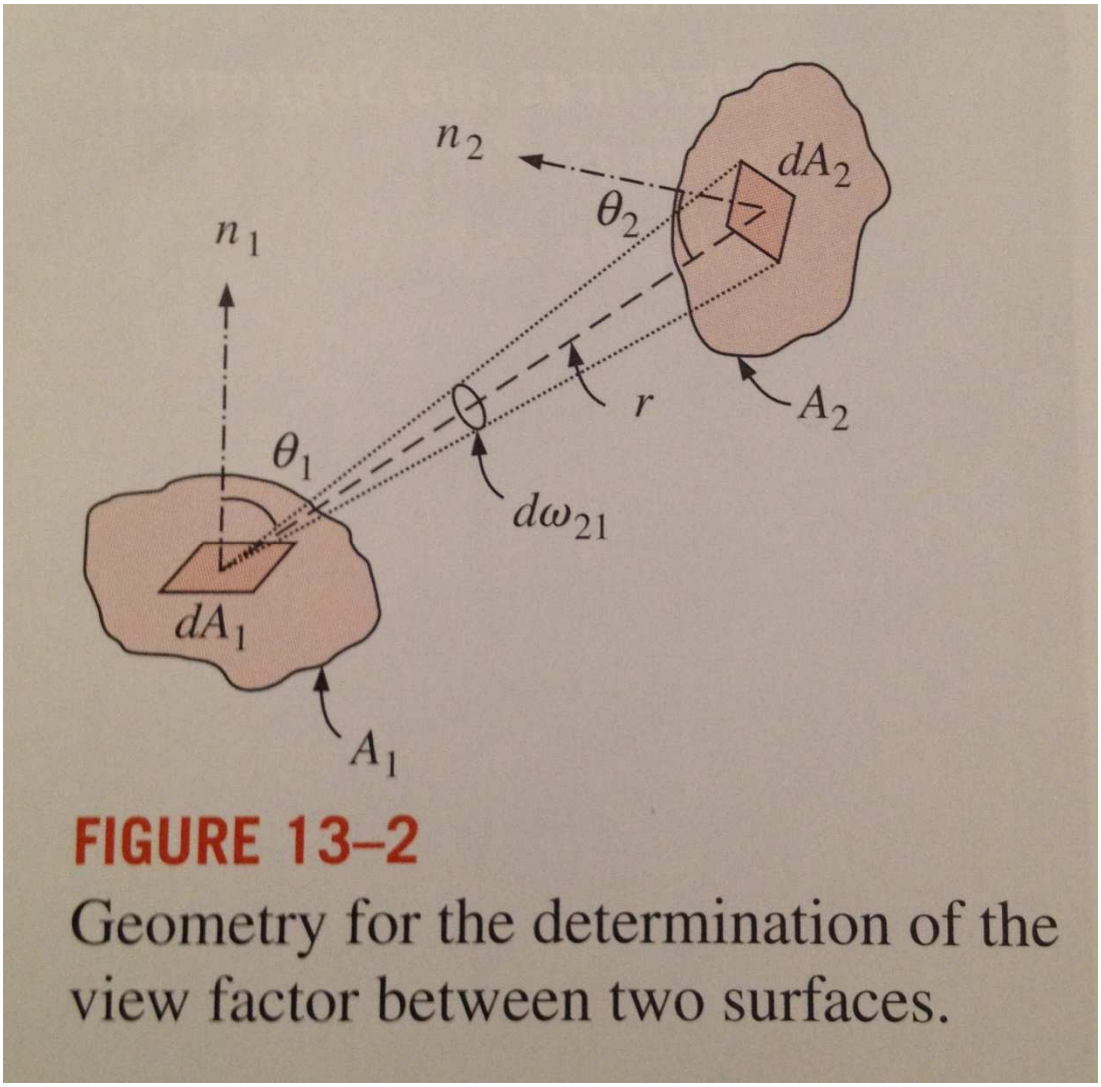

Figure 56 - An illustration of View Factor [Çengal, 2007]

The difference in radiant heat transfer due to orientation is demonstrated by the *view factor*, F.

$$dF_{dA_1 \to dA_2} = \frac{\dot{Q}_{dA_1 \to dA_2}}{\dot{Q}_{dA_1}} = \frac{\cos\theta_1 \cos\theta_2}{\pi r^2} dA_2$$

For a nadir camera looking at flat ground, $\theta_1 = \theta_2 = \theta$ and $r = d/\cos(\theta)$, where d is the perpendicular distance from the ground to the camera and dA_2 is a pixel's projection on the ground. So,

$$dF_{dA_1 \to dA_2} = \frac{\cos^4\theta}{\pi d^2} dA_2$$

This reduction in apparent intensity could be minimized by increasing the size of a pixel's projection far from the image center. This distortion is apparent in a camera with fish-eye effect, where the pixels on the edge seem compressed compared to the pixels in the center. The area in the focal plane covered by the pixel in a constant arc length camera is described below:

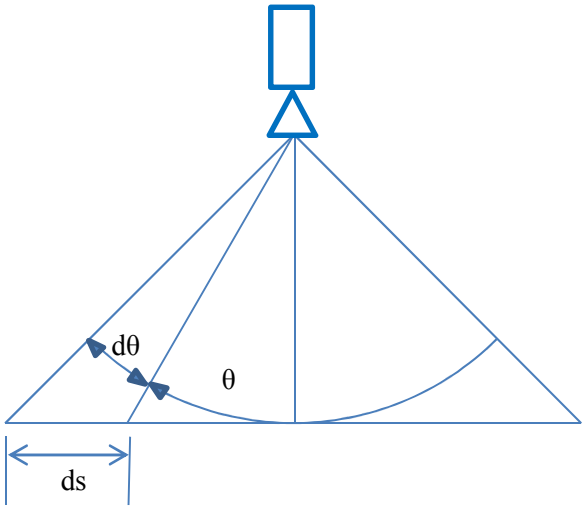

Figure 57 - An illustration of the correlation between a distance along the ground and the arc length that covers that distance.

$$ds = d(\tan(\theta + d\theta) - tan(\theta))$$

where "d" again is the perpendicular distance from the ground to the camera, and ds is the length of a single pixel's projection on the ground. Using a Taylor series expansion

$$\tan(\theta + d\theta) - tan(\theta) = \frac{d\tan\theta}{d\theta}\, d\theta + HOT \approx \sec^2\theta\, d\theta = \frac{d\theta}{\cos^2\theta}$$

$$dA_2 = ds^2 = \left(\frac{d\, d\theta}{\cos^2\theta}\right)^2$$

$$dF_{dA_1 \to dA_2} = \frac{\cos^4\theta}{\pi d^2} dA_2 = \frac{d\theta^2}{\pi}$$

And, therefore, the view factor is the same for all pixels in the image. Therefore, the intensity sensed in the pixel is proportional to the actual average reflectance of the surface projected on the ground by that pixel. To determine if the GoPro used a constant arc length camera model, a calibration image was taken from four inches above a grid sheet on the floor. A ruler was used to ensure the camera was four inches away, and a bubble level was laid across the back of the camera to ensure the camera remained level in at least one axis.

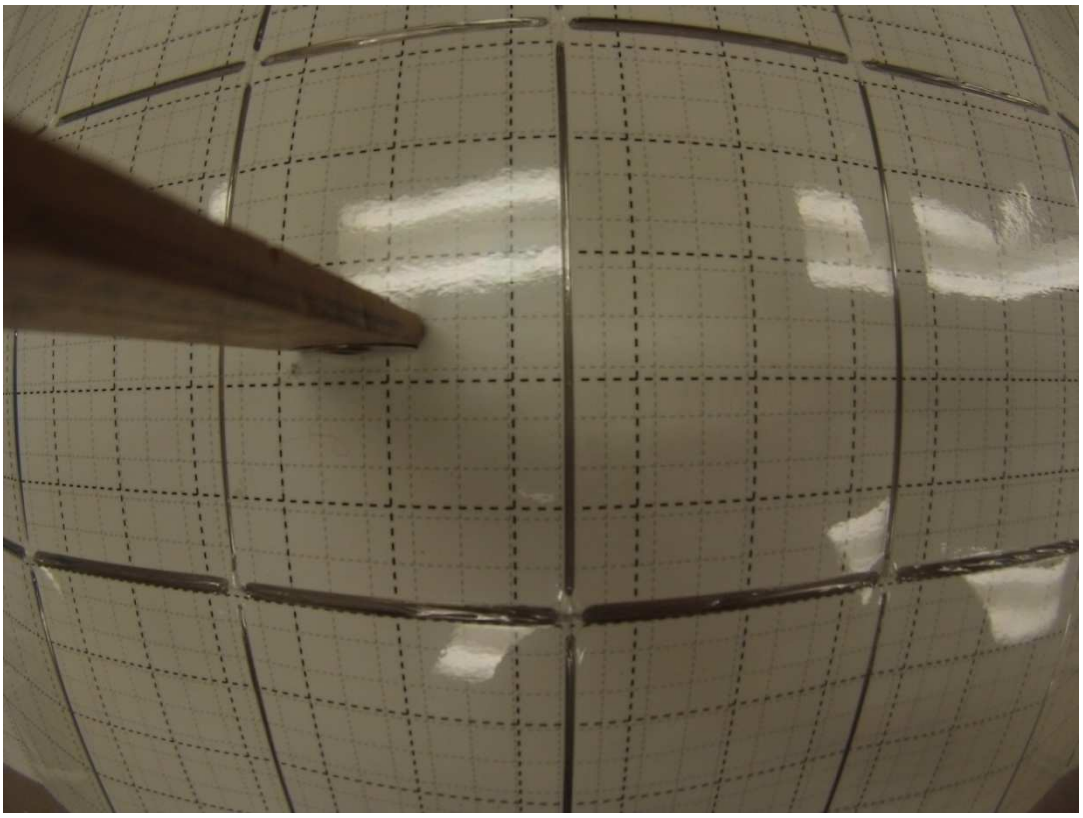

Figure 58 - A GoPro image of a grid mat 4 inches away from the camera lens. The heavy dotted lines represent 1 inch squares.

The image shows that the field of view is 12.5 inches wide and 8 inches tall. At four inches, this equates to 115° wide and 90° tall. A constant arc length image was also calculated in Excel, with the angles θ and φ calculated by the following formula:

$$\theta = \sin^{-1}\left(\frac{y}{r}\right)$$

$$\varphi = \sin^{-1}\left(\frac{x}{r}\right)$$

$$r = \sqrt{u^2 + v^2 + d^2}$$

Where "d" is four inches, y is the vertical distance from centerline on the grid mat, and x is the horizontal distance from the centerline on the grid mat. The following simulation was made for a constant arc length camera with a field of view like the one determined from the calibration picture. The camera is 4 inches from an 8 inch x 8 inch grid mat.

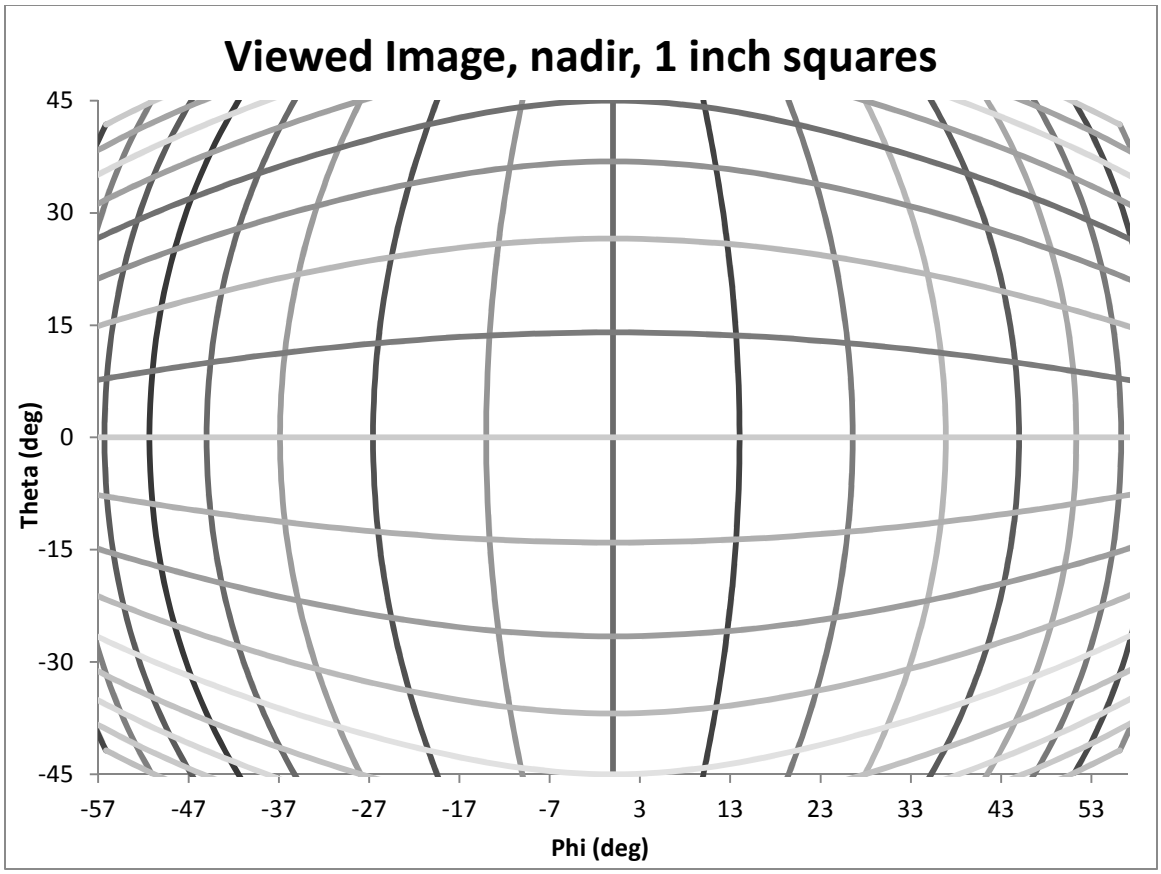

Figure 59 - A representation of a constant arc length looking down on a grid mat from 4 inches away. The lines represent 1 inch squares.

Therefore, a nadir oriented or gimbaled GoPro camera could be a lightweight and low-cost alternative to expensive calibrated spectral sensors.

APPENDIX B

WEATHER DATA

This appendix includes all weather information collected by the Marena Mesonet station during the flights performed at the OSU test plots and the surrounding burn sites. The satellite imagery presented here was compiled weekly by the U.S. Geological Survey EROS lab from AVHRR multispectral satellite imagery of the United States, and was collected from the OKFIRE website. OKFIRE is currently changing the imagery source from AVHRR satellites to the higher resolution MODIS imagery. Future visitors of the OKFIRE website will likely see the data presented in a slightly different format. The equations for determining fire danger indices from the new spectral bands will likely change as well. The following tables and maps were taken from the OKFIRE website for the weeks of relevant test flights. For more information how these values are calculated refer to [Carlson, 2002, Carlson 2003].

Site-Specific Table for Marena

(NFDRS Fuel Model T - Tallgrass with brush)

DATE TIME	BI	SC	ERC	IC	1-HR	10-HR	100-HR	1000-HR	HERB	WOODY	KBDI	TAIR	RELH	WSPD	RAIN_24H
Jan 30 2:00 pm	13	5	5	5%	9%	11%	9%	9%	74%	102%	252	45°F	43%	4 mph	0.00 in.
Jan 30 3:00 pm	20	9	7	7%	8%	11%	10%	9%	74%	102%	252	45°F	41%	4 mph	0.00 in.
Jan 30 4:00 pm	23	10	8	9%	8%	11%	10%	9%	74%	102%	252	46°F	40%	5 mph	0.00 in.
Feb 12 10:00 am	7	5	1	1%	14%	12%	11%	9%	38%	87%	208	33°F	62%	11 mph	0.00 in.
Feb 12 11:00 am	19	19	3	6%	11%	11%	11%	8%	38%	87%	208	35°F	46%	15 mph	0.00 in.
Feb 12 9:00 am	0	0	0	0%	17%	12%	11%	9%	38%	87%	208	29°F	76%	10 mph	0.00 in.
Mar 20 1:00 pm	9	5	2	3%	11%	18%	19%	11%	16%	77%	203	56°F	61%	5 mph	0.14 in.
Mar 20 2:00 pm	9	4	3	4%	10%	17%	18%	11%	16%	77%	203	58°F	64%	4 mph	0.14 in.
Mar 20 3:00 pm	16	9	4	6%	10%	16%	18%	11%	16%	77%	203	58°F	56%	5 mph	0.13 in.
Mar 20 4:00 pm	13	4	6	5%	9%	15%	18%	12%	16%	77%	203	59°F	56%	1 mph	0.10 in.
Mar 27 1:00 pm	25	19	5	9%	10%	11%	11%	10%	32%	84%	234	51°F	50%	10 mph	0.00 in.
Mar 27 2:00 pm	37	23	10	13%	8%	11%	11%	10%	32%	84%	234	52°F	43%	7 mph	0.00 in.
Mar 27 3:00 pm	40	21	13	16%	7%	10%	11%	10%	32%	84%	234	55°F	38%	7 mph	0.00 in.

Table 10 - Weather data from all flights, collected by the Marena Mesonet station. [OKFIRE]

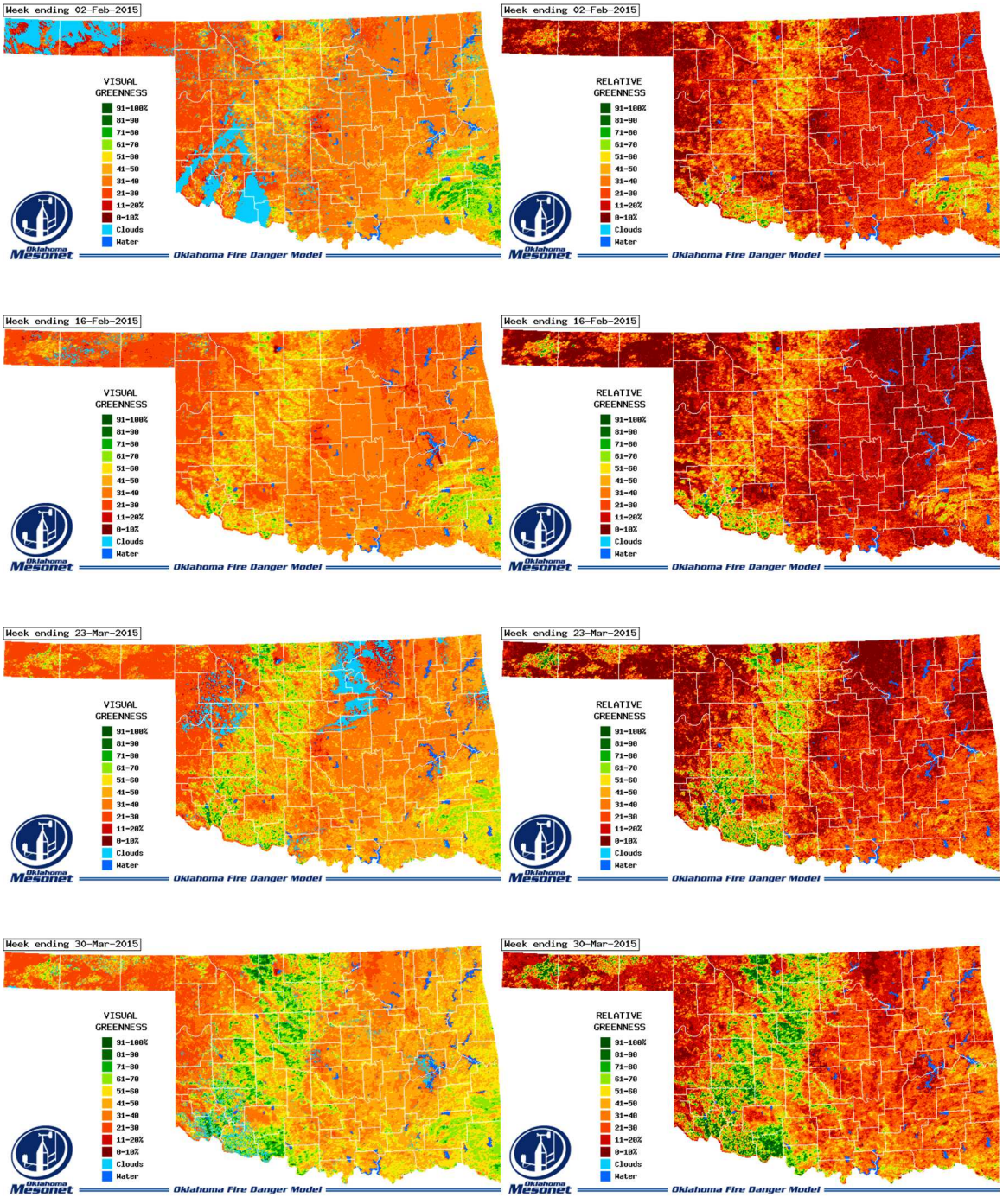

Figure 60 - Relative Greenness and Visual Greenness maps for all flights. [OKFIRE]

APPENDIX C

MATLAB CODE

```
% Nondimensional Difference Vegetative Index (NDVI) is the ratio of the
difference between visible and NIR light to their sum.  This program
calculates the NDVI image pixel-by-pixel, the average NDVI value, and
the NDVI value from the average visible and average NIR values in the
image.  It separates the image into foreground and background so that
odd shapes, such as SfM photomosaics, can also be calculated.  This
program uses the blue channel to measure visible reflectance, but the
red channel can also be used.
% by Dustin Gabbert, Oklahoma State University, 2015

CIR=imread('C:\Users\dgabber\Desktop\March 27 plots flight 4.png');

[rows, cols, chans] = size(CIR);

NIR = im2single(CIR(:,:,1));
green = im2single(CIR(:,:,2));
blue = im2single(CIR(:,:,3));

foreground = zeros(rows, cols, chans);
% background = zeros(rows, cols, chans);

counter = 0;
NDVItotal = 0;

NDVI = (NIR - blue) ./ (NIR + blue);

for i = 1:rows
    for j = 1:cols
        if NIR(i,j) > 0 && NIR(i,j) < 1 && blue(i,j) > 0 && blue(i,j) <
1 && green(i,j) > 0 && green(i,j) < 1
            foreground(i,j,1) = NIR(i,j);
            foreground(i,j,2) = blue(i,j);
            foreground(i,j,3) = green(i,j);
            NDVItotal = NDVItotal + NDVI(i,j);
```

```
            counter = counter + 1;
        else
%             background(i,j,1) = NIR(i,j);
%             background(i,j,2) = blue(i,j);
%             background(i,j,3) = green(i,j);
        end
    end
end

figure
imshow(index,'DisplayRange',[-1 1])
% title('Normalized Difference Vegetation Index')

NIRtotal = sum(sum(foreground(:,:,1)));
avgNIR = NIRtotal/counter
bluetotal = sum(sum(foreground(:,:,3)));
angblue = bluetotal/counter
imageNDVI = (NIRtotal-bluetotal)/(NIRtotal+bluetotal)
NDVIavg = NDVItotal/counter




% dark channel is the assumption that the smallest channel of any
% pixel in a non-smoke non-sky block is very small or zero,
% whereas all smoke pixels have at least a small value in every
% channel because of their gray color.
% by Mehran Aldalibi


clear all; clc; close all;

img1=imresize(imread('dc_bg.png'),[280 360],'bicubic');
img2=imresize(imread('dc_img.png'),[280 360],'bicubic');

% using overlapping windows and setting the value for the
% window's center

% window's size (use odd numbers)
wh=7;
ww=9;

% pre-allocation
dc_img1=255*ones(size(rgb2gray(img1)));
dc_img2=dc_img1;

% some boundary pixels will be left with 255
for i=1:280-wh+1
    for j=1:360-ww+1

        tmp1=img1(i:i+wh-1,j:j+ww-1);
        tmp2=img2(i:i+wh-1,j:j+ww-1);

        dc_img1(i+fix(wh/2),j+fix(ww/2))=min(tmp1(:));
        dc_img2(i+fix(wh/2),j+fix(ww/2))=min(tmp2(:));
```

```
    end
end

% displaying results
figure;subplot(2,1,1);imshow(img1);title('background
image');subplot(2,1,2);imshow(dc_img1,[]);title('Dark Channel of the
background image');
figure;subplot(2,1,1);imshow(img2);title('smoked
image');subplot(2,1,2);imshow(dc_img2,[]);title('Dark Channel of the
smoked image');
figure;imshow(dc_img2-dc_img1,[]);title('Change in the Dark Channel');



% Optical flow is found by finding the magnitude of change in greyscale
illumination between two images in the u and v directions.  This
program is designed to work with the dense optical flow software
developed by Deqing Sun, Department of Computer Science, Brown
University.
% by Mehran Aldalibi

clear all; clc; close all;

img1=imresize(imread('smoke111.png'),[256 512],'bicubic');
img2=imresize(imread('smoke112.png'),[256 512],'bicubic');

uv = estimate_flow_interface(img1, img2,'classic+nl-fast');
u=uv(:,:,1);
v=uv(:,:,2);

% orientation of optical flow
theta=atan2(u,v);

% filt1=[-1 0 1];
% filt2=[-1;0;1];

% second-order horizontal and vertical derivative filters (Laplacian
Operator)
filt1=[-1 16 -30 16 -1];
filt2=[-1 ;16 ;-30; 16 ;-1];

ux=conv2(u,filt1,'same');
uy=conv2(u,filt2,'same');

vx=conv2(v,filt1,'same');
vy=conv2(v,filt2,'same');

% optflow_smooth_img=(ux.^2)+(uy.^2)+(vx.^2)+(vy.^2);

% magnitude of Laplacian operator for optical flow components
optflow_smooth_img=abs(ux)+abs(uy)+abs(vx)+abs(vy);
```

```
% displaying results
figure;subplot(2,1,1);imshow(img1);title('image
1');subplot(2,1,2);imshow(img2);title('image 2');
figure;imshow(abs(double(rgb2gray(img2))-
double(rgb2gray(img1))),[]);title('image difference');
figure;quiver(u,v);title('optical flow quiver plot');
% figure;imshow(w,[]);title('optical flow magnitude');
figure;imshow(theta,[]);title('optical flow orientation');
```

```
%Grayness
%Dustin Gabbert

% clear all
% close all
% clc

fire=imread('C:\Users\dgabber\desktop\fire.png');

[rows, cols, chans] = size(fire);

smokeonly = uint8(zeros(rows,cols,chans)); %black background

for i = 1:rows
    for j = 1:cols
        maxcolor = max(fire(i,j,:));
%         if maxcolor > 150 % brightness check
            mincolor = min(fire(i,j,:));
            colorspread = maxcolor - mincolor; % greyness check
            if colorspread < 20
                smokeonly(i,j,1) = fire(i,j,1);
                smokeonly(i,j,2) = fire(i,j,2);
                smokeonly(i,j,3) = fire(i,j,3);
            end
%         end
    end
end

figure;
subplot 211;imshow(fire); title('original image');
subplot 212;imshow(smokeonly);title('segmented image');
```

```
%Wavelet transform separates the high frequency and low frequency
features in the horizontal and vertical directions to make four images.
The Low pass, Low pass image is the approximate image, and the High
pass, High pass image should have less energy in the area obscured by
smoke.
%Dustin Gabbert
```

```
fire = imread('C:\Users\dgabber\Desktop\fire.png');
[rows, cols, chans] = size(fire);

I = rgb2gray(fire); % grayscale conversion

wname = 'sym4';
[CA,CH,CV,CD] = dwt2(I,wname,'mode','per');

subplot(211)
imagesc(CD); title('Highpass Image');
colormap gray;
subplot(212)
imagesc(CA); title('Lowpass Approximation');
```

APPENDIX D

TEST PLOTS

The information gathered from the five tests at the OSU test plots has been collected in this appendix. For information on how this information was gathered refer to the applicable sections of Methodology and Results. The photomosaics below are organized by flight, in the following order: Agisoft PhotoScan mosaic, Agisoft Photoscan bNDVI mosaic, Pix4D photomosaic, Pix4D bNDVI mosaic.

Agisoft Photoscan:

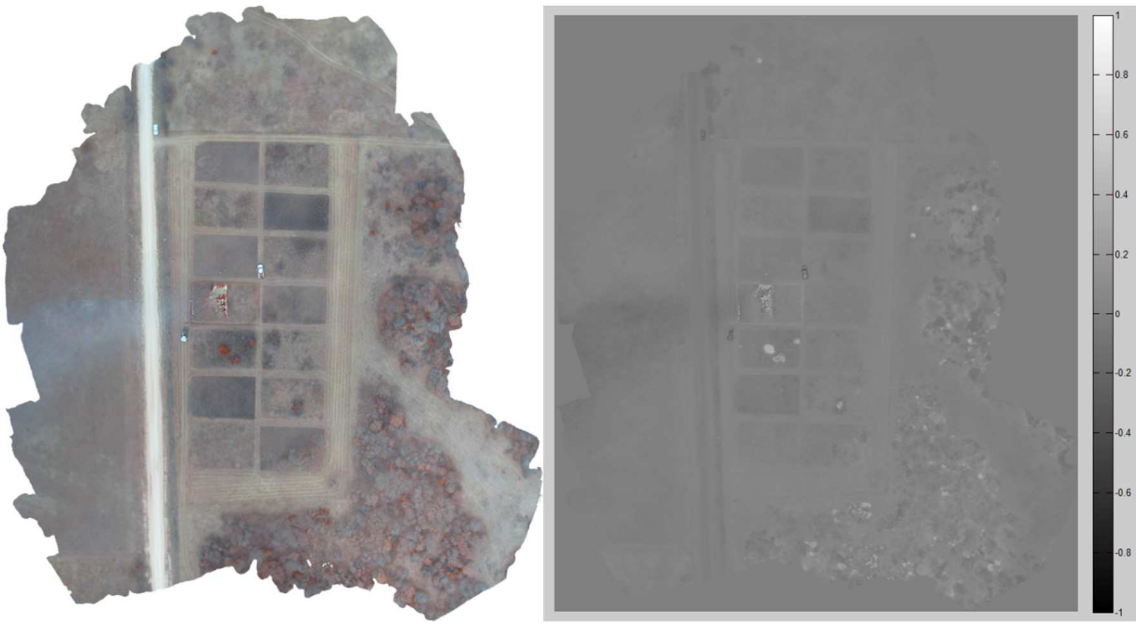

Pix4D:

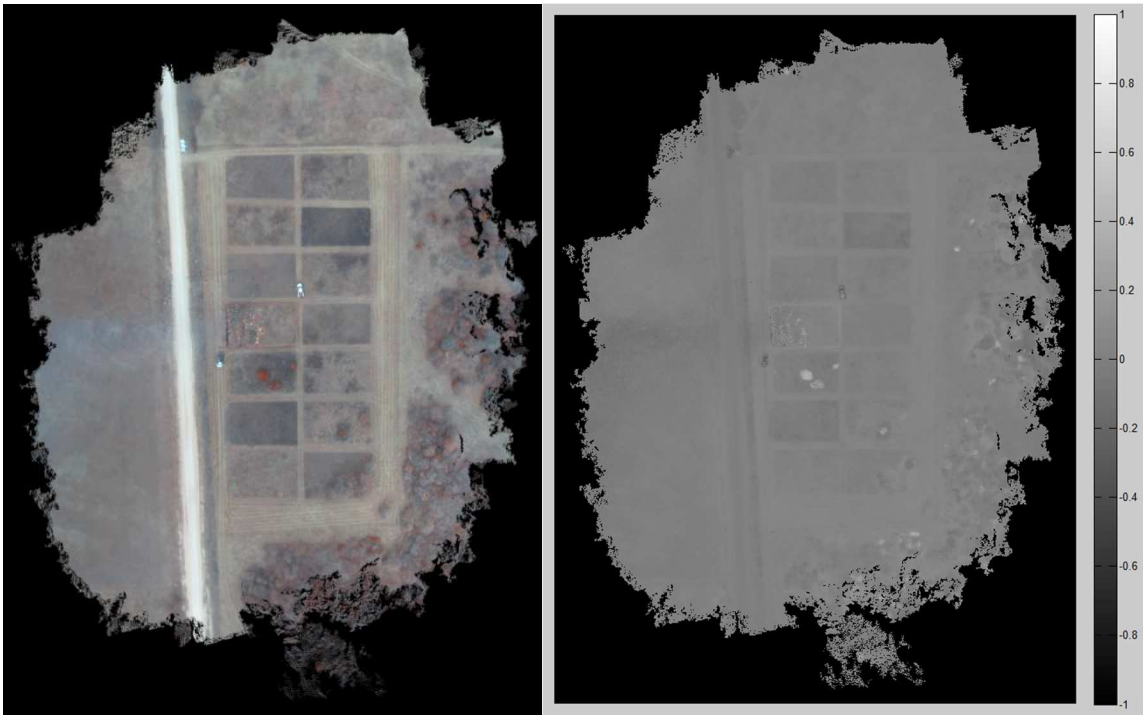

Figure 61 – Comparison image

Agisoft Photoscan:

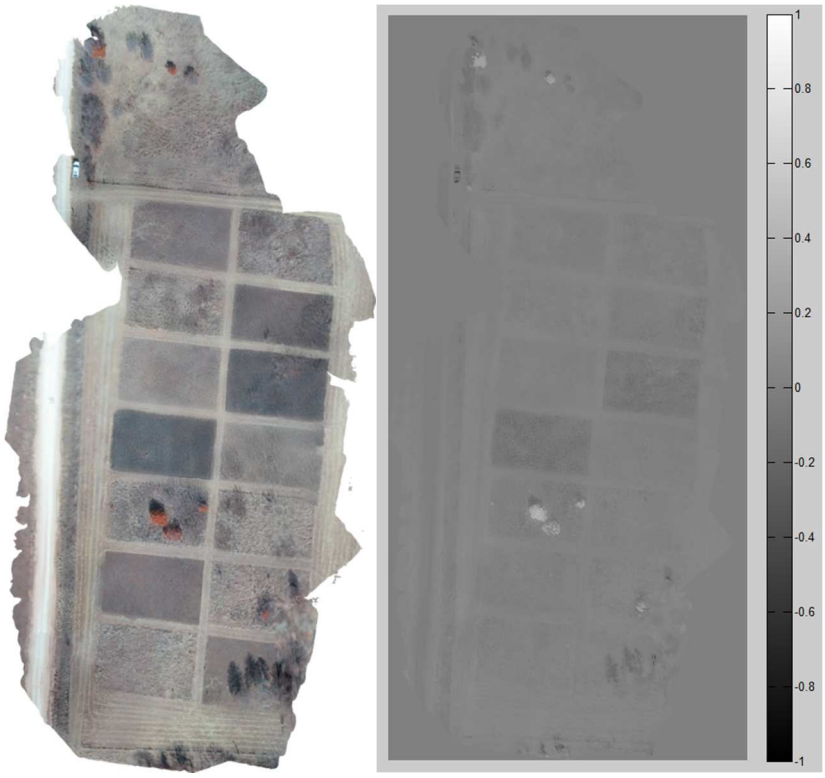

Pix4D:

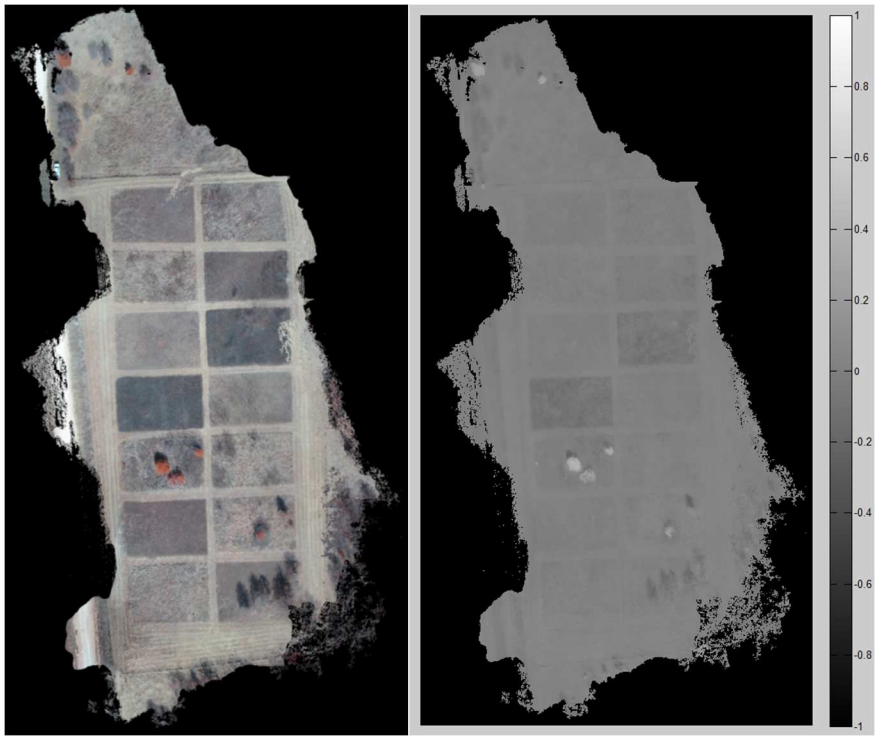

Figure 62 - Comparison image

Agisoft Photoscan:

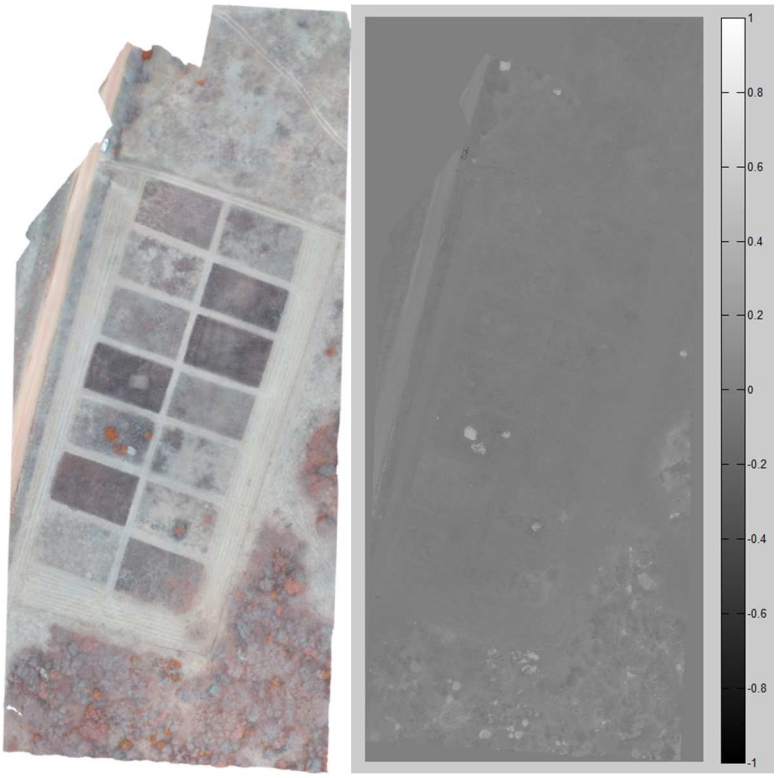

Pix4D:

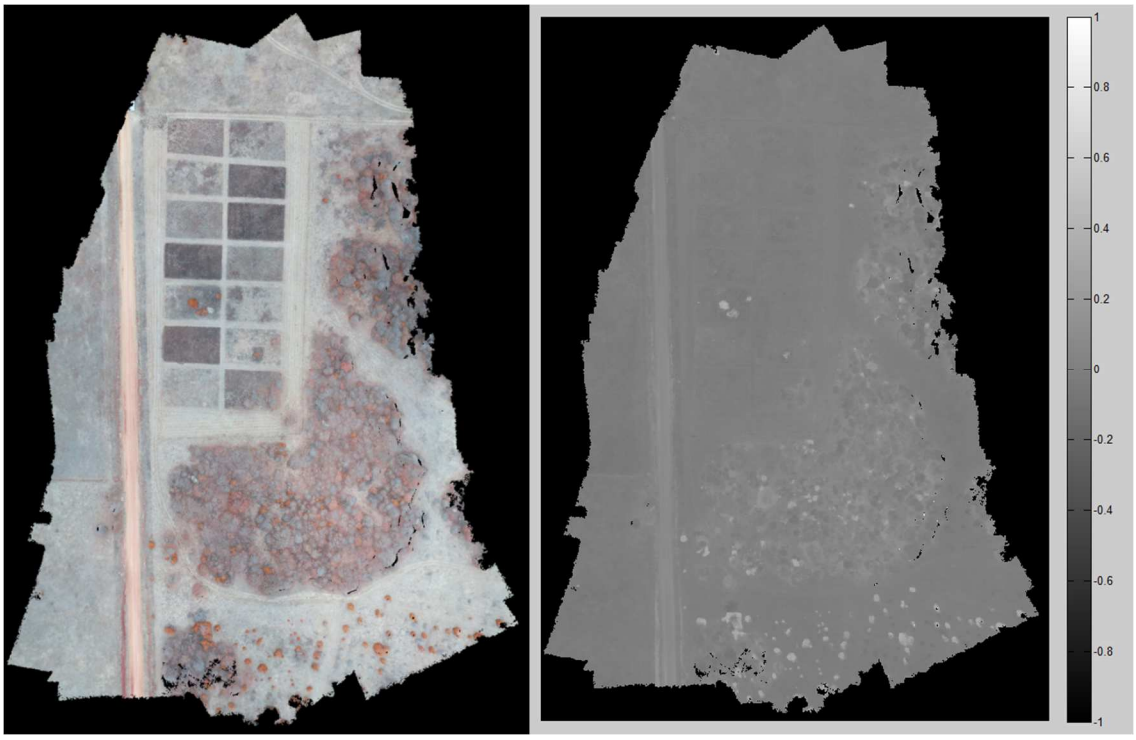

Figure 63 - Comparison image

Agisoft Photoscan:

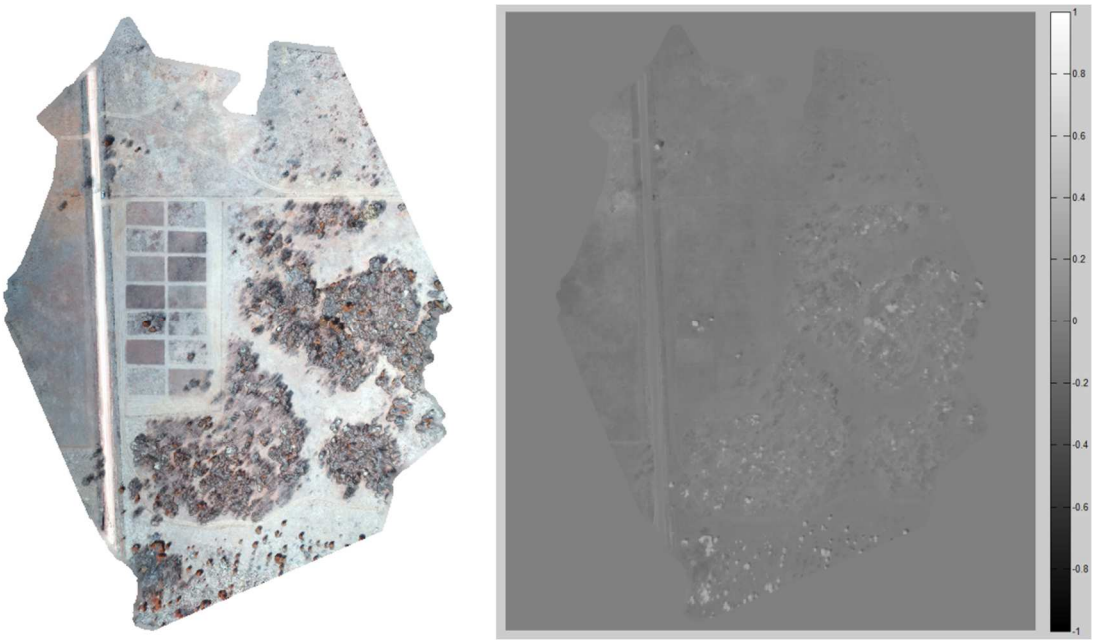

Pix4D:

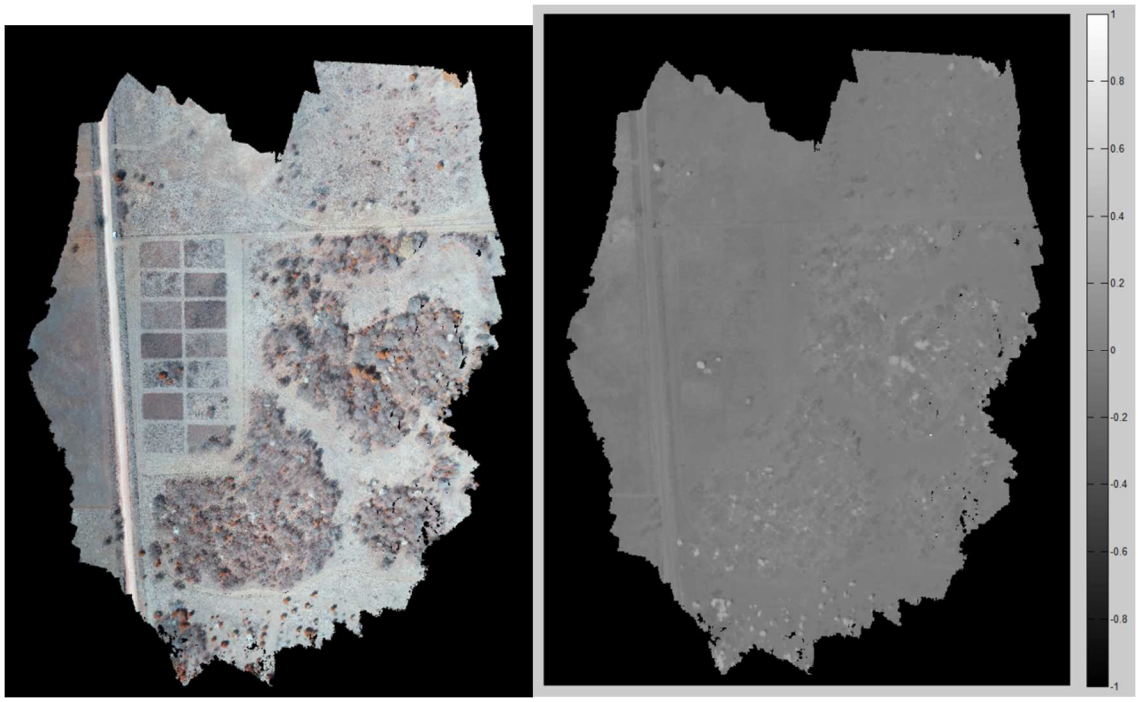

Figure 64 - Comparison image

Agisoft Photoscan:

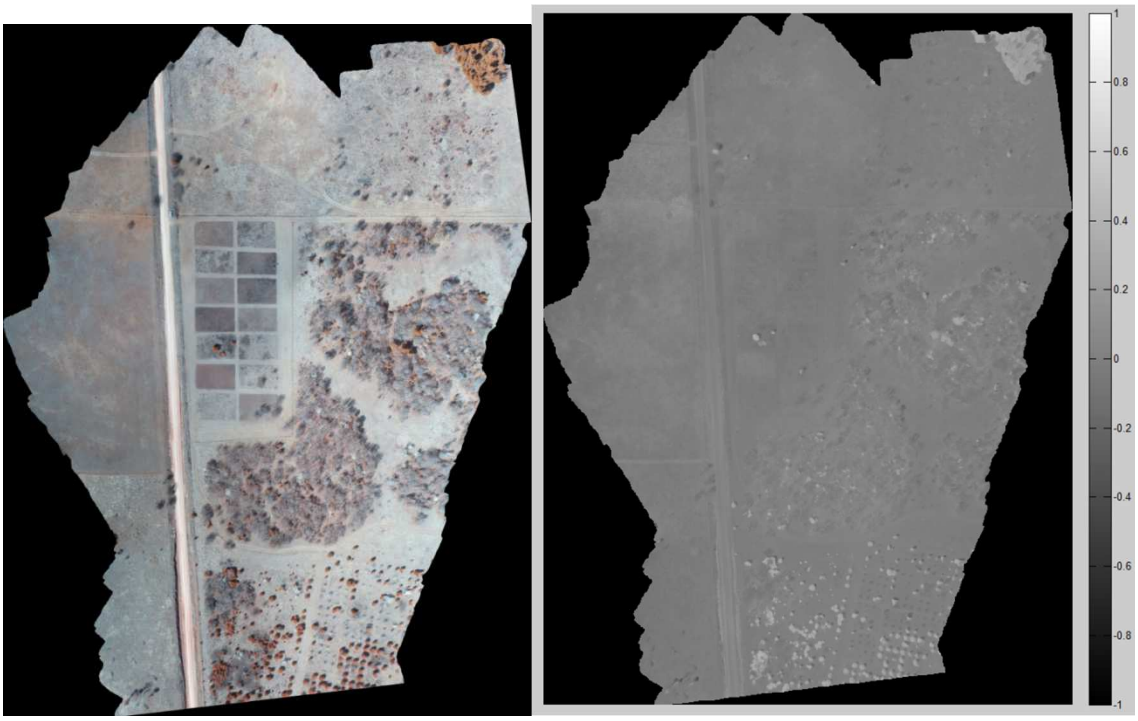

Pix4D:

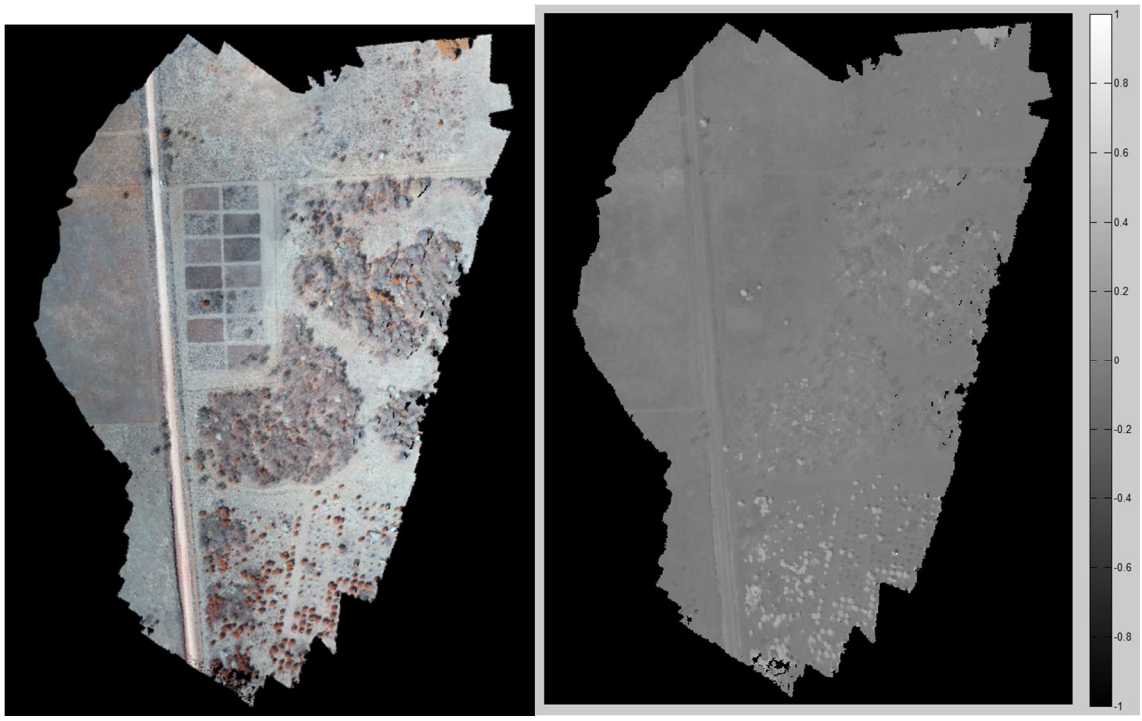

Figure 65 - Comparison image

Plot 1 – burned October 17, 2014			
Date	Enclosed 3D Area	Terrain 3D Area	Total Volume
Jan 30, 2015	1809.59 m^2	2999.30 m^2	201.24 m^3
Feb 12, 2015	2116.15 m^2	6947.78 m^2	375.58 m^3
March 20, 2015	754.23 m^2	1297.31 m^2	-57.75 m^3
March 27, 2015	931.36 m^2	1416.82 m^2	-15.19 m^3
March 27, 2015	814.72 m^2	1129.11 m^2	21.15 m^3

Table 11 - Pix4D geometric values for Plot 1.

Plot 2 – check plot, unintentionally burned April 7, 2009			
Date	Enclosed 3D Area	Terrain 3D Area	Total Volume
Jan 30, 2015	2030.75 m^2	4015.43 m^2	851.48 m^3
Feb 12, 2015	2132.72 m^2	9501.38 m^2	1537.21 m^3
March 20, 2015	860.59 m^2	1883.93 m^2	196.62 m^3
March 27, 2015	967.78 m^2	1477.81 m^2	104.96 m^3
March 27, 2015	876.18 m^2	1280.36 m^2	100.06 m^3

Table 12 - Pix4D geometric values for Plot 2.

Plot 3 – burned June 3, 2013			
Date	Enclosed 3D Area	Terrain 3D Area	Total Volume
Jan 30, 2015	1716.93 m^2	3303.96 m^2	760.75 m^3
Feb 12, 2015	2046.09 m^2	9119.82 m^2	1009.91 m^3
March 20, 2015	720.75 m^2	1288.00 m^2	147.15 m^3
March 27, 2015	892.63 m^2	1434.71 m^2	84.16 m^3
March 27, 2015	784.19 m^2	1182.89 m^2	88.35 m^3

Table 13 - Pix4D geometric values for Plot 3.

Plot 4 – burned December 2, 2014			
Date	Enclosed 3D Area	Terrain 3D Area	Total Volume
Jan 30, 2015	1771.50 m^2	3808.71 m^2	895.80 m^3
Feb 12, 2015	1896.12 m^2	12132.57 m^2	961.25 m^3
March 20, 2015	728.05 m^2	1825.13 m^2	109.85 m^3
March 27, 2015	898.77 m^2	1545.99 m^2	44.86 m^3
March 27, 2015	794.47 m^2	1383.45 m^2	83.36 m^3

Table 14 - Pix4D geometric values for Plot 4.

Plot 5 –August 18, 2014			
Date	Enclosed 3D Area	Terrain 3D Area	Total Volume
Jan 30, 2015*	1888.94 m^2	3880.54 m^2	441.54 m^3
Feb 12, 2015	2180.26 m^2	7714.58 m^2	336.20 m^3
March 20, 2015	801.79 m^2	1038.46 m^2	58.39 m^3
March 27, 2015	962.38 m^2	1335.72 m^2	22.47 m^3
March 27, 2015	819.88 m^2	1084.51 m^2	20.16 m^3
*A truck was in this plot, giving a larger than normal volume			

Table 15 - Pix4D geometric values for Plot 5.

Plot 6 – burned January 30, 2015			
Date	Enclosed 3D Area	Terrain 3D Area	Total Volume
Jan 30, 2015*	1926.30 m^2	4572.88 m^2	1239.13 m^3
Feb 12, 2015	2070.58 m^2	15550.51 m^2	321.35 m^3
March 20, 2015	807.82 m^2	1979.89 m^2	114.80 m^3
March 27, 2015	951.67 m^2	1760.56 m^2	68.81 m^3
March 27, 2015	874.80 m^2	1539.55 m^2	88.34 m^3
*A truck was in this plot, giving a larger than normal volume			

Table 16 - Pix4D geometric values for Plot 6.

Plot 7 – burned January 30, 2015			
Date	Enclosed 3D Area	Terrain 3D Area	Total Volume
Jan 30, 2015*	1783.48 m^2	5211.23 m^2	670.66 m^3
Feb 12, 2015	2103.36 m^2	8091.77 m^2	277.47 m^3
March 20, 2015	753.94 m^2	1208.57 m^2	60.44 m^3
March 27, 2015	922.24 m^2	1273.42 m^2	22.50 m^3
March 27, 2015	795.43 m^2	1095.65 m^2	45.65 m^3
*This plot was burning during the test.			

Table 17 - Pix4D geometric values for Plot 7.

Plot 8 – burned August 18, 2014			
Date	Enclosed 3D Area	Terrain 3D Area	Total Volume
Jan 30, 2015	1686.26 m^2	3020.89 m^2	159.61 m^3
Feb 12, 2015	1990.34 m^2	10472.11 m^2	217.49 m^3
March 20, 2015	761.74 m^2	1058.59 m^2	4.18 m^3
March 27, 2015	890.79 m^2	1250.65 m^2	-6.25 m^3
March 27, 2015	817.36 m^2	1198.33 m^2	23.94 m^3

Table 18 - Pix4D geometric values for Plot 8.

Plot 9 – check plot, never burned, 3 trees			
Date	Enclosed 3D Area	Terrain 3D Area	Total Volume
Jan 30, 2015	1765.74 m^2	6056.30 m^2	2660.14 m^3
Feb 12, 2015	2059.17 m^2	17785.02 m^2	1380.12 m^3
March 20, 2015	786.03 m^2	3437.96 m^2	638.17 m^3
March 27, 2015	916.92 m^2	4302.39 m^2	545.81 m^3
March 27, 2015	806.05 m^2	3161.46 m^2	575.30 m^3

Table 19 - Pix4D geometric values for Plot 9.

Plot 10 – burned March 26, 2013			
Date	Enclosed 3D Area	Terrain 3D Area	Total Volume
Jan 30, 2015	1804.23 m^2	3651.80 m^2	565.25 m^3
Feb 12, 2015	2057.66 m^2	19151.46 m^2	697.39 m^3
March 20, 2015	799.68 m^2	1614.99 m^2	118.71 m^3
March 27, 2015	921.67 m^2	1488.15 m^2	62.70 m^3
March 27, 2015	798.45 m^2	1344.43 m^2	90.57 m^3

Table 20 - Pix4D geometric values for Plot 10.

Plot 11 – burned December 2, 2014			
Date	Enclosed 3D Area	Terrain 3D Area	Total Volume
Jan 30, 2015	1883.76 m^2	3086.43 m^2	594.95 m^3
Feb 12, 2015	2143.44 m^2	13445.88 m^2	1190.04 m^3
March 20, 2015	804.35 m^2	1243.73 m^2	108.81 m^3
March 27, 2015	961.41 m^2	1347.22 m^2	119.00 m^3
March 27, 2015	892.03 m^2	1557.79 m^2	134.47 m^3

Table 21 - Pix4D geometric values for Plot 11.

Plot 12 – burned June 3, 2013, 3 trees			
Date	Enclosed 3D Area	Terrain 3D Area	Total Volume
Jan 30, 2015	1870.04 m^2	4618.52 m^2	1069.82 m^3
Feb 12, 2015	2155.92 m^2	11553.18 m^2	536.17 m^3
March 20, 2015	811.39 m^2	1973.40 m^2	239.46 m^3
March 27, 2015	971.87 m^2	1841.75 m^2	209.33 m^3
March 27, 2015	852.55 m^2	1606.18 m^2	190.39 m^3

Table 22 - Pix4D geometric values for Plot 12.

Plot 13 – burned March 26, 2013			
Date	Enclosed 3D Area	Terrain 3D Area	Total Volume
Jan 30, 2015	2013.55 m^2	4150.89 m^2	1106.18 m^3
Feb 12, 2015	2252.17 m^2	9172.80 m^2	1127.16 m^3
March 20, 2015	892.15 m^2	1636.60 m^2	219.80 m^3
March 27, 2015	1018.03 m^2	1302.26 m^2	185.57 m^3
March 27, 2015	931.49 m^2	1484.13 m^2	168.62 m^3

Table 23 - Pix4D geometric values for Plot 13.

Plot 14 – burned October 17, 2014, 4 trees			
Date	Enclosed 3D Area	Terrain 3D Area	Total Volume
Jan 30, 2015	1893.62 m^2	13009.53 m^2	3346.42 m^3
Feb 12, 2015	2307.90 m^2	14020.99 m^2	1324.27 m^3
March 20, 2015	824.33 m^2	9142.37 m^2	718.86 m^2
March 27, 2015	992.66 m^2	8054.81 m^2	455.02 m^3
March 27, 2015	949.72 m^2	5285.82 m^2	265.54 m^3

Table 24 - Pix4D geometric values for Plot 14

VITA

Dustin W. Gabbert

Candidate for the Degree of

Master of Science

Thesis: AN EVALUATION OF IMAGE BASED TECHNIQUES FOR WILDFIRE DETECTION AND FUEL MAPPING

Major Field: Mechanical and Aerospace Engineering, UAS Option

Biographical:

Education:

Completed the requirements for the Master of Science in Mechanical and Aerospace Engineering at Oklahoma State University, Stillwater, Oklahoma in May, 2015.

Completed the requirements for the Bachelor of Science in Mechanical Engineering at Oklahoma State University, Stillwater, OK in 2011.

Completed the requirements for the Bachelor of Science in Aerospace Engineering at Oklahoma State University, Stillwater, OK in 2011.

Experience:

UH-60 Blackhawk Helicopter Pilot in the Army National Guard since 2012.

Member of Technical Staff at Sandia National Labs since 2011.

Professional Memberships:

American Society of Mechanical Engineers, member.
Oklahoma State University student chapter president, 2010-2011.

American Institute of Aeronautics and Astronautics, member.